NJ-2016-002

Design and Fabrication of Orthotropic Deck Details

FINAL REPORT
Vol. I
February 2016

Submitted by

Sougata Roy, Ph.D.
Former Principal Research Scientist
ATLSS Center
Lehigh University

Soham Mukherjee
Former Research Assistant
ATLSS Center
Lehigh University

NJDOT Research Project Manager
Ms. Priscilla Ukpah

In cooperation with

New Jersey
Department of Transportation
Bureau of Research

DISCLAIMER

TECHNICAL REPORT
STANDARD TITLE PAGE

1. Report No. NJ-2016-002	2.Government Accession No.	3. Recipient's Catalog No.
4. Design and Fabrication of Orthotropic Deck Details FINAL REPORT Vol. I of VII Volumes		5. Report Date February 2016
		6. Performing Organization Code
7. Author(s) Roy, Sougata Ph.D. and Soham Mukherjee		8. Performing Organization Report No.
9. Performing Organization Name and Address Advanced Technology for Large Structural Systems (ATLSS) Engineering Research Center, Lehigh University 117 ATLSS Drive Bethlehem, PA 18015		10. Work Unit No.
		11. Contract or Grant No.
12. Sponsoring Agency Name and Address New Jersey Department of Transportation PO 600 Trenton, NJ 08625		13. Type of Report and Period Covered
		14. Sponsoring Agency Code

15. Supplementary Notes
Volume 1 has 133 pages. All seven Volumes total 804 pages.

16. Abstract

The objectives of the research were to verify the design and fabrication of the orthotropic deck details proposed for the lift bridge, for infinite fatigue life. Multi-level 3D finite element analyses (FEA) of the proposed deck were performed to determine the critical stresses at the connections, the corresponding load position, and the deck specimen. To develop cost-effective connection details, three variations of rib-to-floor beam and rib-to-deck plate connection details, including the influence of different fabrication parameters, were explored in full-scale small size mockups. Subsequently, the infinite life fatigue performance of the connection details were evaluated by laboratory testing of a full-scale prototype. The fatigue testing was conducted under simulated rear tandem axle loading of the AASHTO fatigue truck with adequate boundary condition. The prototype testing was runout after 8 million cycles, verifying the infinite life fatigue performance of the deck design.

17. Key Words Lift Span, Orthotropic Deck, Rounded Bottom Ribs, Infinite Fatigue Life, Full-Scale Prototype, Fatigue Testing, AASHTO, Run-Out, Cost-Effective, Fabrication.	18. Distribution Statement

19. Security Classif (of this report) Unclassified	20. Security Classif. (of this page) Unclassified	21. No of Pages 133	22. Price

Form DOT F 1700.7 (8-69)

ACKNOWLEDGEMENTS

The authors wish to acknowledge the efforts of the New Jersey Department of Transportation (NJDOT) including the Project Manager Ms. Priscilla Ukpah and Ms. Camille Crichton-Sumners, Manager of the Bureau of Research. The authors thank the Research Selection and Implementation Panel members that included the following NJDOT employees: Ms. Xiaohua Hannah Cheng, Mr. Eddy Germain, Mr. Fred Lovett, Mr. Mahesh Patel, Mr. David Lambert, Mr. Nat Kasbekar, Mr. Eric Kraehenbuehl, Mr. Jayant Dalal, Mr. Vijaykumar Thaker, Ms. Kiranben Patel and Mr. Javier Estradal. These individuals offered valuable comments and suggestions on the research project resulting in an improved product.

Editing of the final report was performed by Dr. Richard Sause, Director of the ATLSS Center.

The research was performed with the assistance of Mr. Xudong Zhao, Mr. Philipp Keller, Mr. Frank Artmont, Mr. Yeun Chul Park and Mr. Juan Tzoc, and the support staff of ATLSS Engineering Research Center and Fritz Engineering Laboratory for their help with successful execution of the project.

The authors would also like to specially thank Mr. Ronnie Medlock, Vice President of Technical Services of High Steel Structures for valuable input on fabrication of this deck and to Dr. John W. Fisher for sharing his vast experience regarding orthotropic decks.

CONTENTS (VOLUME I)

CONTENTS (VOLUME II)

CONTENTS (VOLUME III)

CONTENTS (VOLUME IV)

CONTENTS (VOLUME V)

CONTENTS (VOLUME VI)

CONTENTS (VOLUME VII)

LIST OF FIGURES (VOLUME I)

LIST OF TABLES (VOLUME I)

EXECUTIVE SUMMARY

The proposed design of the vertical lift span for the New Jersey Department of Transportation (NJDOT) Route 7 Wittpenn Bridge replacement uses a steel box girder with an integrated orthotropic deck. In contrast to the orthotropic bridge decks implemented in the United States over the past two decades, the subject deck incorporates a $^{3}/_{4}$ in. (19 mm) deck plate stiffened by $^{5}/_{16}$ in. (8 mm) thick rounded bottom ribs (U-shaped) passing continuously through matching cutouts in the floor beams without any extended cut-out under the rib soffit. Perceived to be cost-effective, the fitted floor beam-to-rib connection is proposed to be fillet welded, however, performance of this connection requires careful fit-up, which can incur additional fabrication costs. Fabrication of the sheer length of partial joint penetration (PJP) welds for the rib-to-deck plate connections also needs careful consideration for controlling the initial cost and successful long term performance of the orthotropic deck. In addition, the replacement bridge is expected to experience high volume of Average Daily Truck Traffic (ADTT), as Route 7 is a key component of the NJDOT's Portway Corridor serving as a main trucking route between the New York Metropolitan area and the greater area of Kearny and the Meadowlands. Accordingly, the design and fabrication of the orthotropic deck details for the proposed bridge were evaluated at the ATLSS Engineering Research Center of Lehigh University, Bethlehem, PA for ensuring effective life cycle cost, including cost-effective fabrication and infinite fatigue life, i.e., no in-service fatigue cracking during the design life of the bridge. All orthotropic deck fabrications for this study were performed by High Steel Structures of Lancaster, PA.

In the initial phase of the research project, multi-level 3D linear elastic finite element analyses (FEA) of the proposed bridge deck were performed that identified the rib-to-floor beam connection adjacent to a box girder as the most critically stressed region of the deck, when the rear tandem axle of the AASHTO fatigue design truck was symmetric with the floor beam and the rib was located in the shear span of the floor beam. Based on the analyses, a full-scale prototype of the part bridge deck comprising 5 ribs and 3 floor beams, and a test setup that would adequately replicate the boundary conditions were decided for assessing the in-service fatigue performance of the proposed deck by testing in the laboratory under simulated conditions during the final phase of the project. In addition, three variations of rib-to-floor beam and rib-to-deck plate connection details, including the influence of different fabrication parameters, were explored in this phase by fatigue testing and subsequent destructive evaluation of small-size full-scale mockups. The mockup specimens identified a unique failure mode of the rib-to-floor beam connection, where cracks initiating from the unfused weld root propagated into the floor beam web and the rib wall normal to the principal stress field, particularly when the stresses were significantly large. This study found that: (a) rib-to-deck plate connections employing a 70% PJP weld with a $^{5}/_{32}$ in. (4 mm) root face on the rib wall and maximum 0.02 in. (0.5 mm) fit-up gap; and (b) rib-to-floor beam connections employing a PJP weld with $^{1}/_{8}$ in. (3 mm) double bevel on the floor beam web and a maximum fit-up gap of $^{1}/_{8}$ in. (3 mm), were the most cost-effective.

As per NJDOT's recommendation, however, the following details were considered for evaluation in the prototype deck: (a) rib-to-deck plate connections: 80% PJP weld with minimum 70% penetration, no joint preparation on the rib wall and a maximum fit-up gap of 0.020 in. (0.5 mm); and (b) rib-to-floor beam connections: $^{5}/_{16}$ in. (8 mm) fillet weld with fit-up gap not exceeding $^{1}/_{16}$ in. (1.5 mm). Weld procedure specifications for fabricating this specimen as per the recommended details were developed on additional mockups and were qualified by destructive evaluation. In addition, non-destructive assessment of the rib-to-deck plate weld penetration using Phase Array Ultrasonic Testing (PAUT) was compared with destructive measurements.

The prototype deck was fabricated in two panels, which were spliced (transverse to the ribs) in the laboratory by a complete joint penetration (CJP) weld at the deck plate and bolted splices at the ribs and the girder, simulating the field splice in the actual bridge construction. During assembly of the deck panels in the laboratory, significant lack of fit was noted between the panels due to the distortion from welding heat effects on asymmetric cross section of the specimen. A maximum out-of-flatness of about $^{3}/_{16}$ in. (5 mm) between the mating deck panels existed adjacent to the deck splice after welding, which exceeded the specified tolerance of $^{1}/_{16}$ in. (1.6 mm) prior to welding. In addition, a maximum offset of $^{3}/_{8}$ in. (9.5 mm) was observed between the ribs at the splice, which also exceeded the specified tolerance. The CJP deck plate splice was performed from the top with a brass backing bar, which was removed and the weld root was back-gouged and welded again from the underside. Use of a brass backing bar, however, resulted in significant lack of fusion (LOF) at the weld root, which could not be effectively repaired due to access restrictions from the presence of the ribs.

The fatigue testing was performed using a pair of above-deck hydraulic actuators, which were attached to spreader beams and loading pads, simulating the rear tandem axles of the AASHTO fatigue truck for orthotropic deck design and the tire contact with the deck plate. The actuators were positioned consistent with the critical load disposition determined from the analytical studies, and were cycled in tandem. The deck was loaded as per the Fatigue I limit state load of the AASHTO LRFD Bridge Design Specifications (1) 6th edition to verify infinite life performance, which resulted in a total load range of 82.8 kip (368.4 kN) or 41.4 kip (184.2 kN) per axle (or actuator) and 20.7 kip (92.1 N) per load pad. In addition, an under-deck actuator provided at the inner floor beam was cycled for a displacement range of 0.1 in., synchronous with the above-deck actuators to simulate the global displacement boundary condition. The deck was extensively instrumented with strain gauges and displacement transducers to evaluate the response of various connection details, with majority of the instrumentation concentrated at the critical connection between the inner floor beam and the rib adjacent to the girder.

The fatigue testing was run-out at 8 million cycles without any detectable fatigue cracking in the deck. The measured stress ranges at all critical connections were less than the CAFT of their respective detail categories. The test results would indicate infinite life performance of the deck design, as long as the site specific overloads do not exceed the AASHTO Fatigue I limit state load more than 1 in 10000 occurrences. The test results also demonstrated that deviation from the specified fabrication tolerances and rejected welding procedures, which were noted during the specimen fabrication and installation, did not affect the fatigue resistance of the connection details. These results suggest that further research is needed to develop appropriate fabrication tolerances and welding procedures.

The research developed cost-effective details for fitted rib-to-floor beam connections, and rib-to-deck plate connections for orthotropic bridge decks. In addition, the study provided critical information on issues related to fabrication and installation of the orthotropic deck design for the proposed Wittpenn Bridge, and the expected performance of the orthotropic deck in service under fatigue limit state loading, ensuring effective life cycle cost. The research also highlighted the need for developing rational tolerances for economic domestic fabrication of orthotropic decks based on one fabricator’s experience.

1. INTRODUCTION

1.1 Background

The proposed design of the vertical lift span for the New Jersey Department of Transportation (NJDOT) Route 7 Wittpenn Bridge replacement uses a steel box girder with an integrated orthotropic deck. Steel orthotropic was the ideal choice for the lift bridge because of light weight and inherent redundancy that created less demand on the prime movers, reduced dead load stress, allowed increased span lengths, and enhanced the life cycle of the main supporting elements. A thin wearing surface (overlay) on a 5/8 in (16 mm) or thicker deck plate can provide sufficient overlay for durability, improved riding quality and low maintenance, with further reduction in dead load and life-cycle cost (LCC). In addition, in-service performance and limited laboratory tests have demonstrated that if adequately designed and properly constructed, the orthotropic deck is the only system likely to provide a service life exceeding 100 years with minimum maintenance and optimum LCC (Fisher and Roy 2010 (2)).

The Wittpenn Bridge (Figure 1), carrying Route 7 over Hackensack River, is located between Jersey City (to the east) and Kearny (to the west) in Hudson County and serves as a major connector between Routes 139 and 1&9 Truck (1&9T) to the east, and the New Jersey Turnpike Interchange 15W and Newark/Jersey City Turnpike to the west. Route 7 is a key component of the NJDOT's Portway Corridor serving as a main trucking route between the New York Metropolitan area and the greater area of Kearny and the Meadowlands. Accordingly, the replacement bridge is expected to experience significant truck traffic. In terms of time-dependent deterioration (corrosion and fatigue), the deck is the most vulnerable element of a bridge subjected to: abrasive loading from passing vehicles; direct exposure to the elements of weather; and road salts applied as part of winter maintenance. The in-service fatigue damage of steel bridges and the wearing surfaces from repeated loading is caused primarily by the truck traffic in the vehicular traffic spectrum. For steel deck elements and wearing surfaces, the number of repeated load cycles from truck traffic is further multiplied by the number of axles. As such, the expected high volume of Average Daily Truck Traffic (ADTT) on the Wittpenn Bridge is a concern. To ensure long term durability and effective LCC, the design and fabrication of the orthotropic deck details needed to be verified for infinite fatigue life, i.e., no in-service fatigue cracking during the design life of the bridge.

1.2 Proposed Replacement Orthotropic Deck

The framing plan (without the cross frames) and the cross section of the proposed replacement orthotropic deck are shown in Figures 2 and 3 respectively. The lift span of the deck was 324 ft. and the transverse width was 110 ft. The deck was supported by 46 equally spaced longitudinal ribs and 27 equally spaced transverse floor beams. The floor beams were spaced at 11 ft. 9 in. (3.6 m) apart and the ribs were paced 2 ft. 4 in. (711 mm) apart. As shown in Figure 2, the carriageway of the bridge spans along the east-west direction. It has three box girders identified as BG-1, BG-2 and BG-3 with an integrated orthotropic deck. The box girders have a bottom flange 12 ft. x 21/4 in (3.7 m x 57 mm). The box girder web is $^{9}/_{16}$ (14 mm) in thick with a depth of 14 ft. 9 in (4.5 m).

The design details of the orthotropic deck are shown in Figure 4. The design uses trapezoidal ribs with rounded bottom (U-shaped). The ribs are 14 in (356 mm) high having ${}^{5}/_{16}$ in (8 mm) thick rib wall. The deck plate is ¾ in (19 mm) thick. The rib-to-deck weld is specified as 80% partial joint penetration (PJP) groove weld. The floor beams vary in depth with about an average nominal depth of 3 ft 4 in. (1 m). The floor beam web is ½ in (13 mm) thick. The floor beam is designed to fit the ribs all around without any additional cutout under the rib soffit, with the ribs passing continuous through the floor beam. All around ${}^{5}/_{16}$ in. (8 mm) fillet welds from both sides are specified between the floor beam web and the ribs, and the floor beam web and the deck plate.

1.3 Research Rationale

To ensure optimum LCC of the proposed orthotropic deck for the Wittpenn Bridge, cost-effective fabrication of the deck details needed to be developed and their fatigue performance needed to be verified for infinite life. The fabrication scenarios needed to be investigated in full-size decks to simulate production conditions.

While the design for the Wittpenn Bridge incorporates the trends of a successful modern orthotropic deck design and economic fabrication, limited information exists on the fatigue performance of the orthotropic deck details, their fabrication, and their performance in service. Particularly critical of these details are the rib-to-deck plate and rib-to-floor beam welded connection details.

The design incorporated a thicker deck plate ${}^{(3}/_{4}$ in.) compared to conventional 5/8 in.) that reduced the demand on the rib-to-deck plate welded connections and possibility of wearing surface failure. While, the infinite life fatigue resistance of the rib-to-deck plate weld for ${}^{5}/_{8}$ in (16 mm) thick deck plates were generally well known from full-size fatigue tests, and no fatigue crack growth from the weld toe or the weld root is expected in thicker deck plates when adequately fabricated, only limited (unpublished) test results were available for this detail with ${}^{3}/_{4}$ in (19 mm) deck plate. These recent tests were conducted on full-scale but small-size specimens and tested at unrealistically high stress range levels in the finite life region, mostly for comparing alternative fabrication conditions.

Moreover, fatigue resistant design and economic fabrication of the rib-to-deck connection are significant from a LCC perspective. A cheaper fillet welded detail is not a prudent alternative for this connection. However, an economic fabrication of the PJP weld may be achieved by: a limited or no joint preparation; and by accepting a lesser penetration (up to 70%) and more variability in the penetration along the length, which is supported by recent research and has been adopted in the AASHTO LRFD Bridge Design Specifications. Additional cost saving may be achieved by less stringent requirements for repairs of melt-through condition, which as demonstrated by limited research does not have any tangible correlation to root cracking. Limited research also indicated that a smaller root gap between the rib and the deck plate before welding closes due to weld shrinkage and introduces compressive prestress at the weld root that prevents any fatigue cracking from the weld root. All these parameters needed to be addressed during fabrication of rib-to-deck plate weld for a cost-effective solution for production.

To reduce the cost of fabrication, the orthotropic deck design proposes rib-to-floor beam connections without cutouts and fillet welded all around. Although limited studies (Kolstein 2007) showed promise, infinite life fatigue performance of this rib-to-floor beam connection (without cutout) for the proposed geometric parameters of the deck was not known. Fatigue resistance of this connection depends on the LOF that inherently exists in all fillet welded details, and therefore fabrication of this detail would require stringent tolerance on fit-up and rigorous quality control to ensure the desired fatigue performance, which needed to be investigated during the fabrication of this connection for a cost-effective solution for production.

In addition to these, the response of orthotropic decks under wheel loads is quite complex that creates in-plane and out-of-plane stresses at the welded details as functions of the relative geometry of the connecting elements. Thus, the fatigue design of critical orthotropic deck details cannot be performed based on simple strength of material calculations. The complex behavior of proposed orthotropic deck needed to be simulated both in analysis and experiments for accurate fatigue assessment of the welded connections. Fatigue resistance of different welded details in orthotropic decks of varied configurations has not been established by laboratory testing, where the boundary effects have been adequately accounted for. Only a handful of such tests in the United States provided data on rib-to-deck plate weld detail and the rib-to-floor beam connections with cutout of particular geometric configuration, which were not readily applicable to the orthotropic deck details for Wittpenn Bridge. Similarly, the tests conducted in Europe and Japan were not applicable to the current project as they were mostly conducted on small specimens, where accurate boundary conditions were not replicated and deck sections employed antiquated practices and details. In addition, the newly introduced AASHTO provisions do not provide a reliable and consistent fatigue design methodology for infinite life of welded connections in orthotropic decks. Thus, full-size testing that adequately captures the behavior of orthotropic decks was the only rational means of evaluating in-service fatigue performance of orthotropic decks.

Based on the understanding of research problem and the background information, it was apparent that developing cost-effective fabrication of orthotropic deck details by testing full-scale mockup, and verifying the infinite life fatigue performance of the details by testing a full-size part deck specimen as well as finite element analysis (FEA) was the most rational approach for fulfilling the goals of this research project.

1.4 Objectives of the Current Study

The objectives of this study were:

1. to verify the infinite life fatigue performance of the proposed orthotropic deck for the replaced Wittpenn Bridge based on experimental and analytical studies according to the latest provisions of the AASHTO LRFD Bridge

Design Specifications and the FHWA Manual for Design, Construction, and Maintenance of Orthotropic Steel Bridges;

2. to develop cost-effective connection details and constructible system for fabricating the proposed orthotropic deck for the replaced Wittpenn Bridge; and
3. to simulate full-scale fabrication conditions, and to develop tolerances, inspection guides and quality control procedures for ensuring consistent, reliable and economic fabrication of the orthotropic deck using domestic resources;

1.5 Study Approach

The objectives of this research project were accomplished in three phases: Phase 1, Phase 2 and Phase 3, which are discussed in the flowing.

1.5.1 Phase 1: Preliminaries

Phase 1 included two tasks: Task 1 – Literature Search; and Task 2 – Amplify Research Plan. Task 1 dealt with a literature search focusing on issues related to fatigue design and fabrication of orthotropic bridge deck details. Based on the findings of the literature search in Task 1, the research plan as presented in Task 2 was refined and amplified to best suit the project objectives.

1.5.2 Phase 2: Analytical and Fabrication Studies

Phase 2 included three tasks: Task 3 – Perform Analytical Studies; Task 4 – Evaluate Fabrication Issues; and Task 5 – Finalize Test Plan. In Task 3, analytical studies were performed on the proposed orthotropic deck design for the Wittpenn Bridge: to decide a suitable full-size specimen that will sufficiently replicate the behavior of an entire deck in service; to determine the most critically stressed regions (details) in the deck; to determine the disposition of loads that will produce the most critical stresses; and to analytically predict the fatigue performance of the various critical details. The results of this analytical study helped in deciding the loading protocol for fatigue testing and developing an effective instrumentation plan during laboratory testing in the following phase (Phase 3). The influence of various fabrication parameters related to fabrication of orthotropic decks were evaluated in Task 4 by fatigue testing and destructive evaluation of small-size full-scale mockups with different welded connection details. WPS were developed for fabricating the full-size specimen. In Task 5, the test plan for the full-size testing was finalized.

1.5.3 Phase 3: Full-size Laboratory Studies

Phase 3 included five tasks: Task 6 – Develop Specimen and Fixture Designs; Task 7 – Fabricate Full-size Specimen; Task 8 – Prepare Test Setup; Task 9 – Conduct Experimental Studies; and Task 10 – Evaluate Test Results. In Task 6, finer refinements were made to the full-size specimen, and the fixtures were designed to implement the test plan. Task 7 dealt with the fabrication of the full-size specimen. In Task 8, the test setup was installed at ATLSS Center and laboratory testing of the full-scale full-size specimen was conducted in Phase 9. In Phase 10, the test results were evaluated and destructive evaluation of the rib-to-floor beam welds were performed.

1.6 Outline

This report contains 10 chapters and 14 appendices. The first chapter introduces the background and the problem statement for the research project. Review of available literature was included in the Quarterly Progress Report (dated 09/23/2012). The rationale for the study, the study objectives and the study approach are also provided in the first chapter, in addition to the outline of the report.

The remaining chapters correspond to Phase 2 and Phase 3 studies. The activities undertaken in Phase 2 are reported in Chapters 2 to 5, and the activities undertaken in Phase 3 are reported in Chapters 6 to 10.

The second chapter discusses the FEA of the full bridge deck identified as global model (GM) and FEA of the part of deck identified as submodel (SM). Determination of the most fatigue critical connection and corresponding wheel load dispositions based on FEA, and the corresponding fatigue critical stresses at the welded connection are discussed in this chapter.

The third chapter discusses the design of the mockup specimens and the results of the mock specimen FEA. It also discusses the test setup for testing the mockup specimens. The chapter also provides the details of the instrumentation, loading and the tests conducted.

The fourth chapter discusses the static test results of the mockup specimens. The response of important deck elements and fatigue critical details under static loading are discussed in this chapter. The chapter also provides the fatigue test results of the mockup specimens including the observed fatigue cracks and assessment of fatigue resistance.

The fifth chapter discusses the findings of the post-mortem studies when the fracture surfaces of the mockup specimens were exposed to determine the origin of fatigue crack. The chapter also discusses the findings of the metallographic studies conducted by macro-etching multiple cross sections of rib-to-floor beam and rib-to-deck plate connections of the mockup specimens.

The sixth chapter discusses the design of the Phase 3 full-size specimen and the test setup for fatigue testing. It discusses the gradual development of the full-size specimen from the previous levels of FEA.

The seventh chapter discusses the fabrication studies of additional mockups which were used to develop WPS. The chapter also provides the information of fabrication of the full-size specimen.

The eight chapter discusses the test setup for testing the full-size specimen. The chapter also provides the details of the installation of the deck specimen, instrumentation, loading and the tests conducted.

The ninth chapter discusses the static test results of the prototype deck specimen. The response of important deck elements and fatigue critical details under static loading are discussed in this chapter. It also provides the fatigue test results of the prototype deck specimen including assessment of fatigue resistance.

The tenth chapter discusses the finding of the destructive evaluation of the rib-to-floor beam welds of the full-size specimen.

Figure 1. The Wittpenn Bridge
(http://www.state.nj.us/transportation/commuter/roads/rt7wittpenn/)

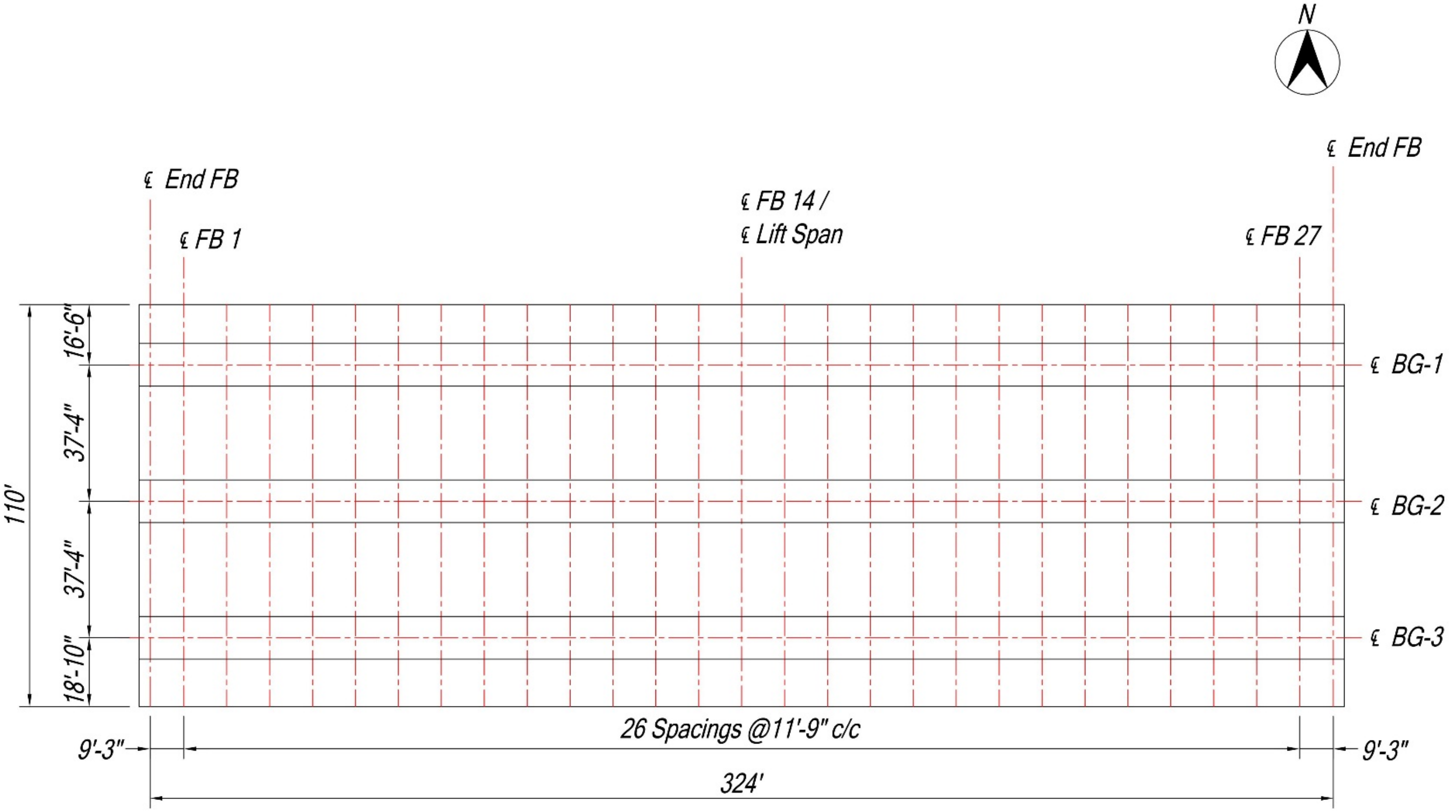

Figure 2. Framing plan of the bridge deck

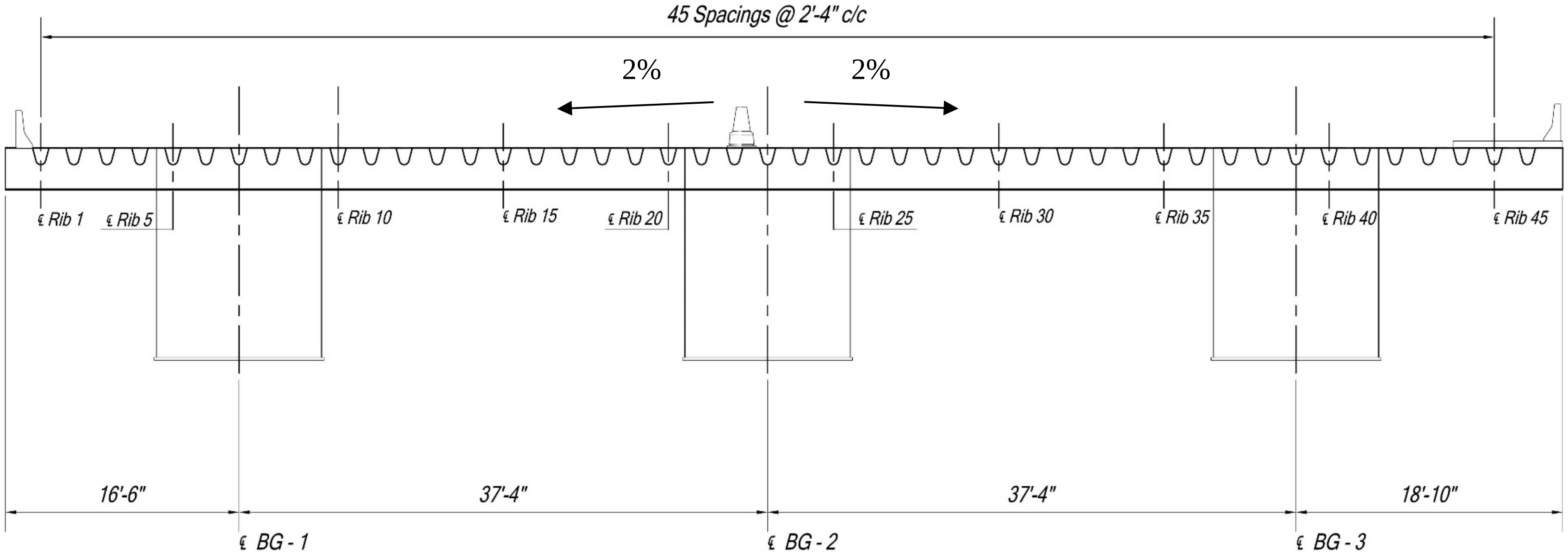

Figure 3. Cross section of the deck at floor beam (slope of deck not drawn)

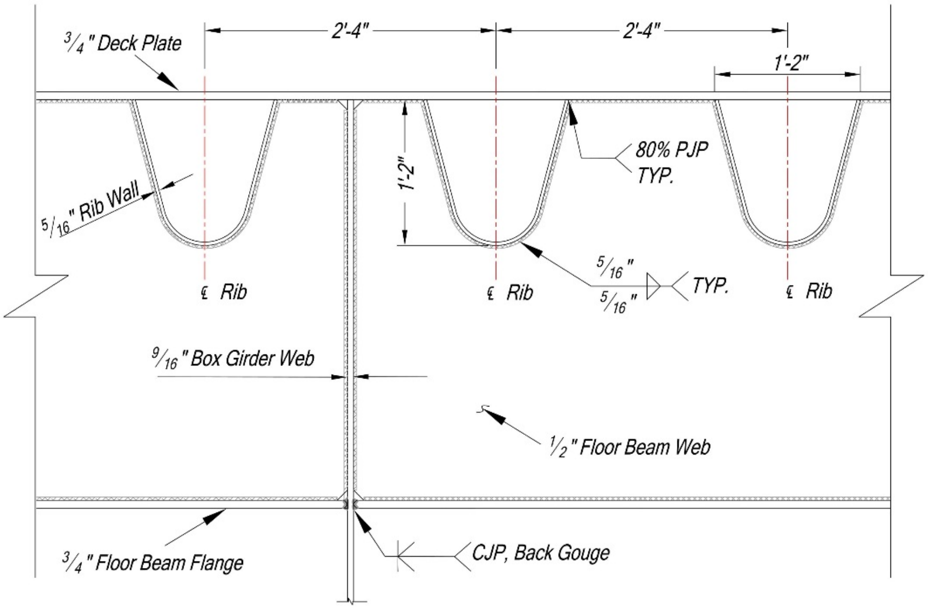

Figure 4. Design deck details

2. ANALYTICAL STUDIES

2.1 Analysis Plan

The activities undertaken in Task 3 of the research project related to the analytical studies of the proposed orthotropic deck for Wittpenn Bridge are reported in this chapter. Linear elastic FEA was conducted: to determine the most critically stressed region of the deck; to determine the disposition of loads that will produce the most critical stresses; to analytically predict the fatigue performance of the various critical details and finally to decide a suitable full-size specimen for fatigue testing that will sufficiently replicate the behavior of an entire deck in service. A 3D FEA of the entire proposed lift span of the Wittpenn Bridge superstructure was performed to understand its behavior and the distribution of stresses in the bridge deck under vehicular live loads as specified by the latest provisions of the AASHTO LRFD Bride Design Specifications, and to determine the most critically stressed region of the deck and the corresponding live load dispositions for the deck components. The FEA was conducted by ABAQUS (3) (a commercially available finite element analysis software suite) using shell elements. This model is identified as Global Model (GM). Welds were not modelled in the global model. In order to get the fatigue critical stresses at the welded connections, a 3D solid submodel (SM) was constructed of the deformed region of the GM, and was analyzed using ABAQUS with all the weld details included in the SM. The results of the GM and the SM analyses were used to design the mockup specimens for Phase 2 and the full-size specimen for Phase 3 of the research project. The FEA of the GM and the SM that were conducted in Task 3 of the research project are reported in this chapter. 3D solid models of the mockup specimens and the full-size specimen were also constructed, which replicated the test specimens. The FEA of the specimen models are discussed later in this report in their respective chapters.

2.2 FEA of GM

2.2.1 <u>Modelling Detail</u>

The GM is shown in Figure 5. All components of the deck namely, the deck plate, the ribs, the floor beams, the box girders and the end floor beams were included in this model. These were modelled according to the design drawings provided by NJDOT. The components were modelled as separate parts. The welds were not modelled; all welded connections were considered integral. The effect of weld notch was studied in subsequent levels of FE models where all the welds were incorporated.

The GM was developed using shell elements. Shell elements were preferred, keeping in mind the computational demand that would have resulted by use of solid elements. All components were modelled by defining the geometry at the middle surface of each. Figure 6 shows the cross section of a typical rib and a floor beam with the dimensions of the middle surface marked. Figure 7 shows the cross section of a typical box girder and an end floor beam with the dimensions of the middle surface marked as designed and as modelled. The depth of the floor beams are variable for the Wittpenn Bridge with 4 ft. at the center and gradually reducing towards the end with a slope of 2%. The average depth of the floor beams are about 3 ft. 4 in. However, an average nominal depth of 3 ft. (914 mm) was used for modelling the floor beam (inclusive of the deck plate), as was stated in the NJDOT Project Proposal. The choice of the floor beam depth was conservative as it reduced the shear area for in-plane stresses and also reduced out-of-plane rotational flexibility of the floor beam. As such, the choice of floor beam depth didn't underestimate the stresses at the connection.

2.2.2 Material Properties

Widely accepted linear elastic material properties of steel were used for analysis. The modulus of elasticity and Poisson's ratio of steel were assumed as 29000 ksi (2.0x105 MPa) and 0.3 respectively.

2.2.3 Choice of Elements and Meshing

The GM was meshed with doubly curved, thick shell elements having eight nodes and incorporating quadratic, reduced integration and isoparametric formulation. In ABAQUS, this element is designated as S8R. The mesh was generated automatically by ABAQUS. with an average element size of approximately 7 in (178mm) resulting in 891,164 elements, 2,609,646 nodes, and 15,657,876 solution variables or nodal degrees of freedom. All the components or parts were meshed separately using structured meshing technique. The meshed components were merged to form the meshed deck model. The average aspect ratio of the element was about 3 with the largest aspect ratio of about 7. The average maximum and minimum of the corner angles were about 91° and 89° respectively. The quality of meshing was in accordance to the standards specified by ABAQUS. A comparison of the element shape selection criteria limits between the GM and as specified by ABAQUS is presented in Table 1.

2.2.4 Boundary Conditions

The boundary conditions of the GM replicated the boundary conditions of the full bridge deck in service. As per the design drawings provided by NJDOT, the end floor beams to the east and the west sides of the deck were connected to the east and the west towers respectively. These towers were placed on the east and the west piers by expansion bearing and fixed bearing respectively. These bearings were simulated by consistent displacement boundary conditions imposed at the soffit of the end floor beams, coincident with the proposed bearing locations on the physical bridge (Figure 8). Displacement boundary conditions restraining displacements in all three coordinate directions were imposed at the underside of the west end floor beam to simulate fixed condition. Displacement boundary conditions releasing displacement in the longitudinal direction of the deck and restraining displacements in the other two directions, were imposed at the underside of the east end floor beam to simulate roller support or expansion bearing.

2.2.5 Loading

The GM was analyzed for 5 longitudinal positions of the AASHTO fatigue design truck for Fatigue I Limit State as recommended by the latest AASHTO provisions. The longitudinal load positions are shown in Figure 9. Corresponding to each longitudinal position, the transverse load positions were decided starting from the south side of the bridge and gradually moving towards the north side. The transverse load positions are shown in Figures 10 to 25. The criticality of the load position was decided in terms of the fatigue critical stresses normal to the weld toe at the rib-to-floor beam welded connection both on the floor beam web and the rib wall. The transverse load positions appear discontinuous as the intermediate load positions are not shown as the stresses normal to the weld toe at the fatigue critical locations due these load positions were insignificant. In this report, the load cases are identified by the longitudinal load position (e.g. L1, L2, etc.) suffixed by the transverse load position (e.g. T1, T29, T30).

The loads were positioned around FB14, the floor beam at the mid span of the bridge deck, which was expected to produce the maximum global deformations of the deck, and any associated effect on the local stresses in the deck. The longitudinal load positions were chosen as to simulate the passing of an AASHTO tandem axle over the span of the deck between FB 14 and FB 13. The first longitudinal load position was chosen such that the tandem axle was symmetric with respect to FB 14 to produce symmetric response of the FB 14. The subsequent load positions were chosen to represent the gradual passage of the axle over the span between FB 14 and FB 13 and to investigate the asymmetric response of FB 14 under the combined effects of in-plane and out of plane deformation of the floor beam due to the rib rotation.

The load from the deck plate is transferred to the box girder through the floor beam as shear. Consequently in the shear span, a diagonal tension field is formed from the bottom flange (tension flange) of the floor beam to the top corner formed by the floor beam, the box girder and the deck plate. This tension field deviates around the cutout in the floor beam due to the discontinuity, and causes high stress concentration at the rib-to-floor beam connection near the rib rounding. Accordingly, the transverse load positions were chosen to simulate different shear spans, covering all possible cases of shear at the floor beam-to-box girder connection, creating different magnitude of stress concentration at the rib-to-floor beam connection. In addition, the transverse load positions also covered all possible response of the deck components in the transverse direction. The truck was positioned such that either one wheel or both wheels of the left wheel pair was located symmetrically between the ribs, on a rib wall, or over a rib. These placements of the left wheel pair also resulted in dispositions of the right wheel pair, where the deck plate over the ribs or between the ribs was loaded in different configurations. As a result, the deck plate and the ribs, whose responses are driven by local effects of individual wheels, were subjected to several different load conditions, where the wheels (tire contacts) were positioned partially or fully between the rib walls, or on the rib walls. These load positions generated all possible critical stress states in the deck plate, the rib walls and rib-to-deck plate connections.

2.2.6 Analysis

The GM was analyzed on distributed memory computer cluster of 8 nodes, each having 16 central processing units (cpu). All analyses were linear elastic. The load magnitude was set to vary linearly over the step, from the value at the end of the previous step (or zero, at the start of the analysis) to the given load value. All analyses used the direct linear equation solver and converged in a single increment. The direct linear equation solver used a sparse, direct, Gauss elimination method that found exact solution of this system of linear equations (up to machine precision.

2.2.7 Analysis Results

Comparison of Deck Response under Different Load Cases

The FEA of the GM showed high stress concentration in the floor beam and the rib wall at the Rib 10-to-FB 14 welded connection. Rib 10 was adjacent to box girder BG-1 and FB 14 was at the midspan of the deck around which the loads were positioned. Comparison of deck response as obtained from different load cases are presented in Figures 20 to 23 in terms of variation of stresses normal to weld toe at the Rib 10-to-FB 14 connection. The paths along which the stresses were plotted (the abscissa or the x-axis of the plots), and the direction of stresses are identified in the figures on the section view. The results for 6 transverse load positions are shown in the plots, as the stresses due to the other load positions were insignificant.

Figure 20 shows the variation of tensile stresses normal to weld toe in floor beam web at the rib-to-floor beam connection for L1. The origin of the path corresponds to the soffit of the rib and the path circumvents the connection following the rib rounding. The maximum tensile stress was observed for T29 and was about 4.3 ksi. The location of maximum stress was about 56° from the rib soffit. This load position generated higher shear forces in the floor beam web and critical stresses at the Rib 10-to-FB 14 connection. Figure 21 shows the variation of tensile stresses normal to weld toe in floor beam web at the rib-to-floor beam connection for L2. The origin of the path corresponds to the soffit of the rib and the path circumvents the connection following the rib rounding. The maximum tensile stress was observed for transverse load positions 29 and 30 and was about 3.7 ksi. Note that L2 produced both in-plane and out-of-plane stresses in the floor beam web. However, stresses due to L2 were less than L1. This is because sufficient floor beam depth was available below the soffit of the rib which provided the out-of-plane flexibility of the floor beam web and reduced the out-of-plane stresses in the floor beam web.

Figures 22 and 23 show the variation of tensile stresses normal to weld toe on rib at the rib-to-floor beam connection for L1 and L2 respectively. The origin of the path corresponds to the soffit of the rib and the path circumvents the connection following the rib rounding. The maximum tensile stress was observed for T29 corresponding to L1 and was about 3 ksi. The maximum tensile stress for L2 was lower and was about 1.8 ksi. As it was discussed earlier, deeper depth of the floor beam provided the out-of-plane flexibility of the floor beam web and reduced the stresses due to out-of-plane effects of the wheel load.

Figures 24 and 25 show the variation of tensile stress normal to weld toe in floor beam at the Rib 10-to-FB 14 connection for L1 and L2 respectively. The origin of the path corresponds to the maximum stress point location and continues radially outward from the connection. Similar behavior was observed for all the transverse load positions with high tensile stress at the weld toe and gradually becoming compressive away from the weld toe.

For the above comparison, it is evident that the transverse load position T29 corresponding to longitudinal load position L1 produced the most critical stresses normal to weld toe at the Rib 10-to-FB 14 connection, when the tandem axles were symmetrically placed about the floor beam (Figure 9). For this load case, the center line of the tandem axle was 11 ft. from the center line of BG-1 (or 5 ft. 4 in. from the box girder web). Accordingly, analysis of subsequent levels of FE models and also the fatigue testing in both Phase 2 and Phase 3 were conducted for load case L1T29. The FEA results shown in the following sections are shown for load case L1T29.

Behavior of the Deck Plate and the Ribs

The 3D view of the deformed shape of the bridge deck is shown in Figure 26, scaled to 300x. Figure 27 shows the zoomed underside view of the portion of the deck in which the loads were positioned for FEA. As is seen from the two figures, the deck deformation was characterized by global longitudinal bending of the ribs and transverse bending of the floor beams, and significant local transverse bending of the deck plate under the load patches. Deformation of the deck plate beyond the load patches was insignificant. The response of the deck plate and the ribs was investigated by comparing the defected shape of the deck at two transverse sections and two longitudinal sections. The sections are shown in Figure 28. Transverse sections A-A and B-B are aligned with the centerline of west pair of load pads and the centerline of FB 14 respectively. Longitudinal sections C-C and D-D are aligned with the centerline of the south and the north pair of load pads respectively.

Figures 29 and 30 show the overlay plots (deformed shape of the deck overlaid on the undeformed shape of the deck) for the bridge deck at sections A-A and B-B respectively, scaled to 50x. As is seen from the figures, the local transverse bending the deck plate was more at the section A-A than at the section B-B. Figure 31 shows the overlay plot comparing the deformed shapes of the deck at sections A-A and B-B, scaled to 50x. As also noted previously, the deck plate underwent local transverse bending at section through the load pads much more compared to the section through the centerline of floor beam. In addition, the deformation of the deck plate away from the load pads was negligible. Zoomed views of the portions of the deck around the load patch are shown in Figures 32 and 33. It could be seen from Figure 32 that the deck plate deformed in a sagging curvature under the load pads between the two ribs and in a hogging curvature over the rib wall. Figure 33 shows that the deck plate deformed in a sagging curvature under the load pads inside the rib and in a hogging curvature over the rib wall. Due to the framing action between the rib wall and the deck plate, the rib walls under the north and the south pair of load pads deformed in different curvatures. The deformation of the deck plate and the rib wall was essentially local under the wheel loads and the rib walls and the rib-to-deck plate connections underwent local out-of-plane bending under the wheel loads.

The contours of maximum principal stress in the deck (deformed configuration scaled to 300x) are shown in Figures 34 to 36 under load disposition L1T29. Two way deformation of the deck was observed with high stresses and deformation of the deck plate locally under the load pads. Figures 35 and 36 show the zoomed views of the deck top and deck bottom stresses around the load pads. As it could be seen from the figures, the deck plate stresses were significant locally under the load patches with compressive stresses on the top and tensile stresses on the bottom of the deck plate.

The distribution of longitudinal stresses on the top of deck plate at sections C-C and D-D is shown in Figure 37. The path along which the stress variation was plotted (the abscissa or the x-axis of the plots) and the direction of stress is identified in the section view of the deck. The origin of the path corresponds to the centerline of FB 13. As expected, the deck plate underwent flexural deformation spanning continuously between the ribs and the stresses peaked locally under the load pads. The compressive stresses were as high as 25.5 ksi and 19.1 ksi at sections C-C and D-D respectively. The stresses were symmetric on either side of FB 14 as loads were positioned symmetrical on either side of FB 14. The distribution of longitudinal stresses on the bottom of deck plate at sections C-C and D-D is also shown in Figure 38. As expected, the stresses peaked locally under the load pads, but following opposite trend to that of the stresses on the top of the deck plate. The tensile stresses were as high as 23 ksi and 16.3 ksi at sections C-C and D-D respectively. The stresses were symmetric on either side of FB 14 as loads were positioned symmetrical on either side of FB 14. As it can be observed, the stresses on the top and the bottom of the deck plate were almost of equal magnitude with little membrane stresses.

Variation of transverse and longitudinal normal stresses on the top surface of the deck plate at the transverse section A-A are shown in Figure 39. The path along which the stress variations were plotted (the abscissa or the x-axis of the plots) is identified in the section view of the deck. The origin of the plot corresponds to the right wall of BG-1 and ends at the left wall of BG-2. The stresses in the deck plate were significant locally under the load pads. The transverse stresses were more as the deck plate predominantly underwent flexural deformation spanning continuously between the ribs. At section C-C, the stresses were compressive between the ribs and tensile over the ribs. The deck plate deformed in a sagging curvature under the load pads in between the two ribs and in a hogging curvature over the rib wall (refers Figure 32). At section D-D, the stresses were compressive inside the rib and tensile over the rib walls. The deck plate deformed in a sagging curvature inside the rib and in a hogging curvature over the ribs (refer Figure 33).

Distribution of longitudinal normal stresses along the bottom surface of rib 10 for load case L1T29 is shown in Figure 40. The path along which the stress variation was plotted (the abscissa or the x-axis of the plots) and the direction of stress is identified in the section view of the deck. The origin of the plot corresponds to the centerline of FB 13. The stress profile resembled the bending moment distribution of a continuous beam spanning between the floor beams and subjected to concentrated load symmetrically on either side of FB 14. As expected, the maximum tensile stresses occurred under the wheel load, symmetrical on either side of FB 14. The rib deformed in a sagging curvature under the wheel load and in hogging curvature over the support (or FB 14). The maximum tensile stress at the bottom of rib 10 was about 1.2 ksi.

Behavior of the Floor Beams

The deformed configurations of FB 13 and FB 14 are shown in Figure 41 under load cases L1T29 and L2T29 respectively, scaled to 500x. As discussed in section 2.2.5, the loads were positioned around FB14, the floor beam at the mid span of the bridge deck, to produce the most critical global deformations. So, the displacement of FB 14 was more than the displacement of FB 13. The displacements of FB 13 and FB 14 are also compared in Figure 42. The displacements of the floor beams were almost similar away from the load, but FB 14 displaced more under the wheel loads. FB 14 essentially deflected like a propped cantilever with support settlement at BG-1, however, FB 13 deflected like rigid body with support settlement.

The in-plane bending moment diagram of FB 14 is shown in Figure 43. The moment diagram is similar like a continuous beam supported by the box girders. The moment was maximum under the wheel loads, so the maximum displacement also occurred under the load. Figure 44 shows the maximum principal stress contour for the bottom surface of the floor beam flange and the external surface of the rib wall. As expected, the stresses at the bottom surface of the floor beam flange were tensile as the floor beam deformed in a sagging curvature in between the box girders BG-1 and BG-2. Figure 45 shows the distribution of transverse stresses along the bottom surface of the floor beam flange at section B-B for load cases L1T29 and L2T29. The path along which the stress variation was plotted (the abscissa or the x-axis of the plots) and the direction of stress is identified in the section view of the deck. The origin of the path corresponds to the left wall of BG- 1 and ends at the right wall of BG-2. The maximum tensile stresses in the floor beam flange were about 4.8 ksi and 4.6 ksi for load cases L1T29 and L2T29 respectively. The stress envelope resembled the variation of bending moment in a continuous beam spanning between the box girders with sagging curvature in the span and hogging curvature over the support (or over the box girders).

The contours of maximum in-plane principal stress in FB 14 are shown in Figures 46 and 47, for load cases L1T29 and L2T29 respectively. Since the floor beams were integral with the box girder, the wheel loads were transferred to the box girder (BG-1) through the floor beam by shear. In both the load cases, the transfer of wheel loads as shear to the box girder resulted in a diagonal tension field from the bottom (tension) flange to the top corner formed by the floor beam web and the box girder web. The shear induced tensile stress in the floor beam web was interrupted by the cutouts, and the stress field deviated around the cutout. As a result, high stress concentration developed in the web of the of the floor beam where the tension fields were approximately tangential to the cutout. As weld was not modelled in the GM, the effect of weld toe notches at the rib-to-floor beam connections which also contributed as stress raisers, were studied in the SM. The maximum principal stress was determined to be 11.3 ksi and 10.4 ksi for load cases L1T29 and L2T29 respectively. In both the load cases, the maximum stress occurred along the diagonal tension field at Rib 10 adjacent to BG-1: in the floor beam web adjacent to the rib rounding at the Rib 10-to-FB 14 connection. However, as is well known, the nominal fatigue resistance of the base metal is higher than the welded connections. Hence, the Rib 10-to-FB 14 connection was expected to develop fatigue cracking.

As is evident from Figures 46 and 47, the stresses were higher for load case L1T29 when the loads were placed symmetrically on either side of FB 14. Out-of-plane bending of the floor beam web due to rotation of the rib was expected to occur at the rib-to-floor beam connection. In that case, load L2T29 would have been more critical. However, L2T29 was not critical as sufficient floor beam depth was available below the soffit of the rib which provided the out-of-plane flexibility of the floor beam web and reduced the out-of-plane stresses in the floor beam web. Figure 48 shows the variation of the stress normal to the weld toe of the Rib 10-to-FB 14 connection on the two faces of FB 14 web along a radial path. The origin of the path corresponds to the maximum stress point location and continues radially outward from the rib-to-floor beam connection. The stresses were primarily in-plane. The out-of-plane stress component was minimal in L2T29. The value was maximum at the weld toe and stayed constant for a distance of about 3 in. As the distance increased further, the out-of-plane component decreased rapidly and became primarily in-plane. For L1T29, there was no out-of-plane bending as the loading was symmetric to FB 14.

2.3 FEA of SM

2.3.1 Details of the SM

The FEA of the GM identified the rib-to-floor beam connection (Rib 10-to-FB 14 connection) adjacent to one of the box girders as the most critically stressed region of the deck. The tandem axles symmetric with respect to the floor beam in the longitudinal direction (L1), and with the wheels nearest to the box girder placed centrally between the adjacent pair of ribs (T29) produced the most critical stress state at the rib-to-floor beam connection. GM analysis showed that the response of the deck under the tandem axles in the most critical load disposition were limited to three floor beams in the longitudinal direction as shown in Figure 49. Based on this observation, it was decided to include three floor beams in the SM as shown in Figure 50. GM analysis also showed that the floor beam essentially deflected like a propped cantilever with some settlement at the box girder Figure 51. However, the curvature of the transverse deflection was limited to few ribs (Figure 51) locally where the load was applied. So, it was decided to include the portion of the deck in between the box girders for consideration in the SM. Accordingly, a SM consisting of the ribs between the two box girders (BG-1 and BG-2), part of the box girder webs, a single rib on the other side of the box girder webs and three floor beams was developed. The extent of the SM is shown in Figure 52 overlaid on the plan view of the GM. The SM included a 35 ft. 3 in. length of the deck symmetric about FB 14 and contained ribs 10 to 20 between box girders BG-1 and BG-2 and ribs 9 and 21 on the other side of BG-1 and BG-2 respectively. The width of the model was 30 ft. 4 in. In the transverse direction the SM was symmetric about Rib 15. The boundaries of the SM in the longitudinal direction was 5 ft. 10 ½ in. from the centerline of FB 13 and FB 15, which were respectively half the spacing between two consecutive floor beams. All the weld details were included in the SM and the welds were modelled as $^{5}/_{16}$ fillet welds with idealized zero notch radius at the weld toes and complete penetration at the weld root. The modelled weld details in the SM provided the fatigue critical stresses at the welded connections, which were used in determining the size of the test specimens.

2.3.2 Material Properties

Widely accepted linear elastic material properties of steel were used for analysis. The modulus of elasticity and Poisson's ratio of steel were assumed as 29000 ksi and 0.3 respectively.

2.3.3 Element Type and Meshing

The SM was meshed with 3D continuum solid hexahedral elements, incorporating twenty node, quadratic, reduced integration and isoparametric formulation. In ABAQUS, this element is identified as C3D20R. The mesh was generated automatically by ABAQUS with an average element size of approximately 1 in (25 mm) resulting in 160,3140 elements, 823,1042 nodes and 2,469,3126 solution variables or nodal degrees of freedom. The SM was meshed with an average minimum mesh size of 1 in. and an average aspect ratio of about 6. The average maximum and minimum corner angles were about 85° and 95° respectively. The quality of meshing was in accordance to the standards specified by ABAQUS.

2.3.4 Loading

The SM was analyzed for the most critical disposition of the tandem axles as determined from GM analysis. The load position in elevation and plan are shown in Figures 51 and 52 respectively. The SM was analyzed for longitudinal load position L1 corresponding to transverse load position T29, which was determined from GM analysis to produce the most critical stress state at the rib-to-floor beam connection adjacent to the box girder. The load from each wheel pair of the tandem axle was uniformly distributed over a rectangular load pad of 10 in. long and 20 in. wide as specified by AASHTO LRFD Bridge Design Specifications. These load patched are identified as LP in Figure 52. Although a transverse gap of 1 in. exists in the middle of each wheel pairs, it was ignored in the idealized rectangular wheel contact for simplicity in modelling. Each pair of load patches represented one tandem axle. As seen from Figure 52, the tandem axles were symmetrically placed 2 ft. on either side of FB 14 resulting in a spacing of 4 ft. between the two axles, and in transverse direction the load pads were spaced 6 ft. apart. The spacing between the tandem axles in the longitudinal direction and the spacing between the load pads in the transverse direction were consistent with the latest provisions of the AASHTO LRFD Bridge Design Specifications. The total load applied on the deck was 82.8 kip, which is three times the AAHTO fatigue design load (0.75×HS20 + 15% impact) as specified by AASHTO for Fatigue I limit state design of orthotropic decks. This resulted in a total load of 41.4 kip per axle or 20.7 kip per wheel pair or load pad. This resulted in a uniformly distributed pressure load of 0.1035 ksi per load pad which was applied on LPs in the SM.

2.3.5 Boundary Condition

The global-to-local SM analysis employed shell-to-solid sub-modelling, where the SM was driven by the displacement solution of the GM at the common interface.

2.3.6 Analysis

Similar to the GM, the SM was analyzed on distributed memory computer cluster of 8 nodes, each having 16 central processing units (cpu). All analyses were linear elastic. The load magnitude was set to vary linearly over the step, from the value at the end of the previous step (or zero, at the start of the analysis) to the given load value. All analyses used the direct linear equation solver and converged in a single increment. The direct linear equation solver used a sparse, direct, Gauss elimination method that found exact solution of this system of linear equations (up to machine precision.

2.3.7 Analysis Results

The contours of maximum principal stress in the deck are shown in Figures 53 and 54. in the deformed configuration of the deck from the top and underside view of the deck respectively. The stresses are presented for a total load of 82.8 kip. Similar to the GM, the deformed configuration of the deck shows that the deformations were concentrated under the load patches and decreased rapidly away from the load patches. It can also be seen that the maximum principal stresses were highly localized under the load patches as is seen as black patches, and away from the load the stresses were insignificant.

Figure 55 compares the deformed configuration of FB 13 and FB 14. It can be clearly seen that the deformation of FB 14 was much more compared to FB 13 whose deflection was practically negligible. FB 13 essentially deflected like a rigid body with settlement at the box girders. On the other hand, FB 14 deflected like a propped cantilever with settlement at the girder edges. So, it can be said the deformation of the deck was highly localized as FB 14 about which the loads were placed deflected much more as compared to FB 13 which was far away from the loads. This can also be seen from the principal stress contours of FB 14 and FB 13 presented in Figures 56 and 57 respectively. The maximum value of principal stress in FB 14 was about 12.3 ksi, whereas it as only about 2.4 ksi in FB 13.

Since the floor beam was integral with the box girder, the wheel loads were transferred to the box girder through the floor beam by shear. The transfer of wheel loads as shear to the box girder resulted in a diagonal tension field from the bottom (tension) flange to the top corner formed by the floor beam web and the box girder web. The shear induced tensile stress in the floor beam web was interrupted by the cutouts, and the stress field deviated around the cutout. As a result, high stress concentration developed in the web at the rib-to-floor beam connection of the of the floor beam where the tension fields were approximately tangential to the cutout. The rib-to-floor beam connection (rib 10 adjacent to the box girder) also contributed to the increase in stress due to the presence of the sharp notch at the weld toe. Stresses were tensile at the connection towards the box girder side and compressive on the other side. As such, the high stress concentration was observed at the Rib 10-to-FB 14 connection (Figure 56) in SM analysis, similar to the GM analysis; and hence this connection was identified as most fatigue critical corresponding to the most critical disposition of the tandem axles.

The stresses obtained from the SM analysis provided the fatigue critical stresses at the rib-to-floor beam connection, which was the basis for designing the mockup specimens for Phase 2 and the full-size specimen for Phase 3.

Table 1 – Element shape selection criteria limits

Selection Criterion	ABAQUS Specified Limits	GM	
		Average	Worst Case
Smaller Face Corner Angle	10°	89°	32°
Larger Face Corner Angle	160°	91°	138°
Aspect Ratio	10	3	7

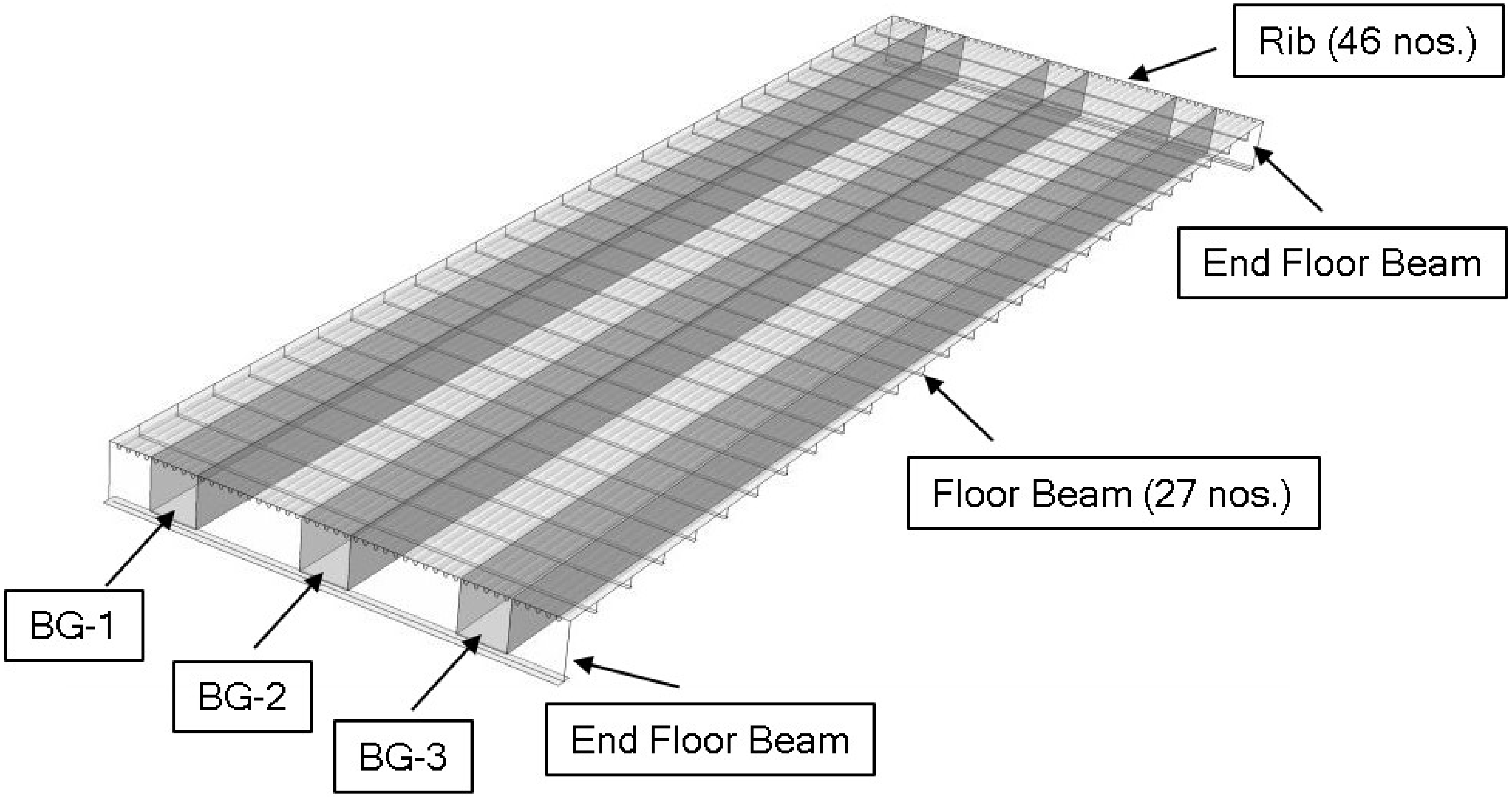

Figure 5. GM: top view

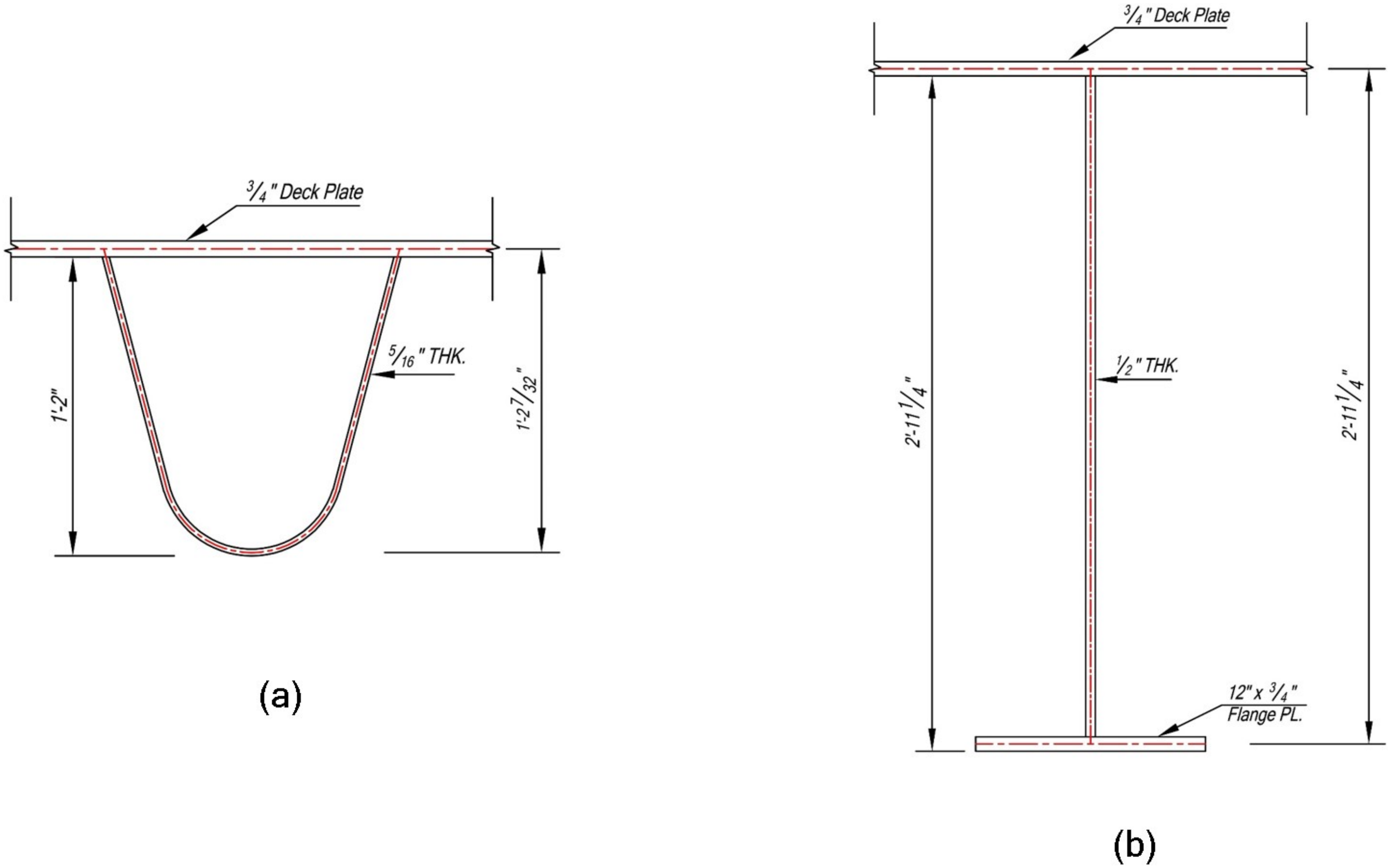

Figure 6. Cross section: (a) rib; (b) floor beam

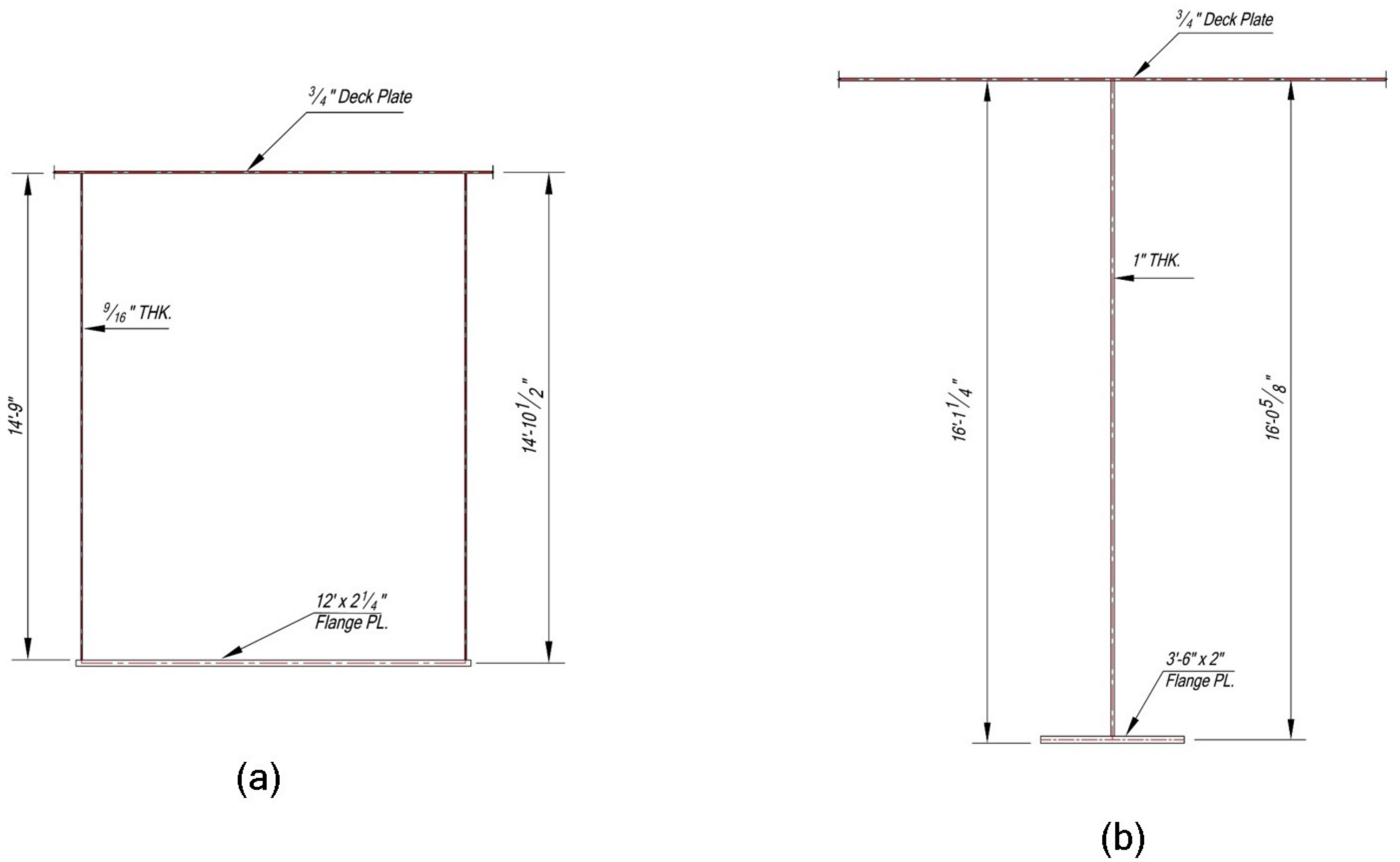

Figure 7. Cross section of: (a) box girder; (b) end floor beam

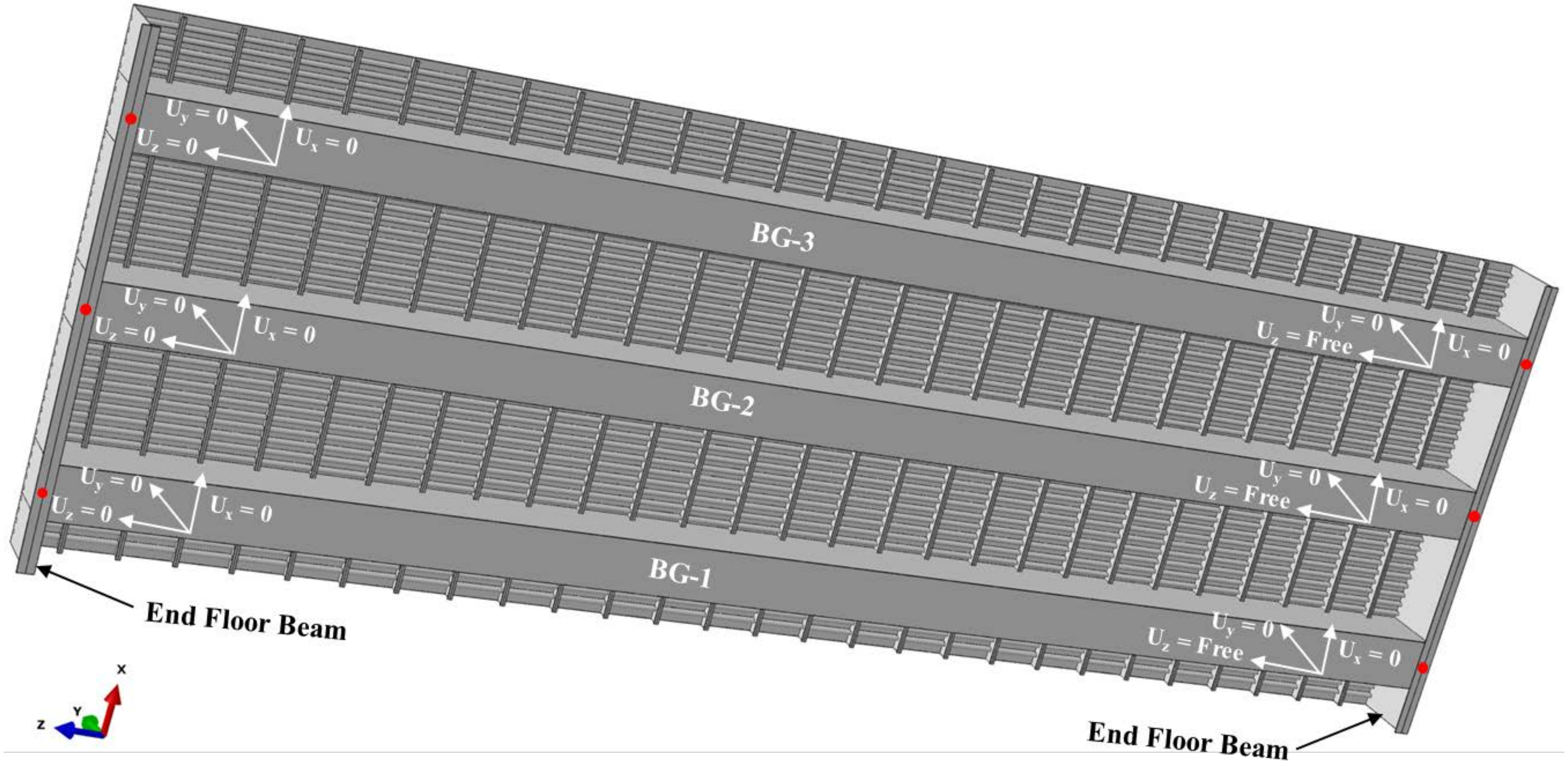

Figure 8. 3D FE model of the bridge deck – underside view showing the boundary conditions specified at the soffit of the end floor beams at locations identified as dots.

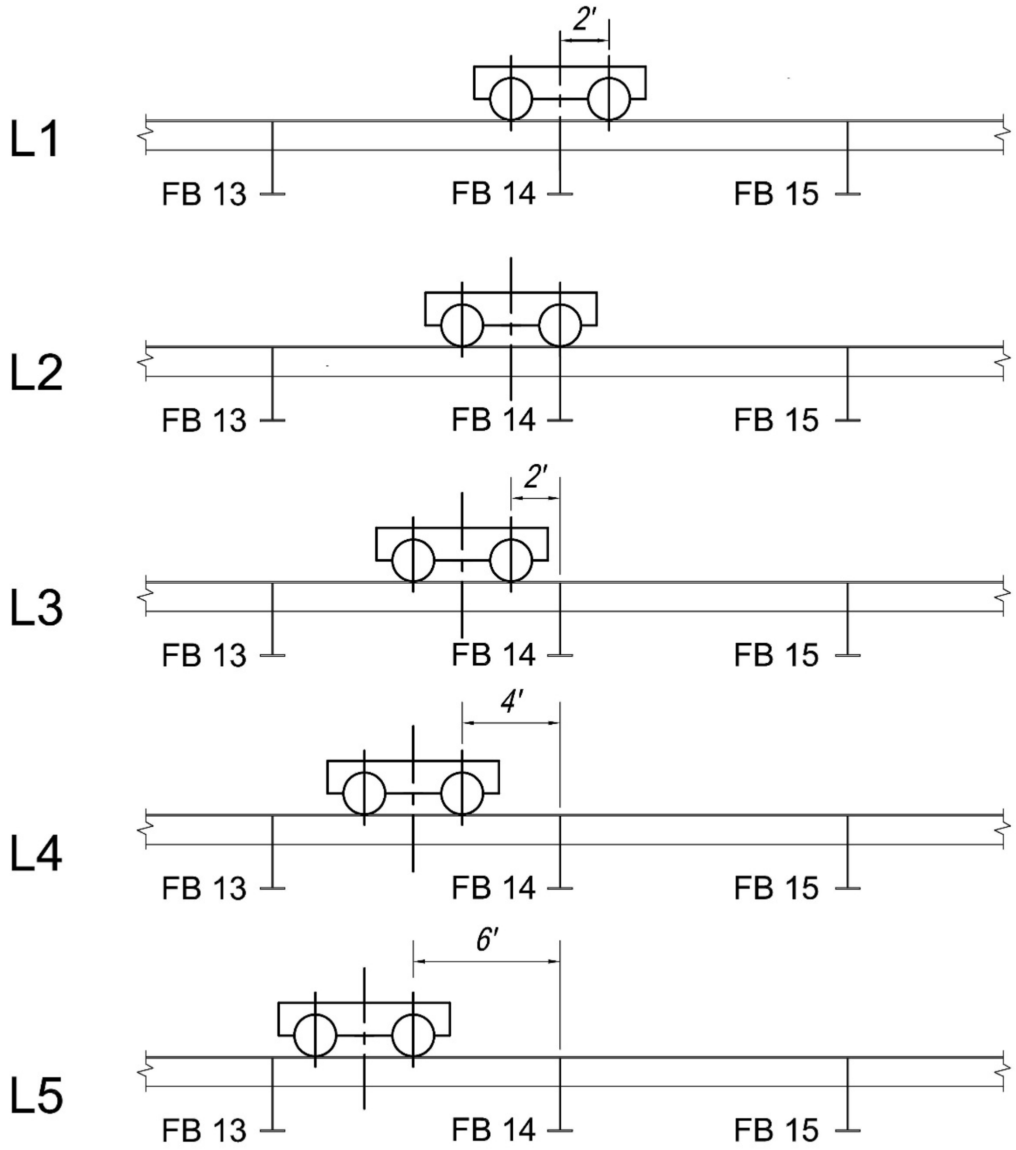

Figure 9. Longitudinal disposition of AASHTO tandem axles considered for FEA of bridge deck

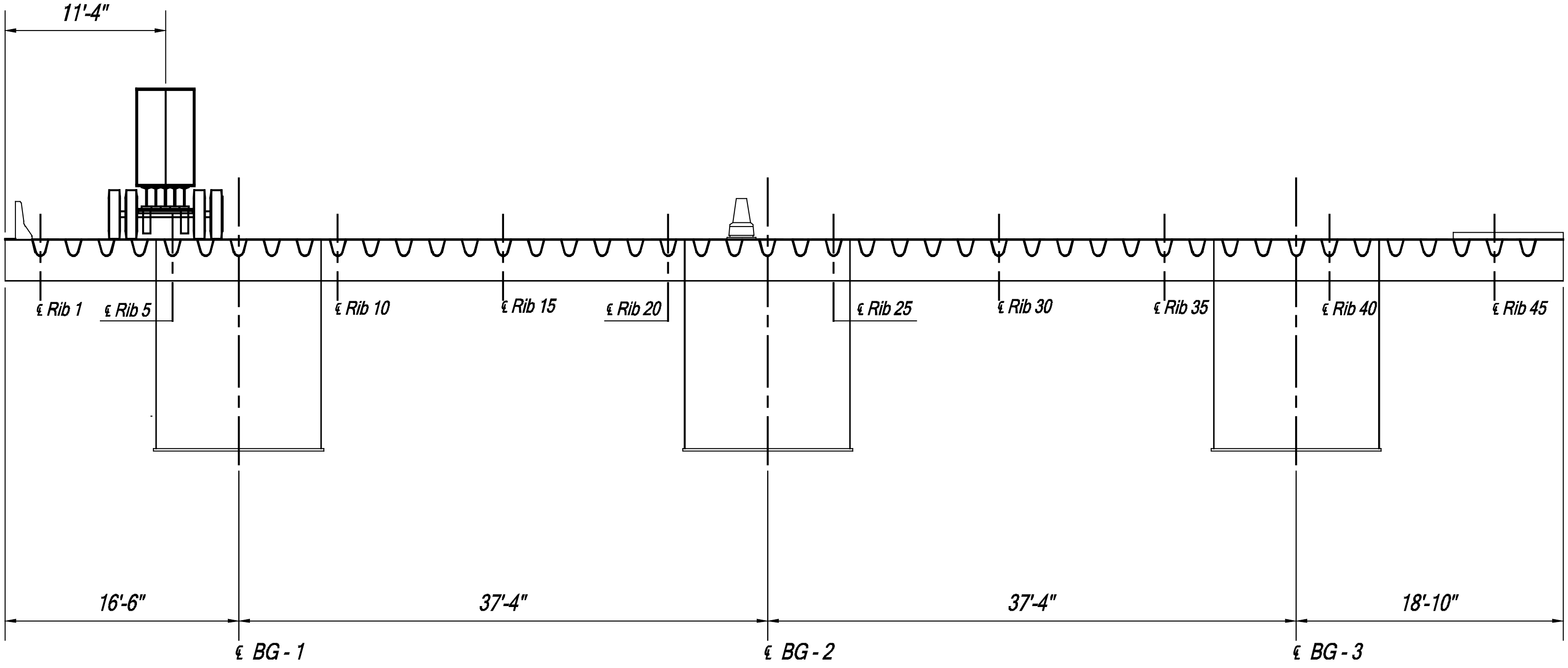

Figure 10. Transverse load position T1 considered for FEA of bridge deck

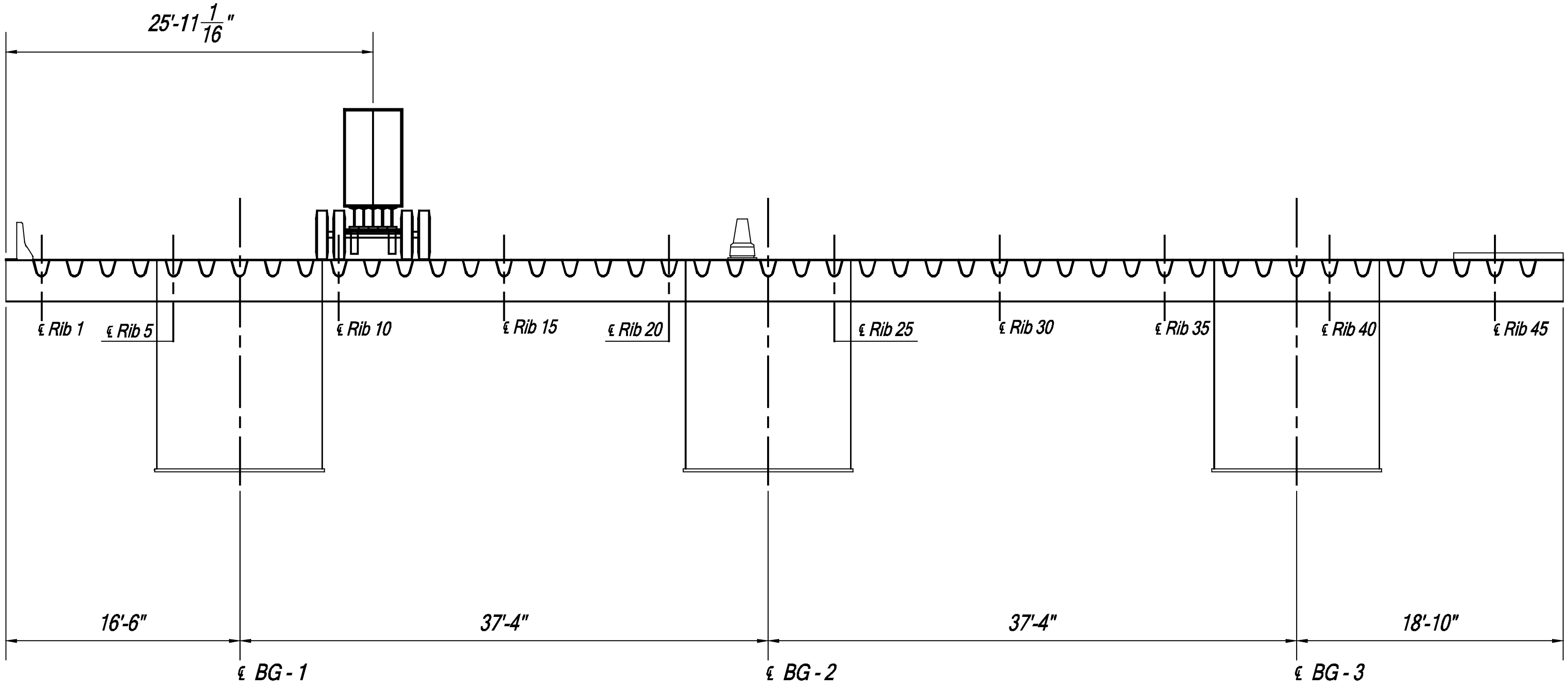

Figure 11. Transverse load position T26 considered for FEA of bridge deck

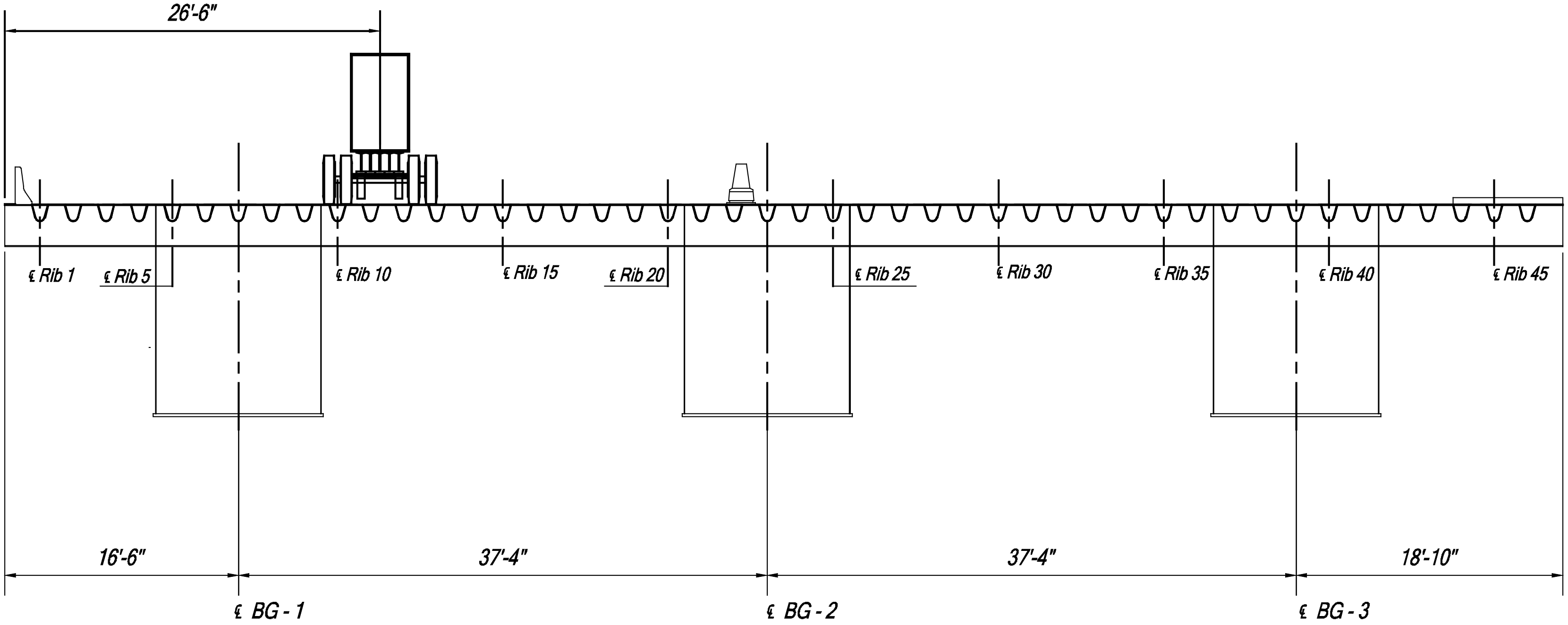

Figure 12. Transverse load position T27 considered for FEA of bridge deck

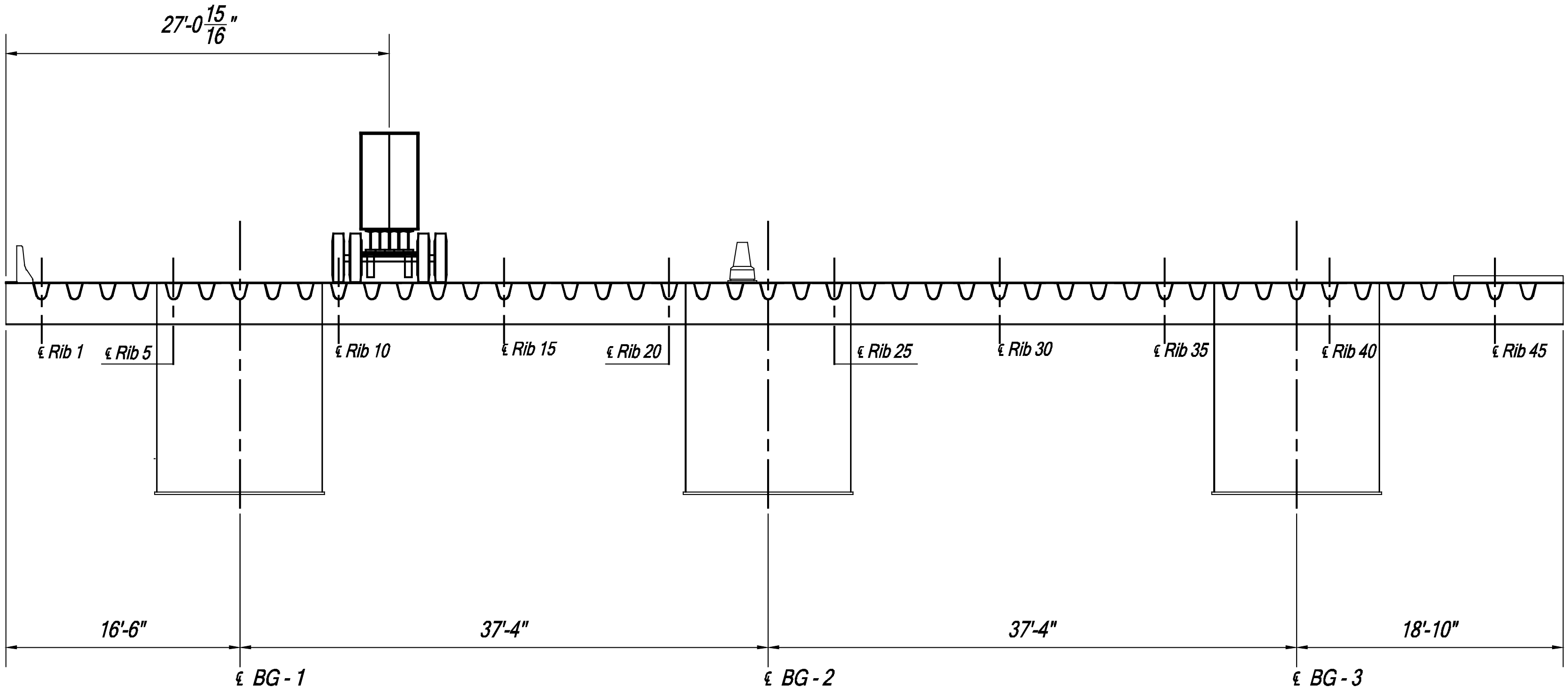

Figure 13. Transverse load position 28 considered for FEA of bridge deck

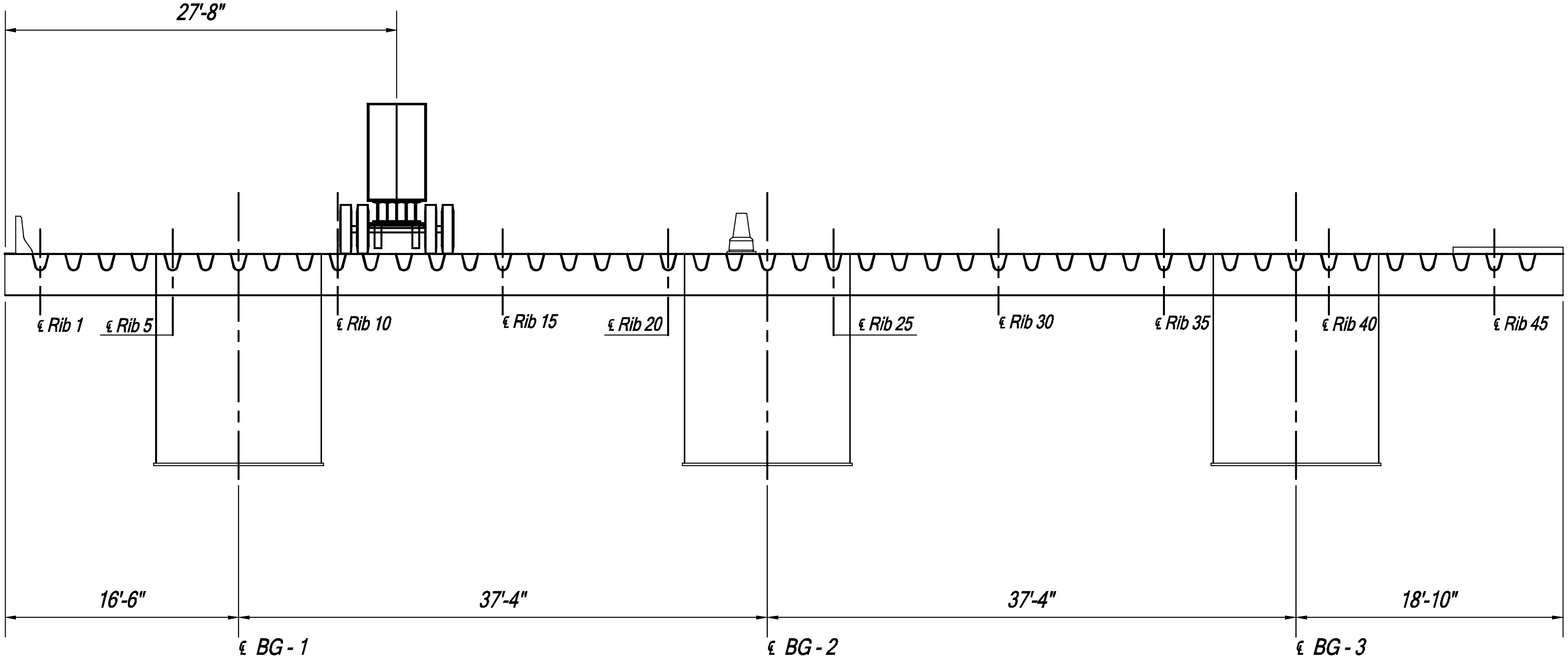

Figure 14. Transverse load position 29 considered for FEA of bridge deck

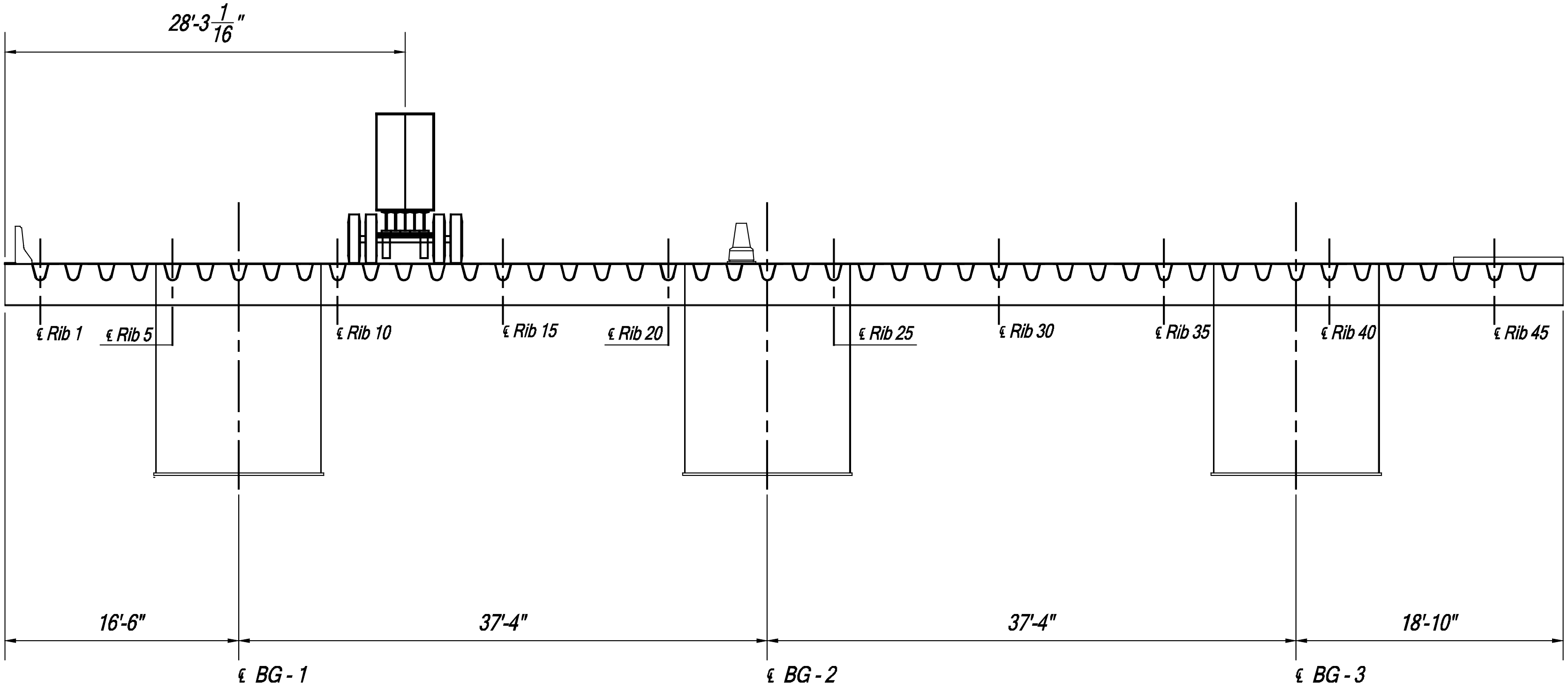

Figure 15. Transverse load position 30 considered for FEA of bridge deck

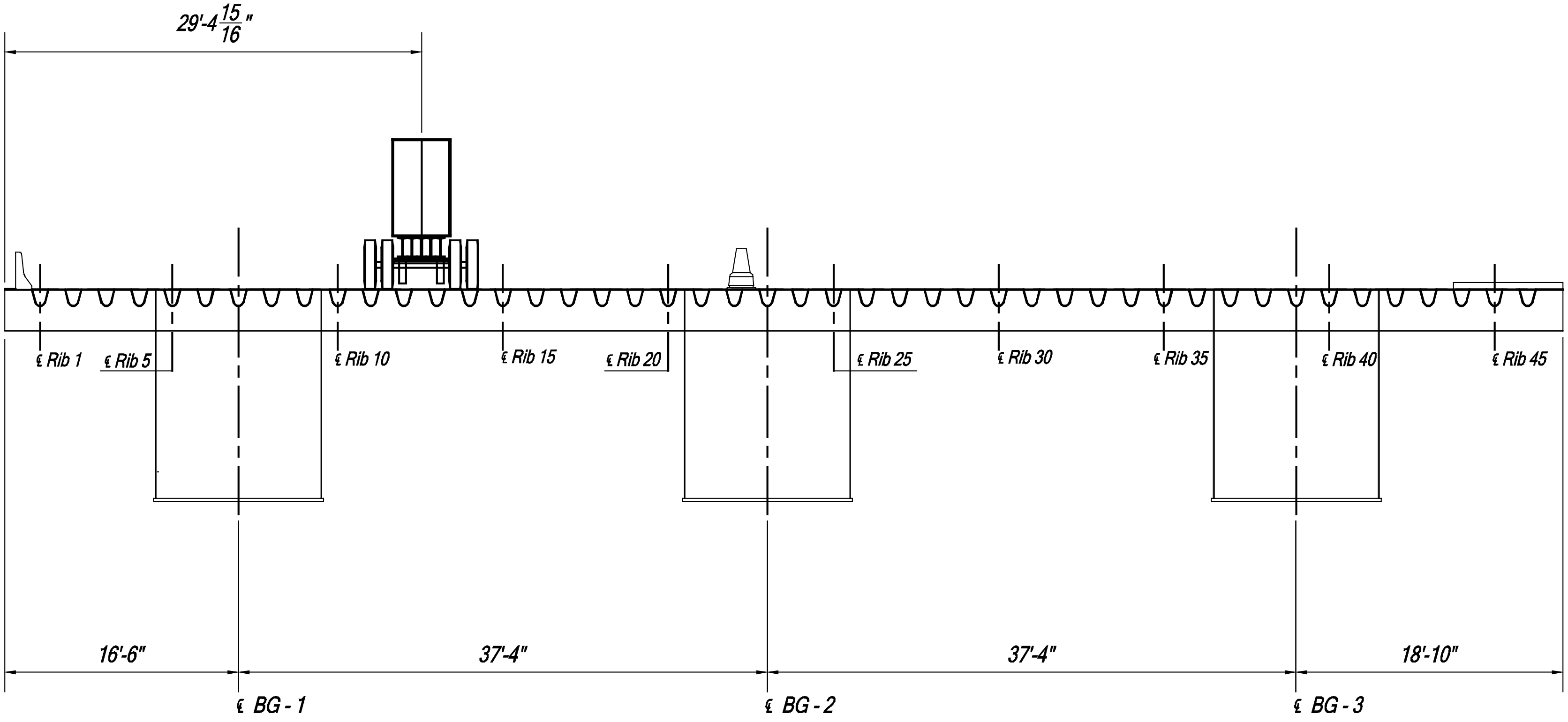

Figure 16. Transverse load position 33 considered for FEA of bridge deck

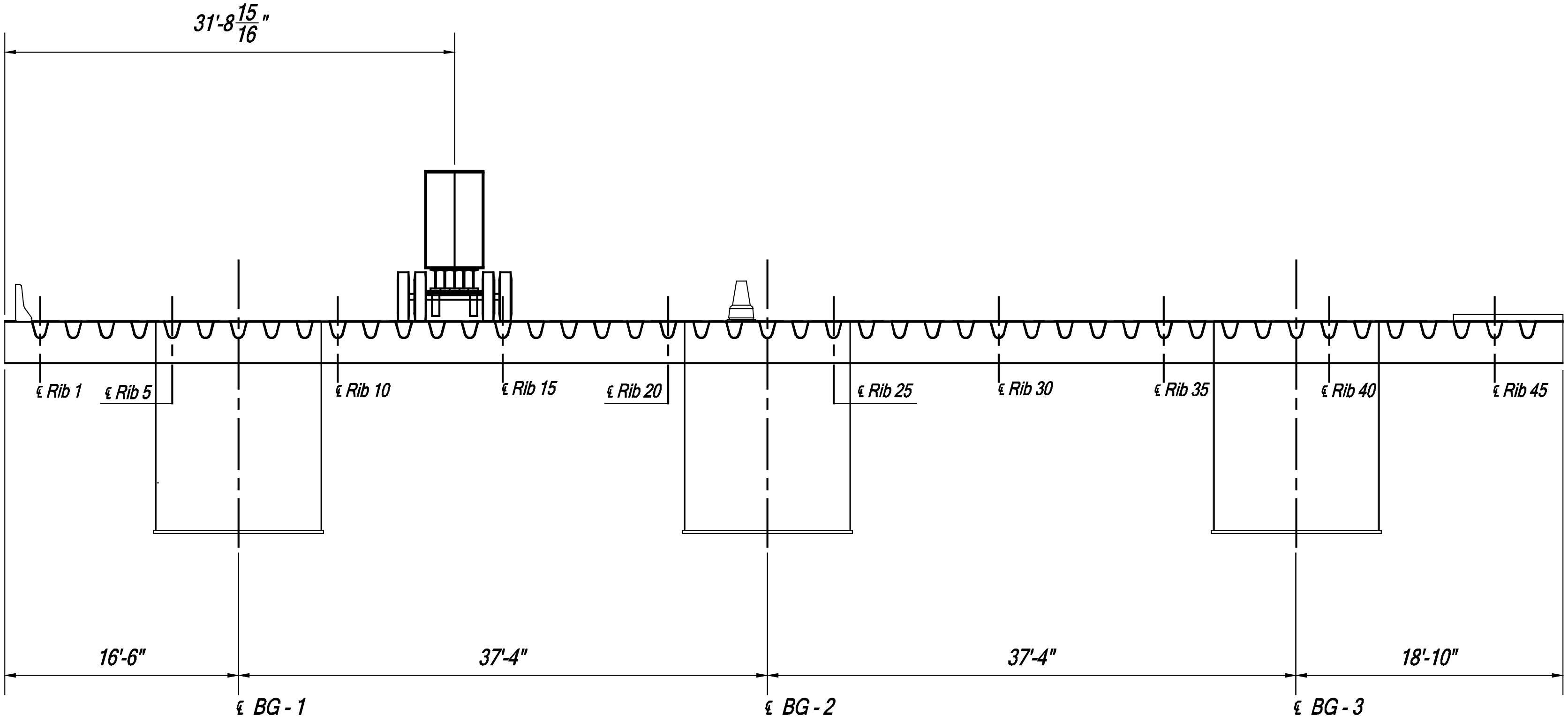

Figure 17. Transverse load position 34 considered for FEA of bridge deck

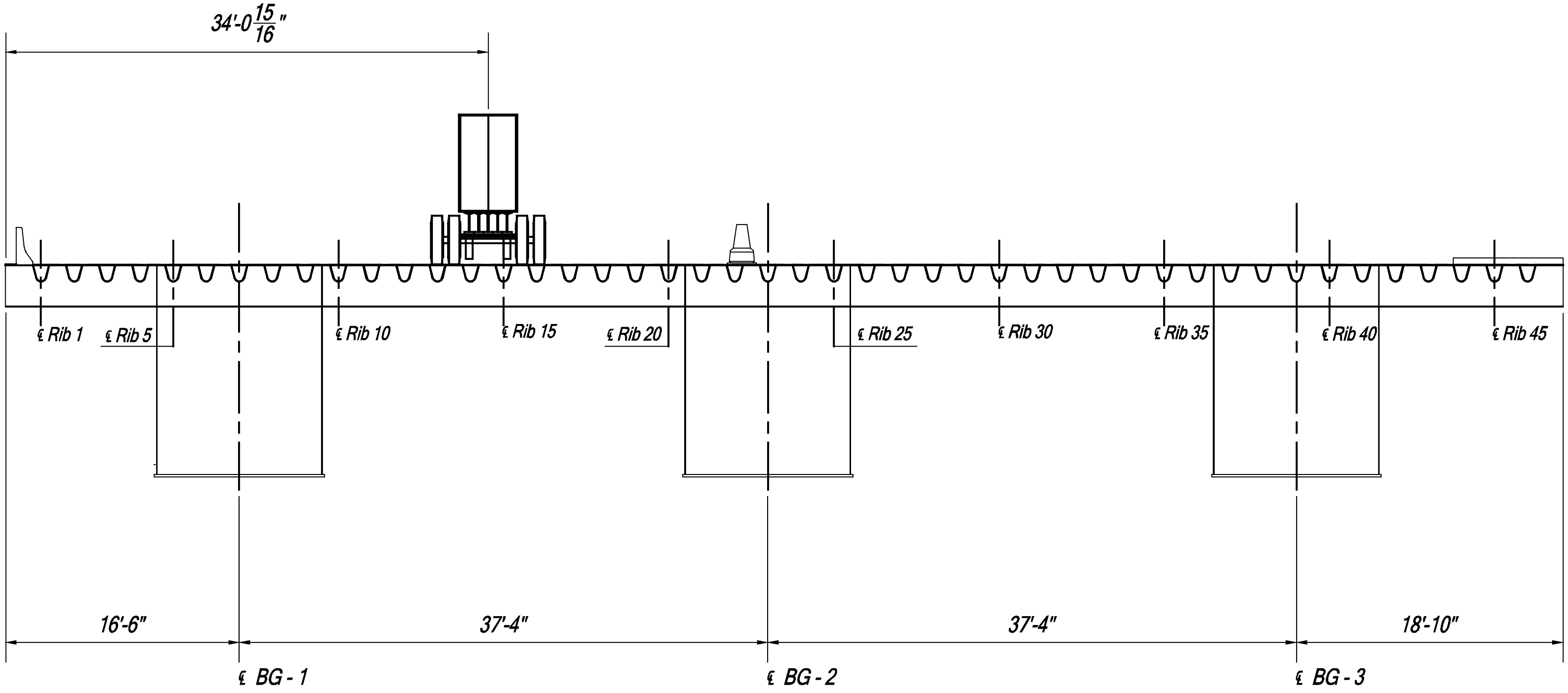

Figure 18. Transverse load position 35 considered for FEA of bridge deck

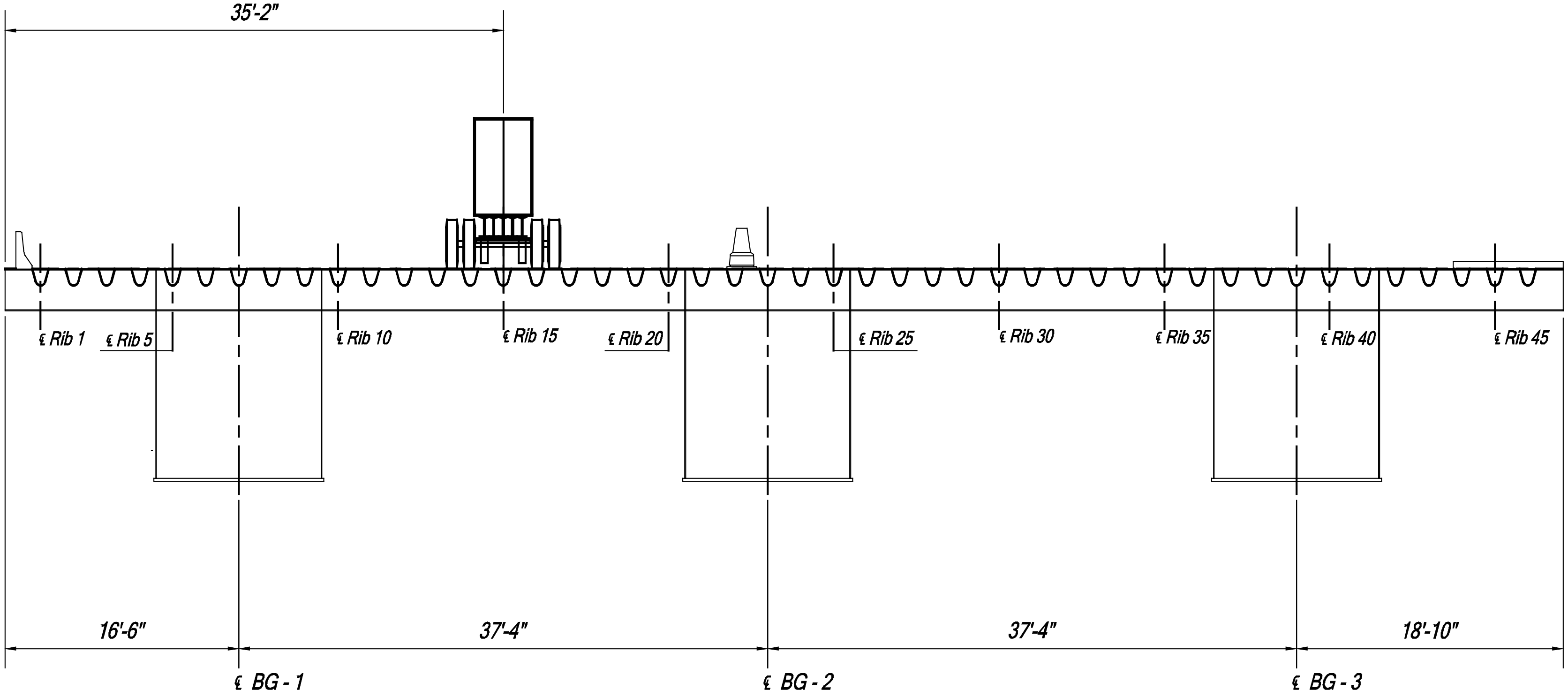

Figure 19. Transverse load position 36 considered for FEA of bridge deck

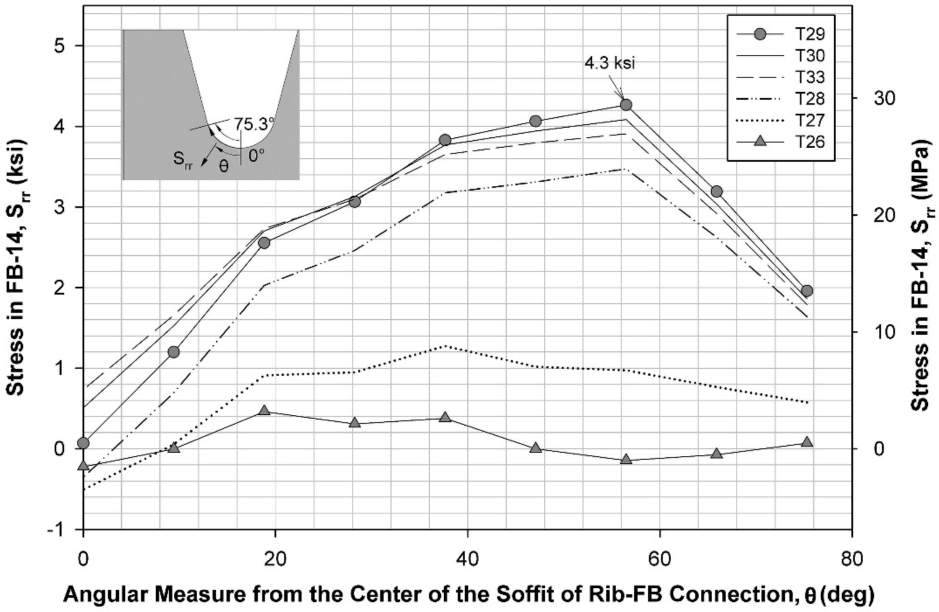

Figure 20. Comparison of tensile stress normal to weld toe in floor beam web for different transverse load cases corresponding to L1

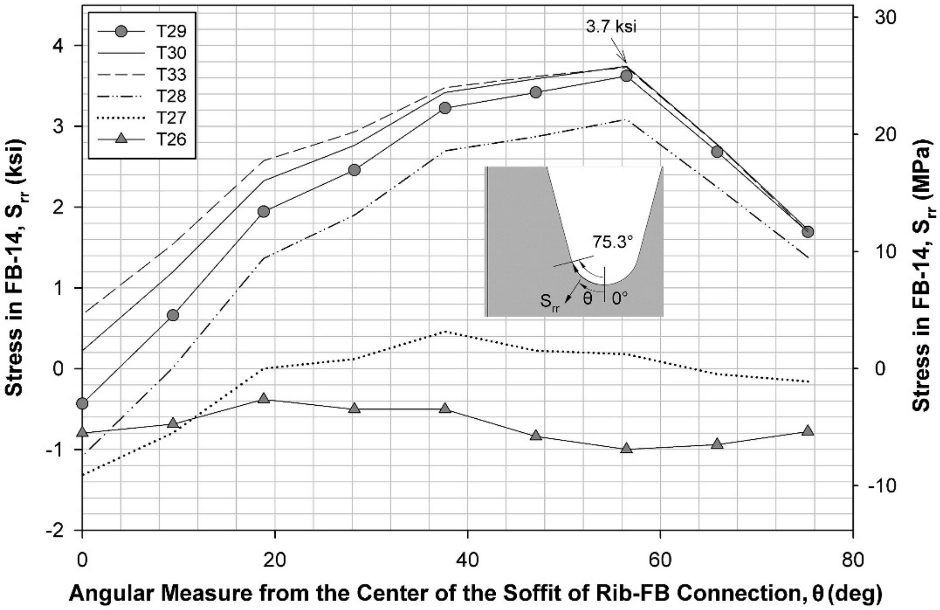

Figure 21. Comparison of tensile stress normal to weld toe in floor beam web for different transverse load cases corresponding to L2

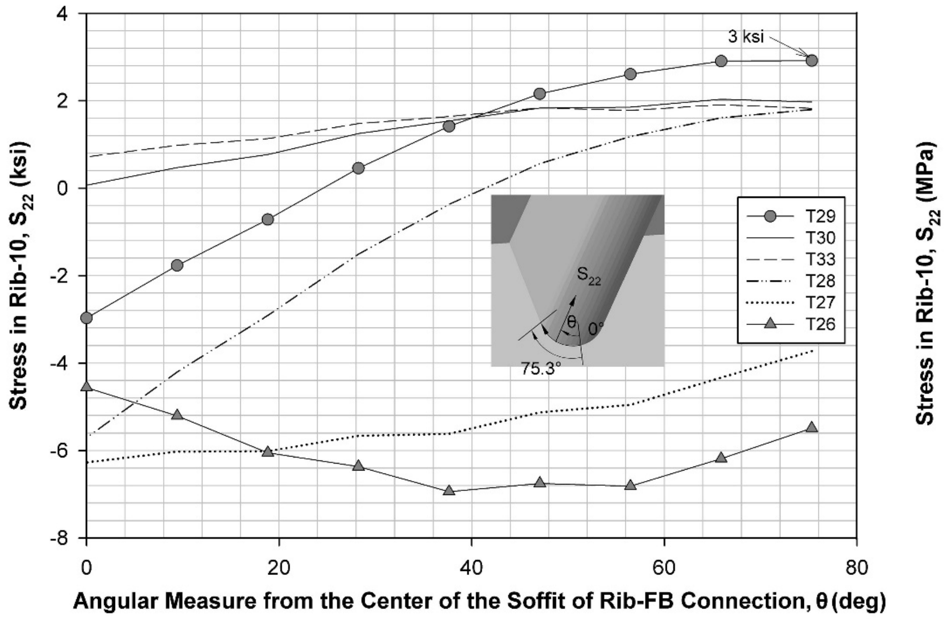

Figure 22. Comparison of tensile stress normal to weld toe in rib wall for different transverse load cases corresponding to L1

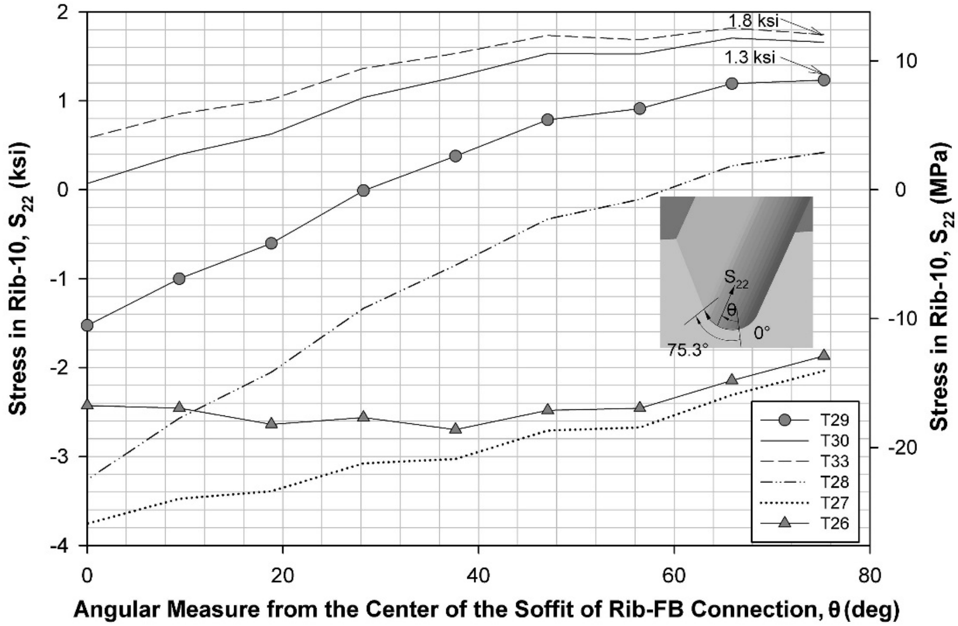

Figure 23. Comparison of tensile stress normal to weld toe in rib wall for different transverse load cases corresponding to L2

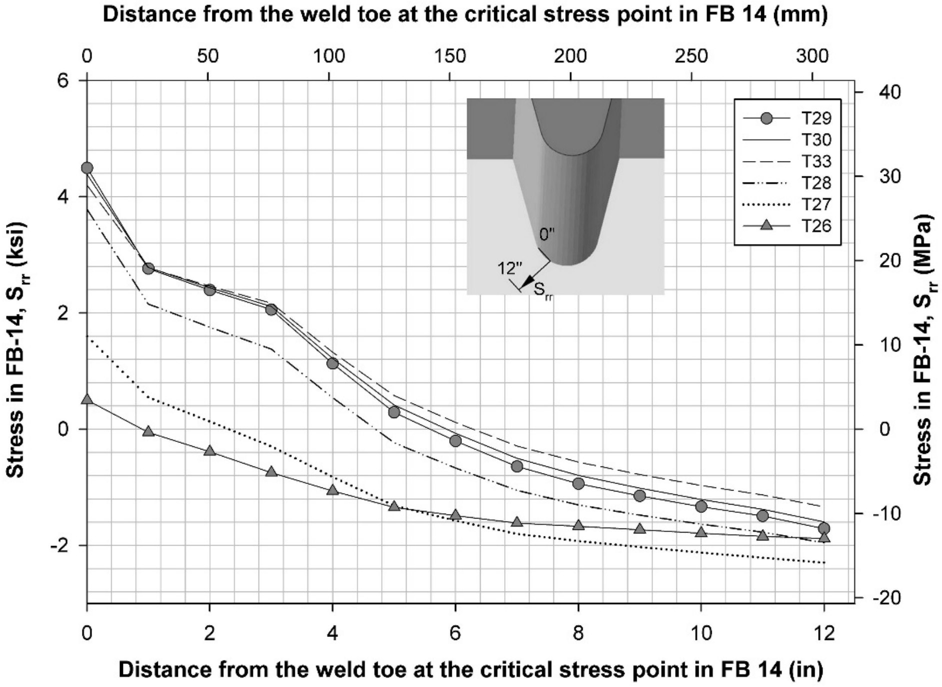

Figure 24. Variation of tensile stress normal to weld toe in floor beam web along a radial path starting from the point of maximum tensile stress for L1

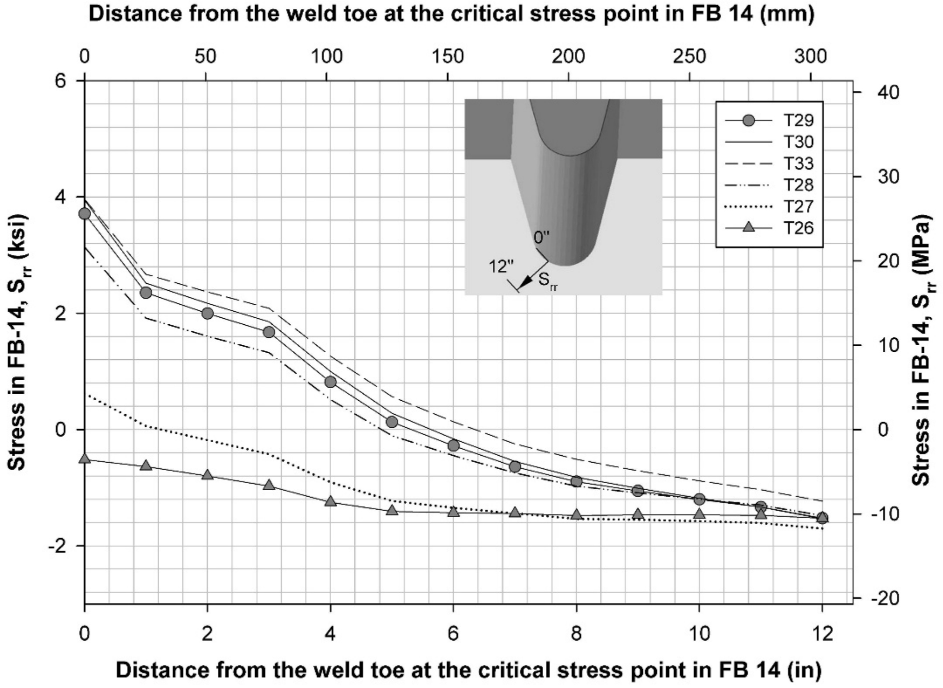

Figure 25. Variation of tensile stress normal to weld toe in floor beam web along a radial path starting from the point of maximum tensile stress for L1

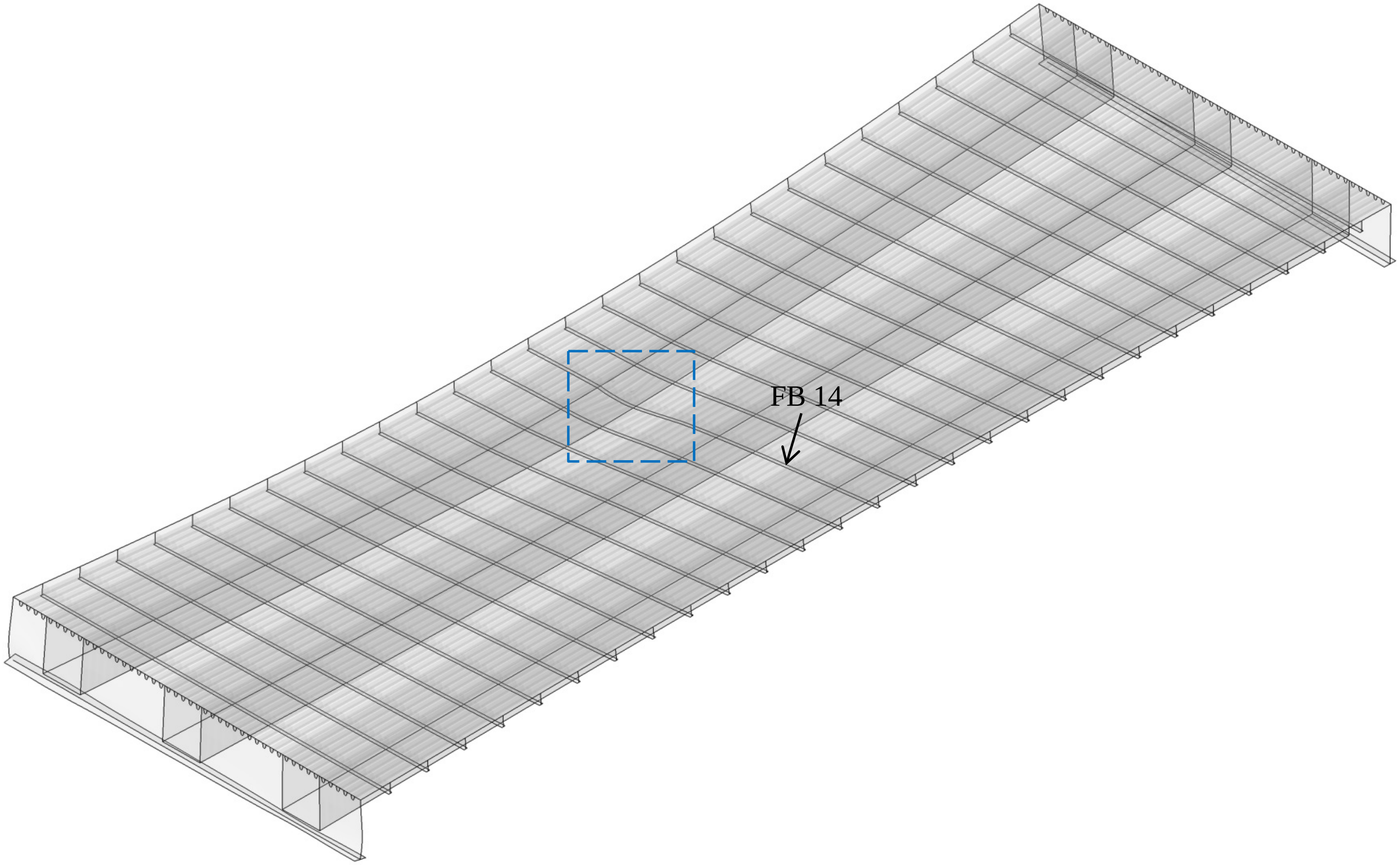

Figure 26. 3D view of the deflected shape of the bridge deck under load case L1T29 (300x)

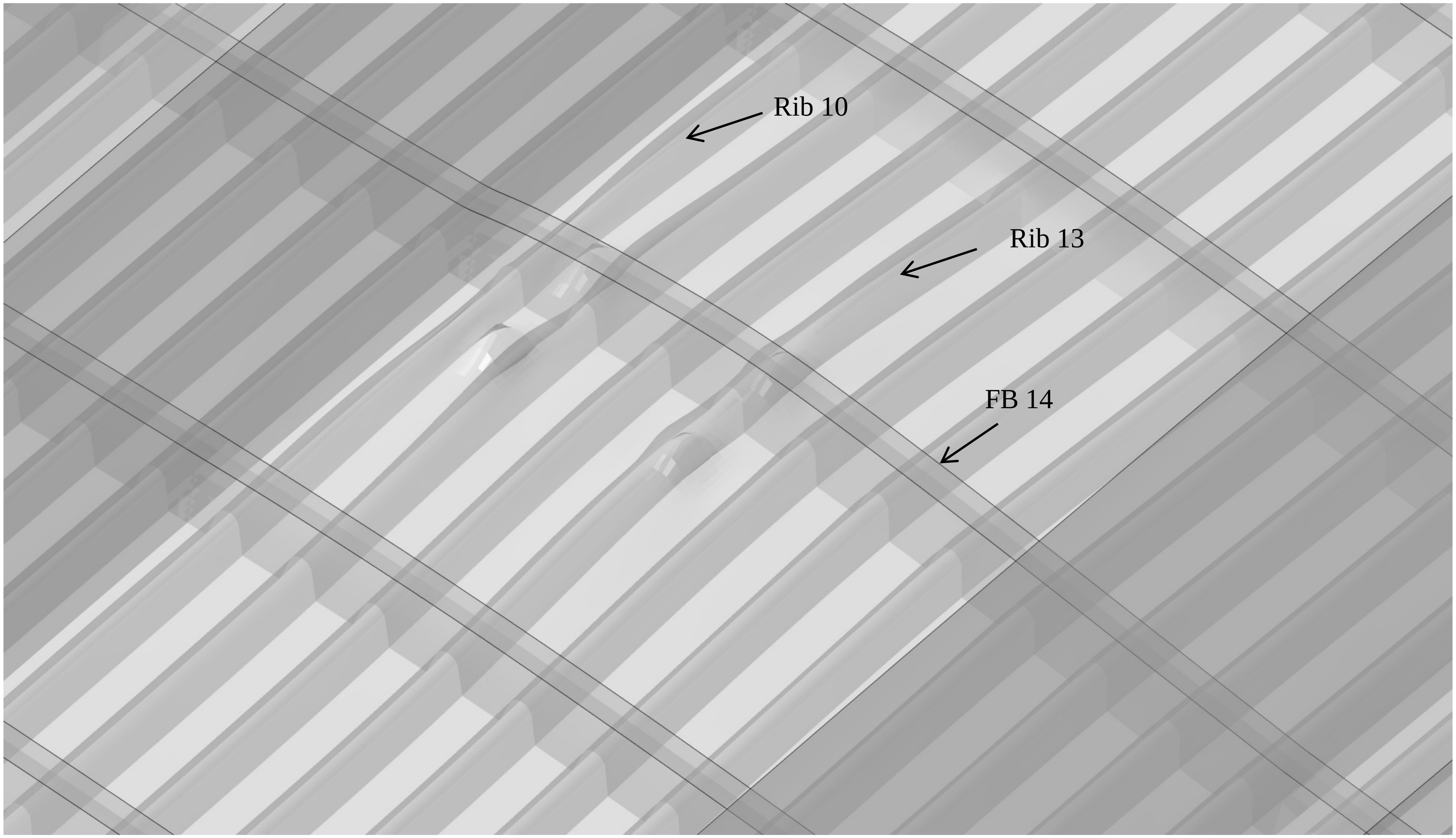

Figure 27. Underside zoomed view of the selected portion in Figure 26

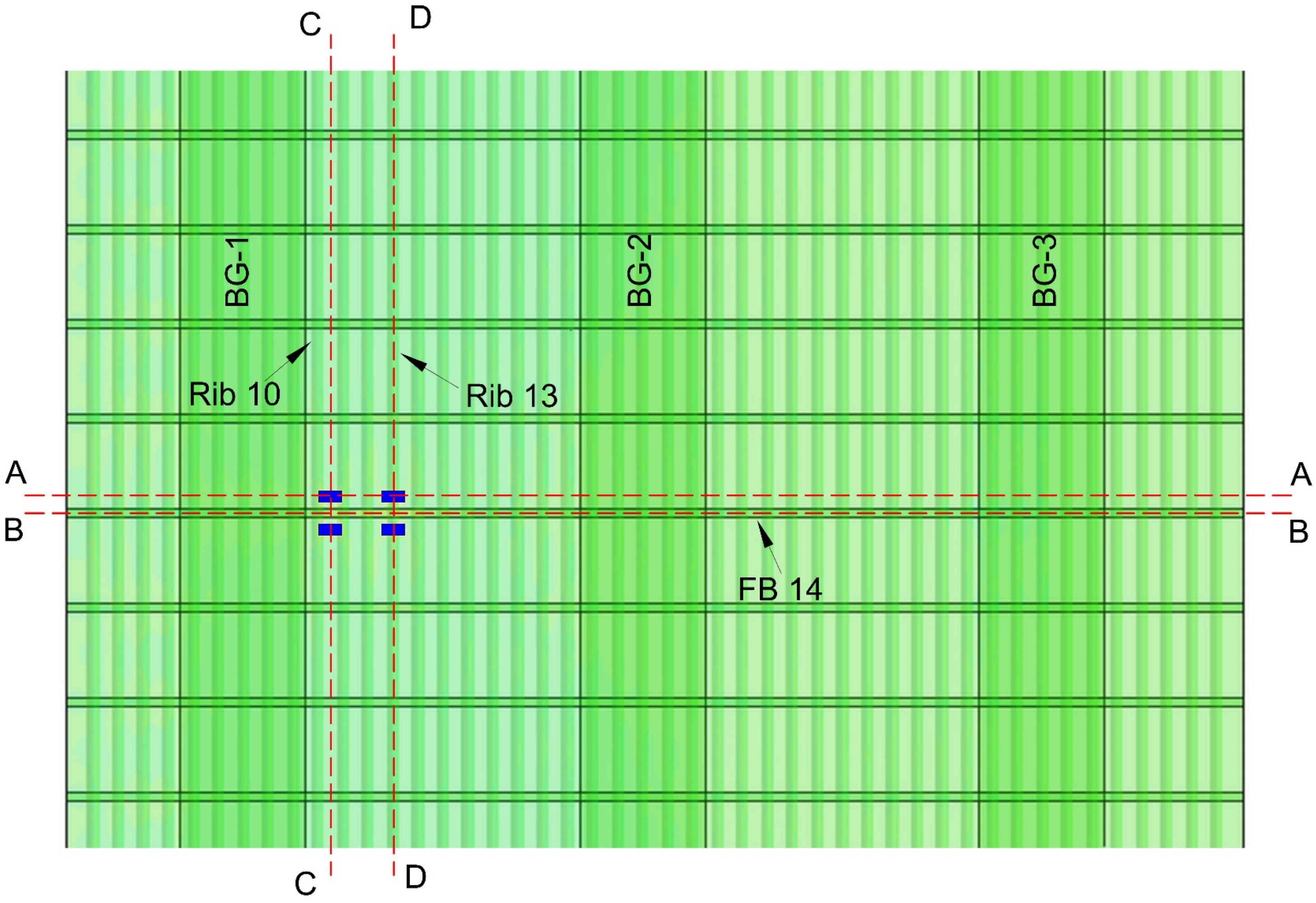

Figure 28. Plan view of the global model showing the sections at which response of deck plate and ribs are discussed

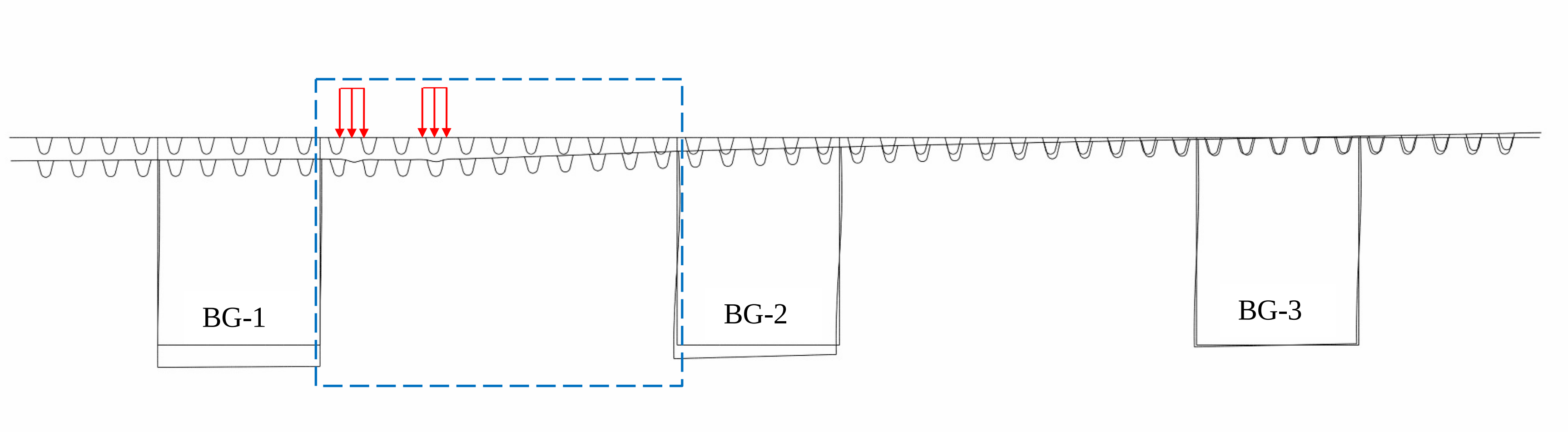

Figure 29. Overlay plot showing the deflected shape of the bridge deck at the section A-A under load case L1T29 (50x)

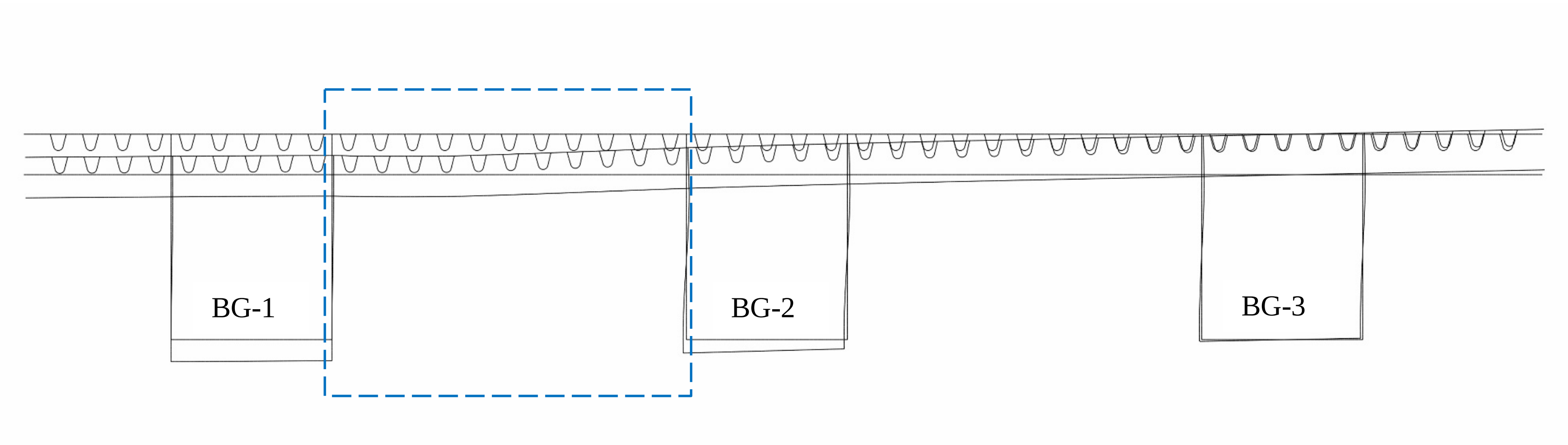

Figure 30. Overlay plot showing the deflected shape of the bridge deck at the section B-B under load case L1T29 (50x)

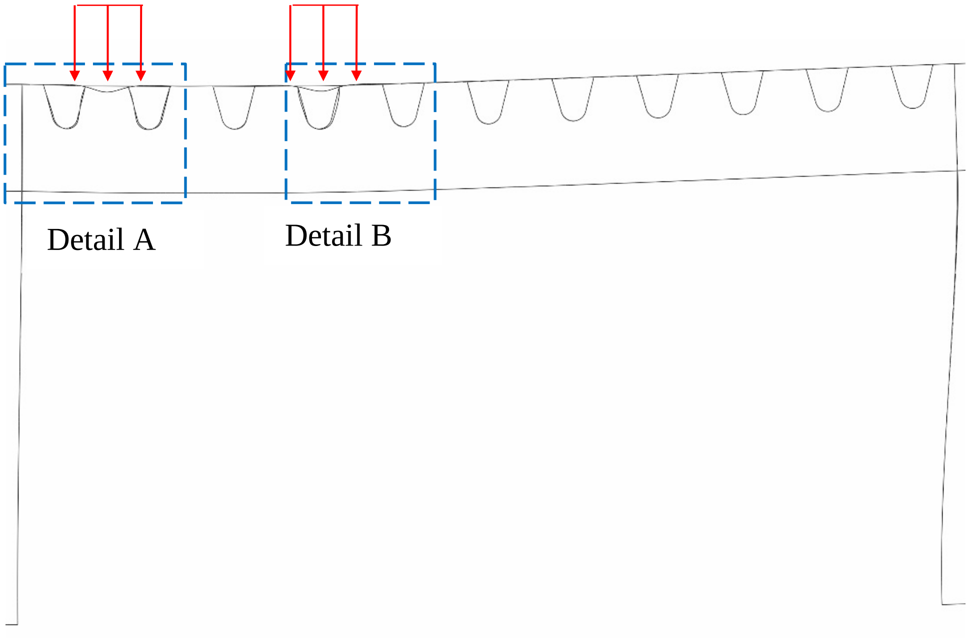

Figure 31. Overlay plot of deck comparing local transverse bending at sections A-A and B-B (50x)

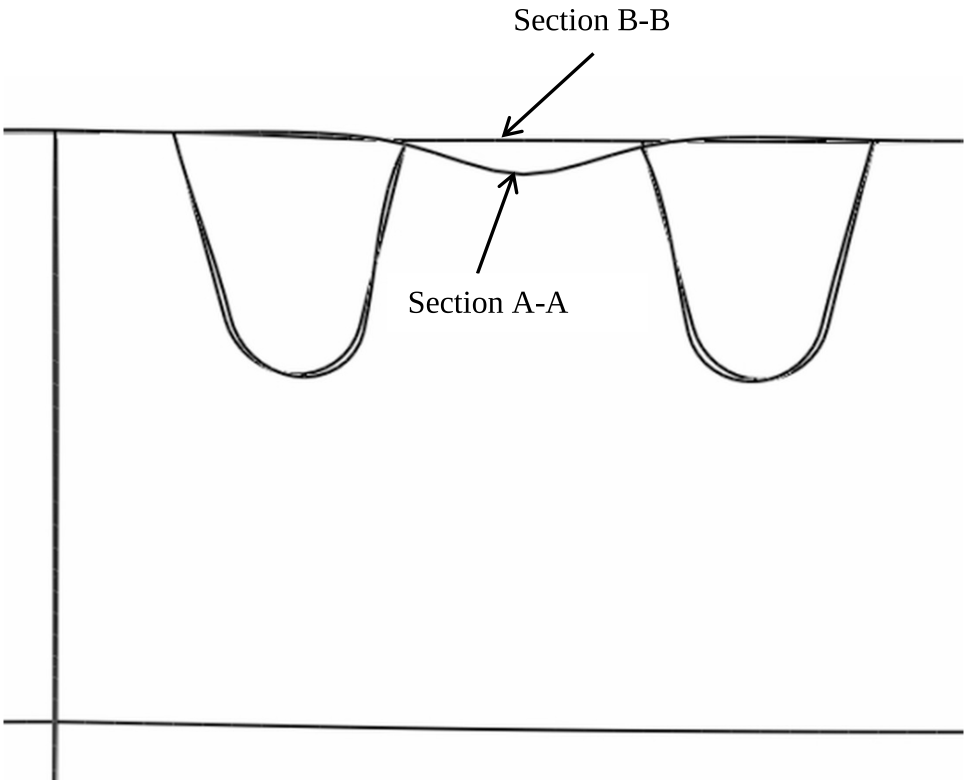

Figure 32. Detail of Figure 31

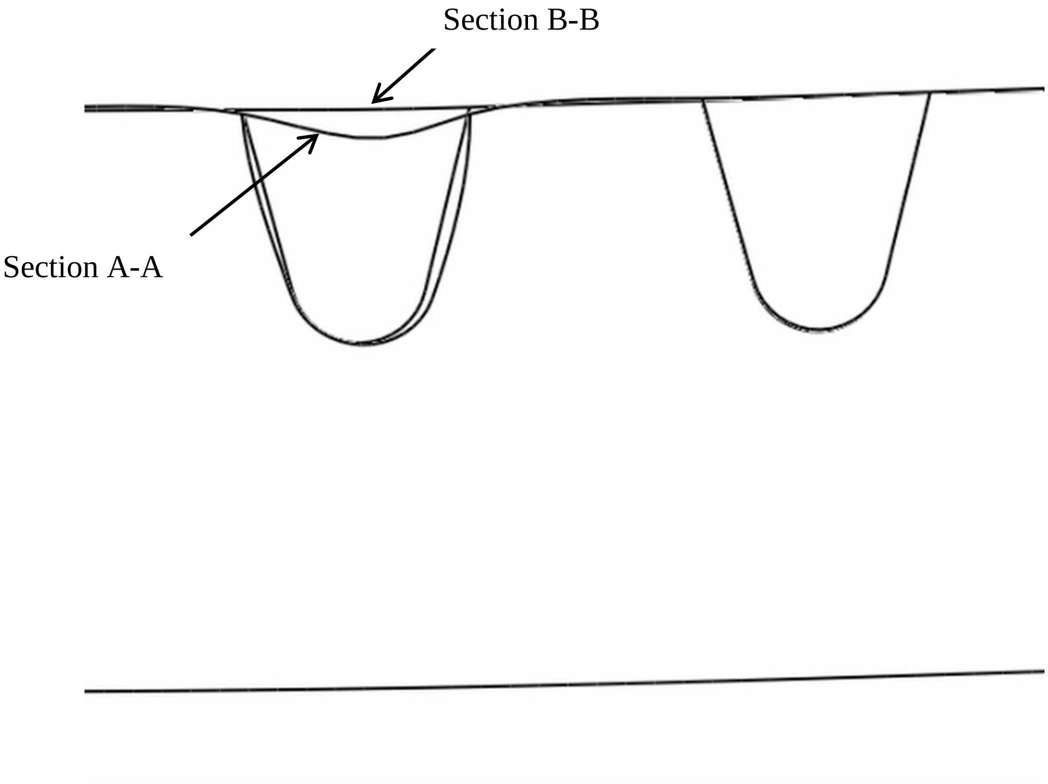

Figure 33. Detail B of Figure 31

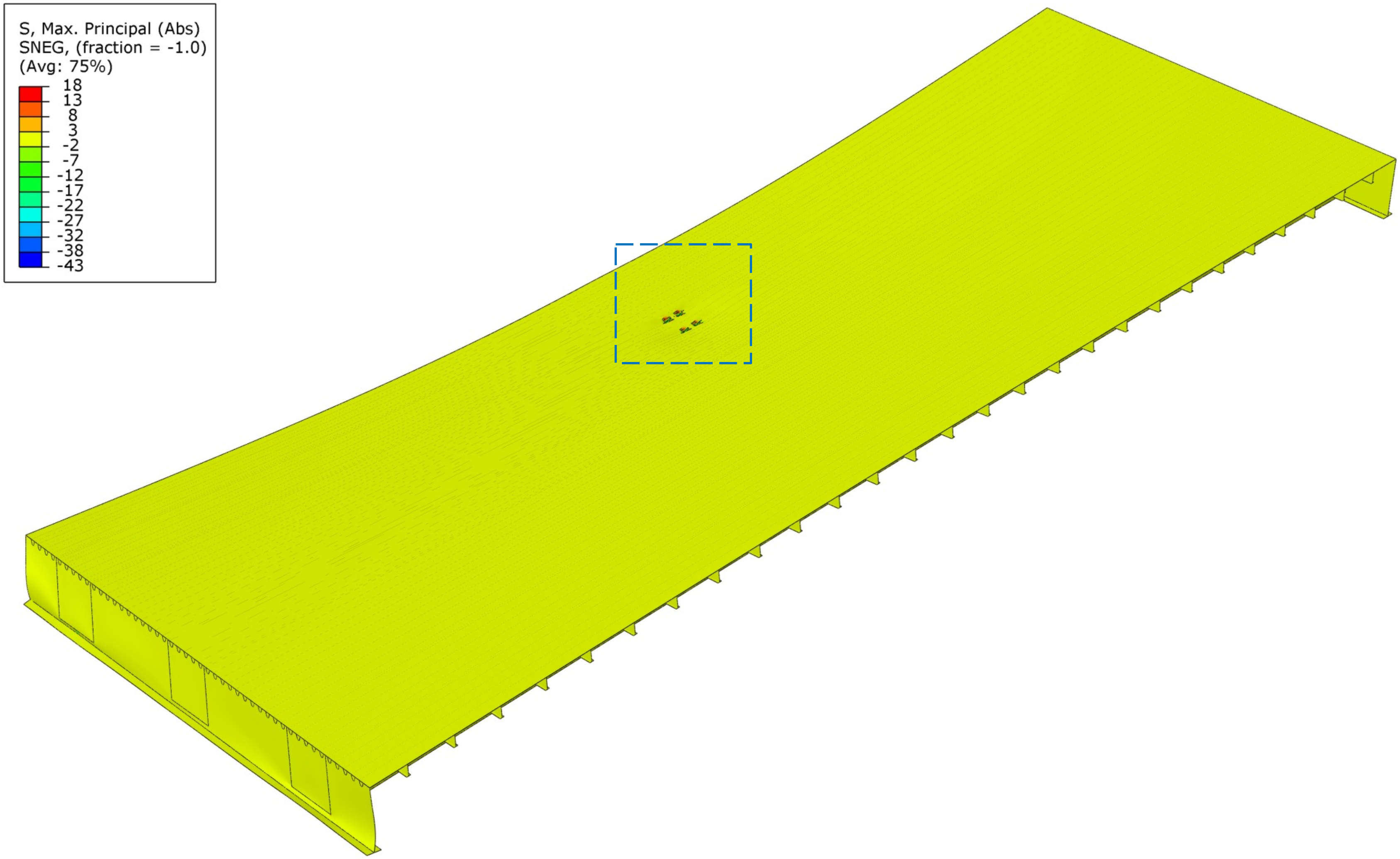

Figure 34. Principal stress contour of the bridge deck showing deck plate stresses

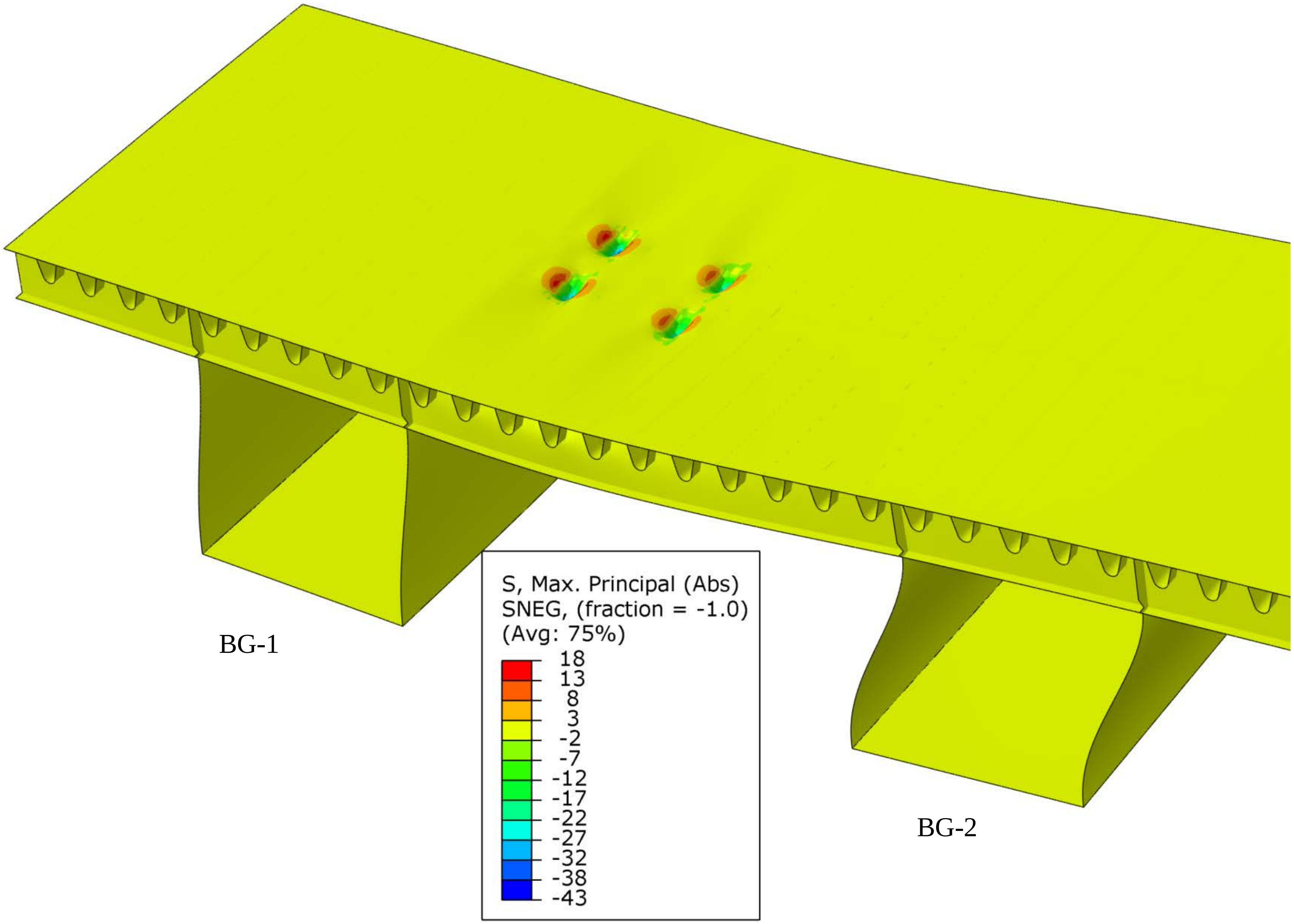

Figure 35. Principal stress contour of the portion of the deck around the load patches (300x) showing deck plate stresses

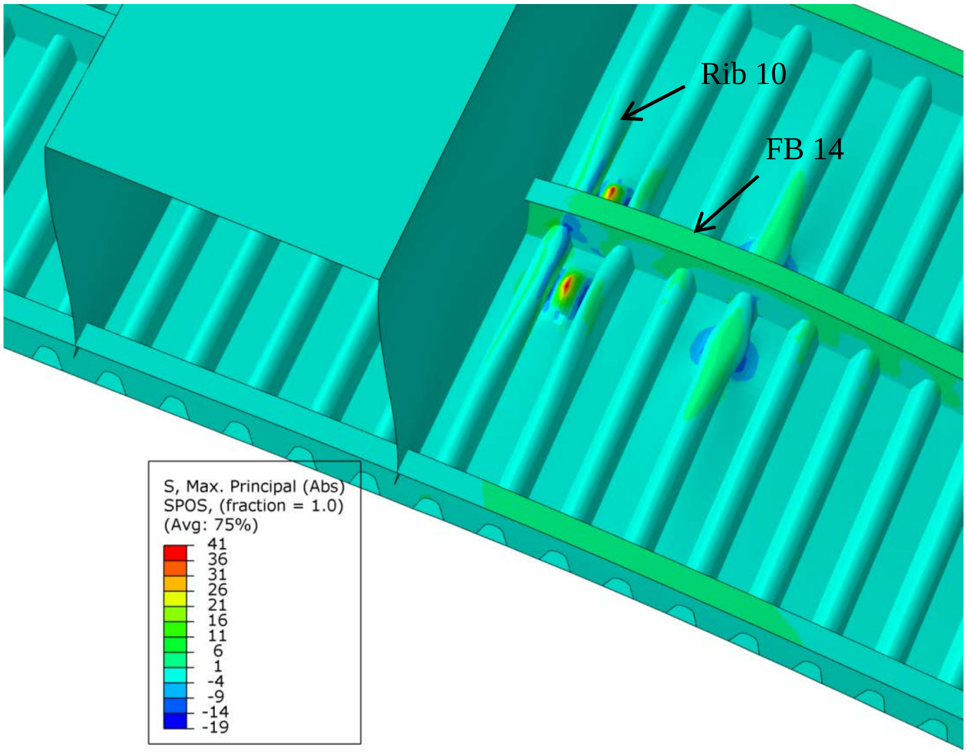

Figure 36. Underside view of the principal stress contour of the portion of the deck around the load patches showing deck plate stresses (300x)

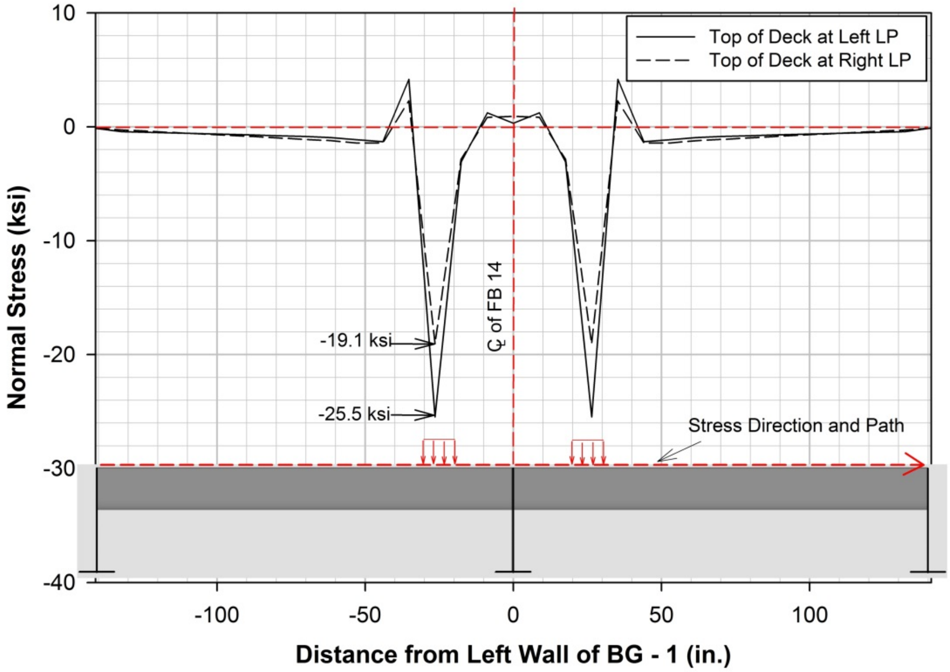

Figure 37. Distribution of longitudinal direction stress at the top of deck plate along sections C-C and D-D for load case L1T29

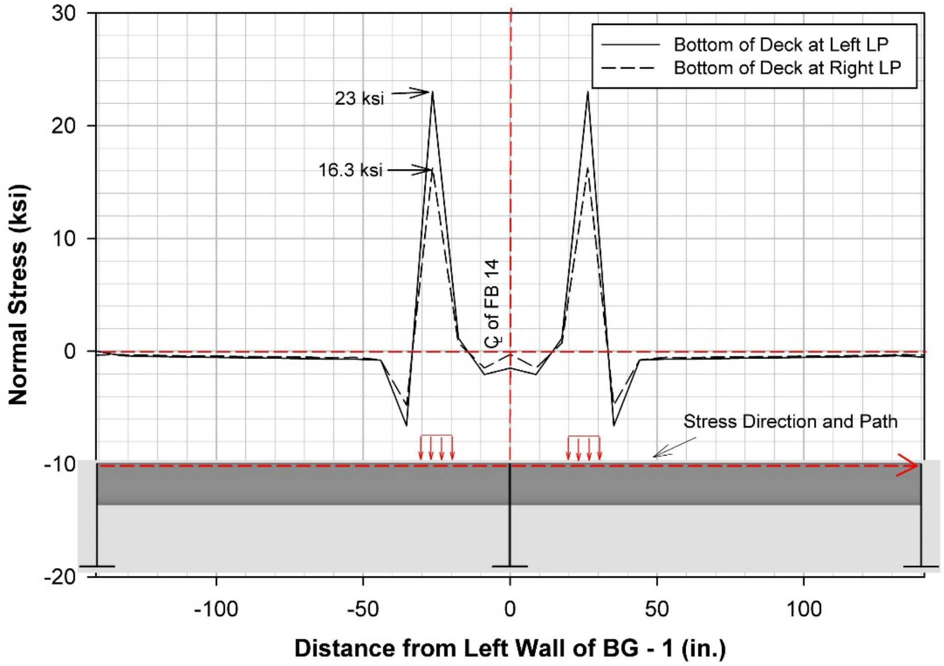

Figure 38. Distribution of longitudinal direction stress at the bottom of deck plate along sections C-C and D-D for load case L1T29

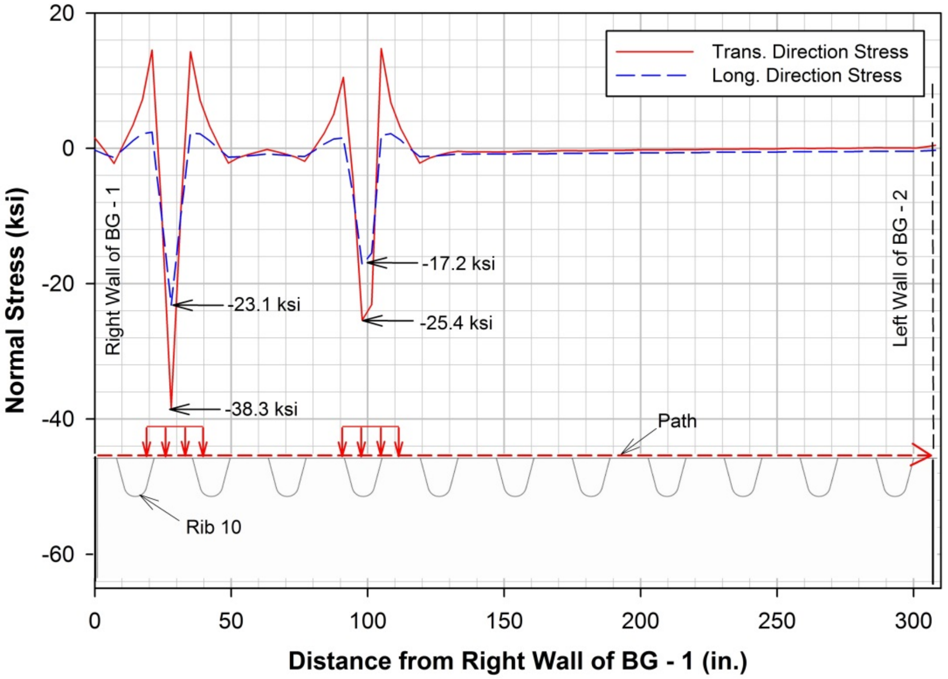

Figure 39. Comparison of longitudinal and transverse stresses at top of deck plate at section A-A for load case L1T29

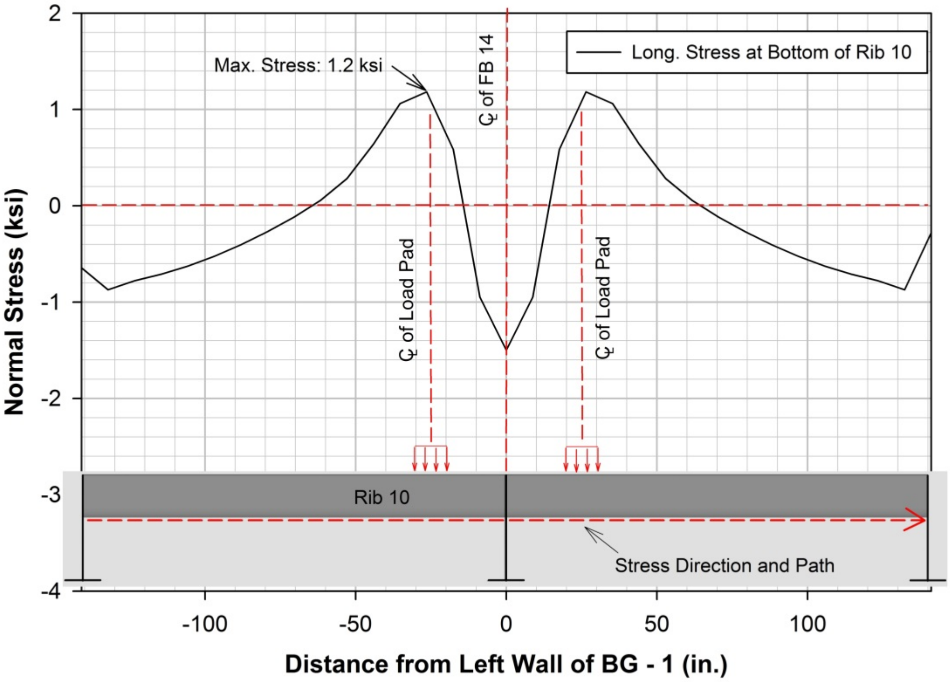

Figure 40. Distribution of longitudinal direction stress at the bottom of Rib 10 for load case L1T29 at a section through the center of the rib

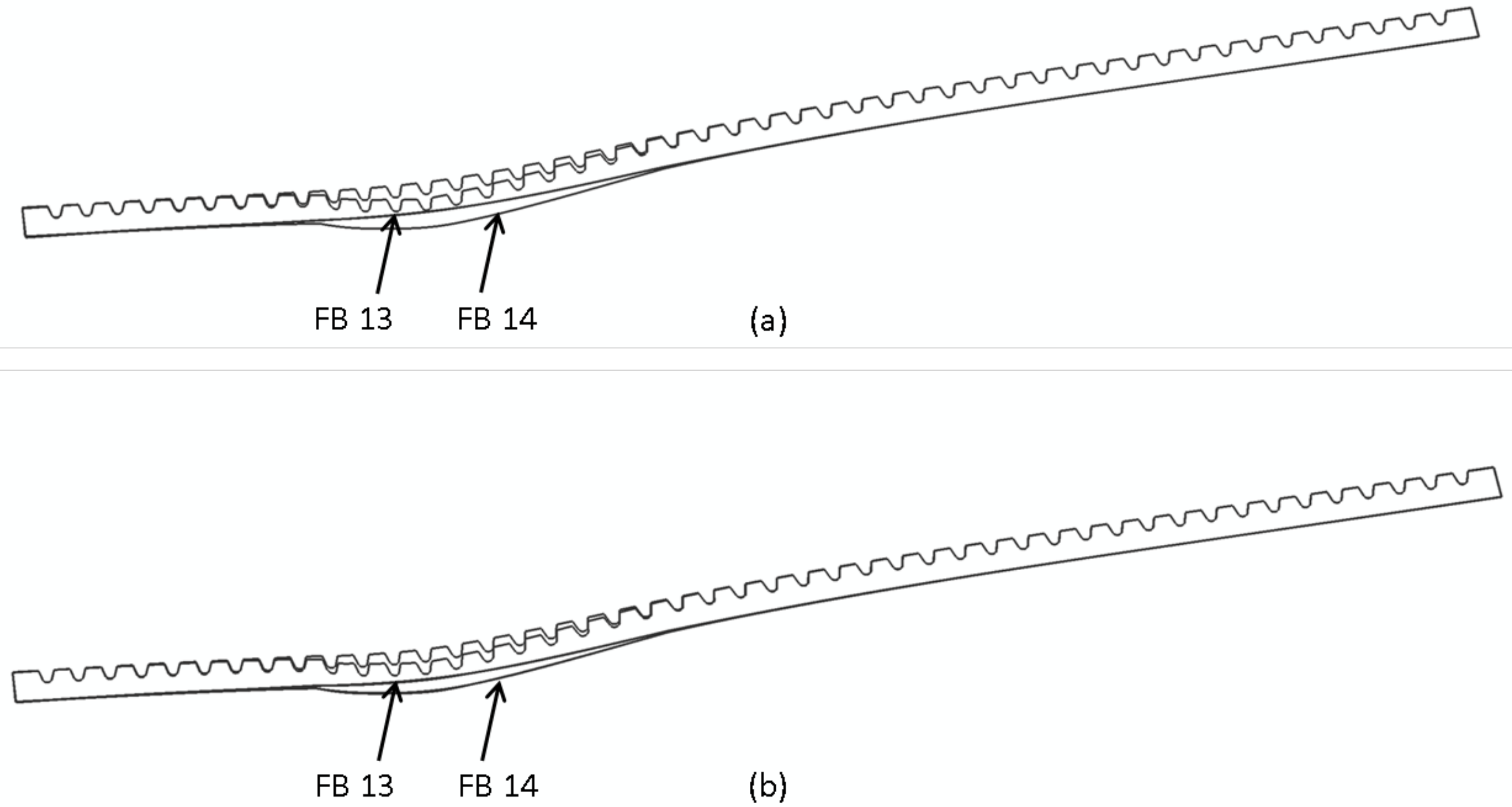

Figure 41. Maximum deformation of FB 13 and FB 14 (500x); (a) Load Case L1T29 (b) Load Case L2T29

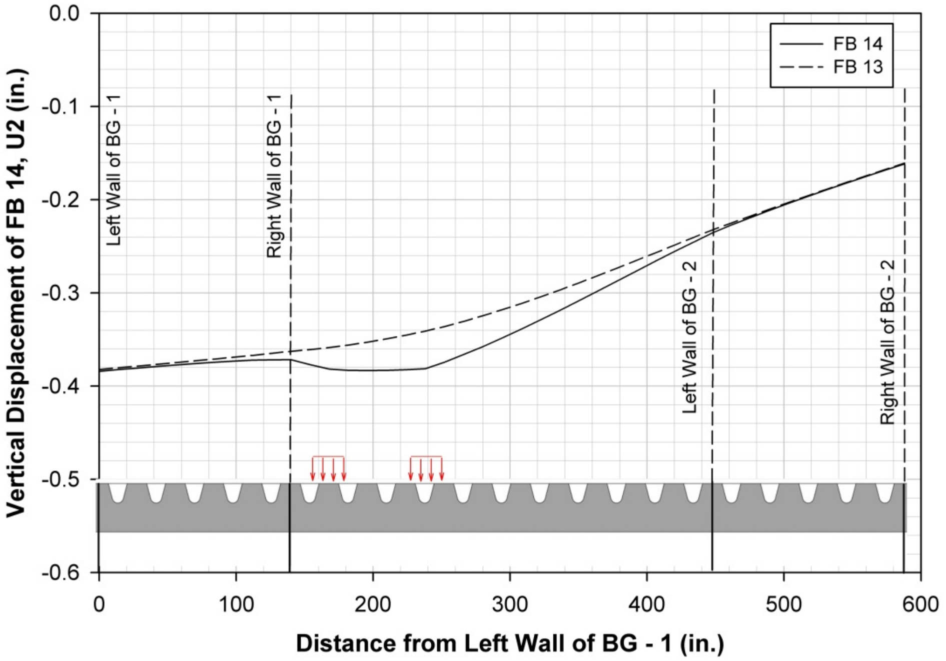

Figure 42. Comparison of vertical displacement of FB 13 and FB 14 for load case L1T29

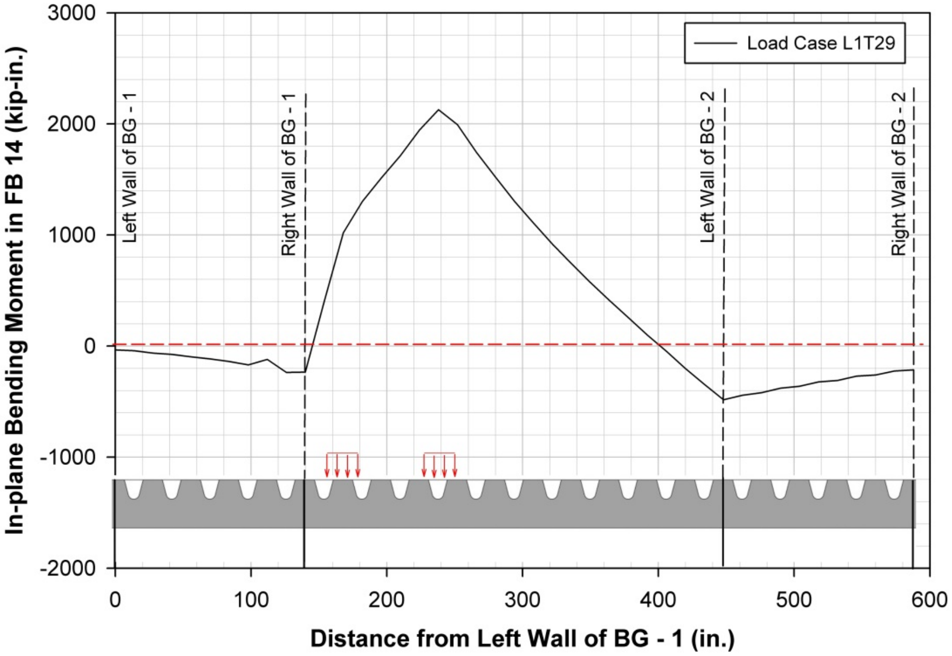

Figure 43. Variation of in-plane bending moment in FB 14 for load case L1T29

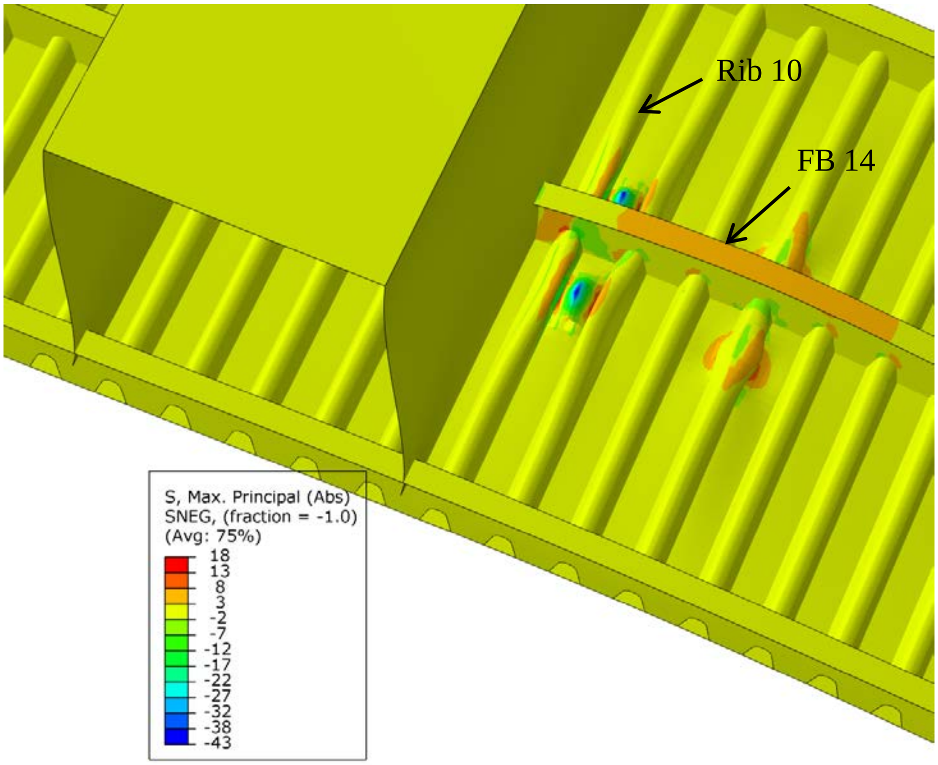

Figure 44. Underside view of the principal stress contour of the portion of the deck around the load patches showing floor stresses (300x)

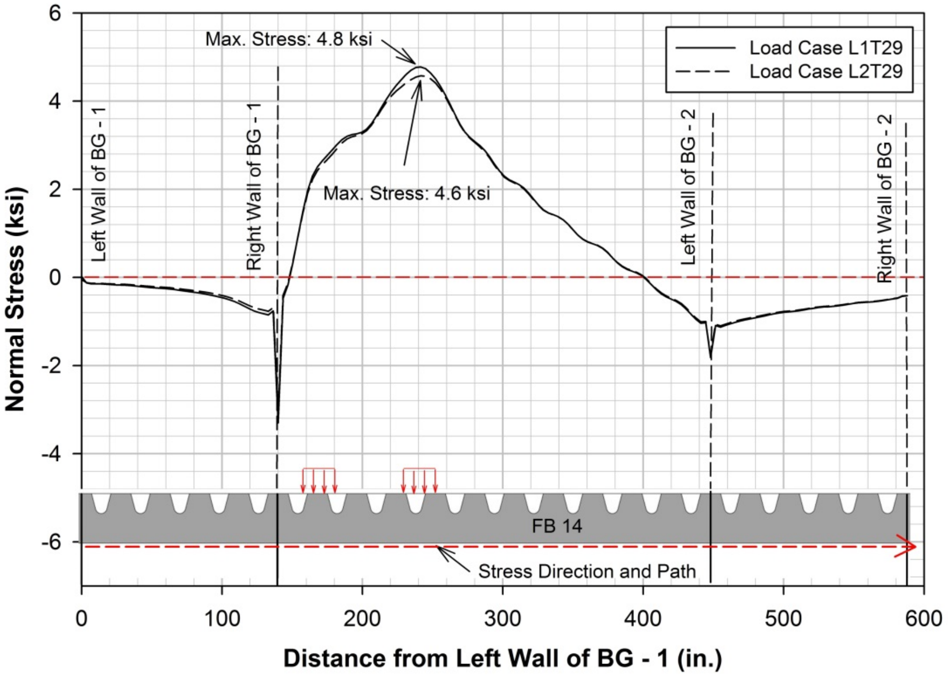

Figure 45. Distribution of transverse direction stress at the bottom of FB 14 for load cases L1T29 and L2T29

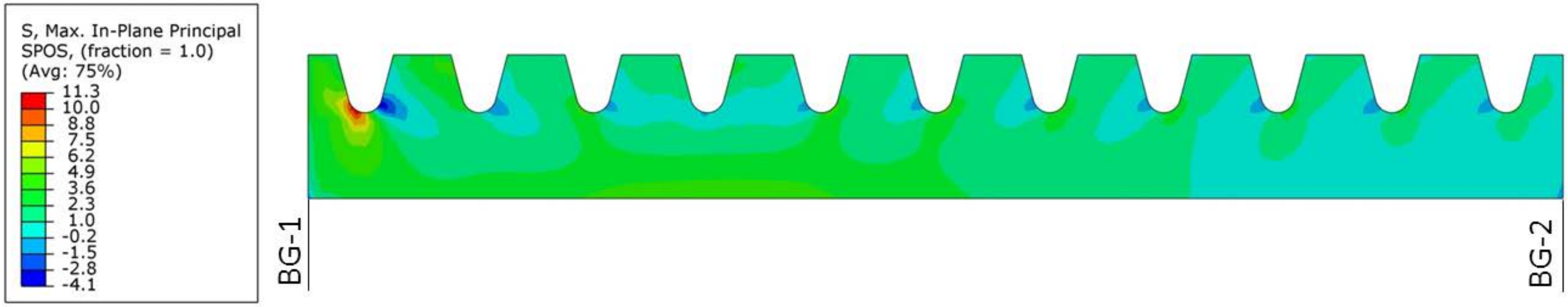

Figure 46. Maximum in-plane principal stress in FB 14 (between BG-1 and BG-2) for L1T29

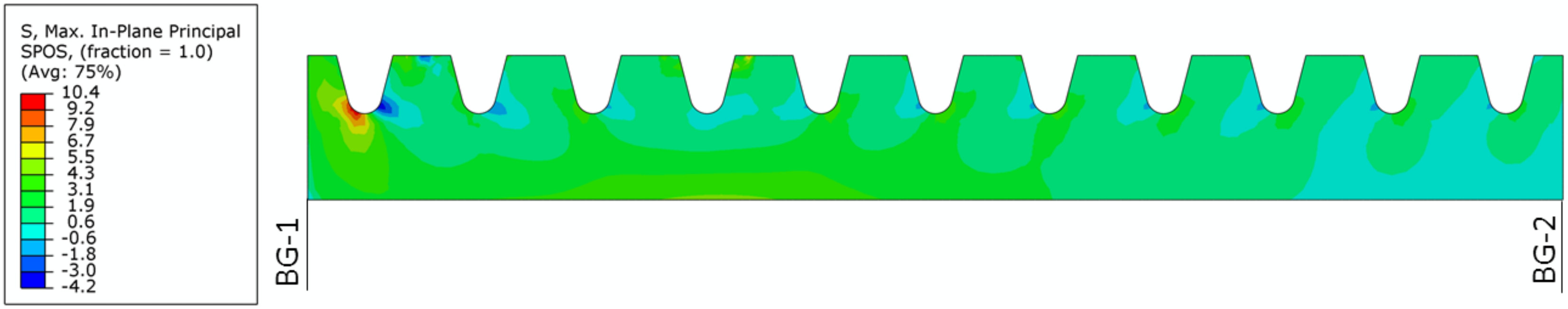

Figure 47. Maximum in-plane principal stress in FB 14 (between BG-1 and BG-2) for L2T29

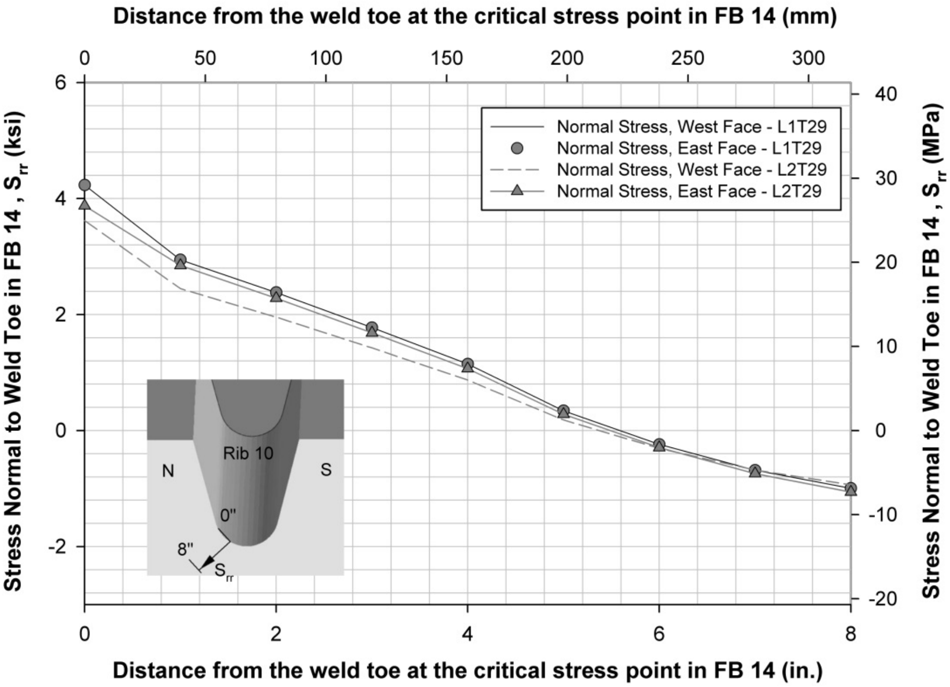

Figure 48. Comparison of normal stresses on the east and west faces of FB 14 showing out-of-plane bending

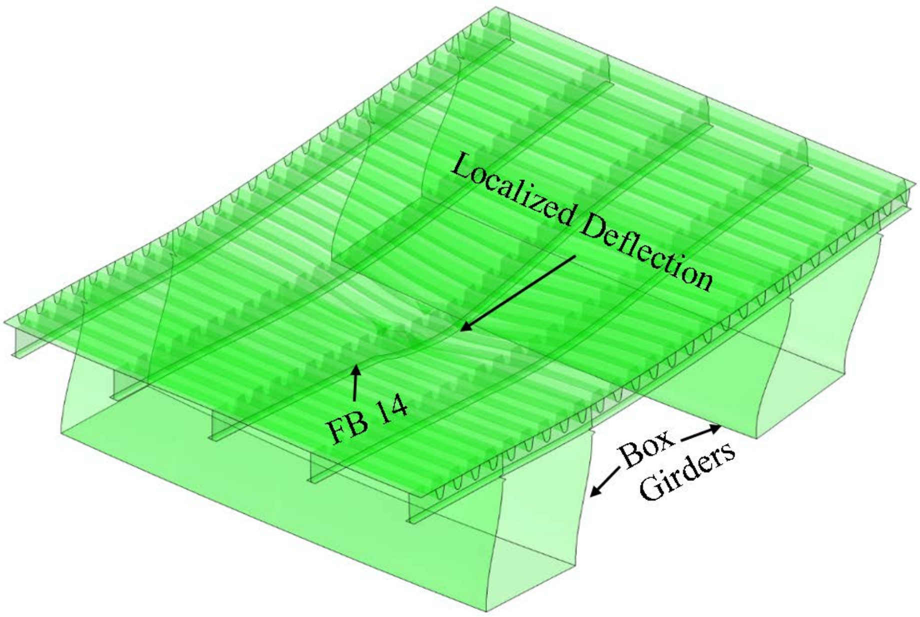

Figure 49. Top view of GM showing localized deflection

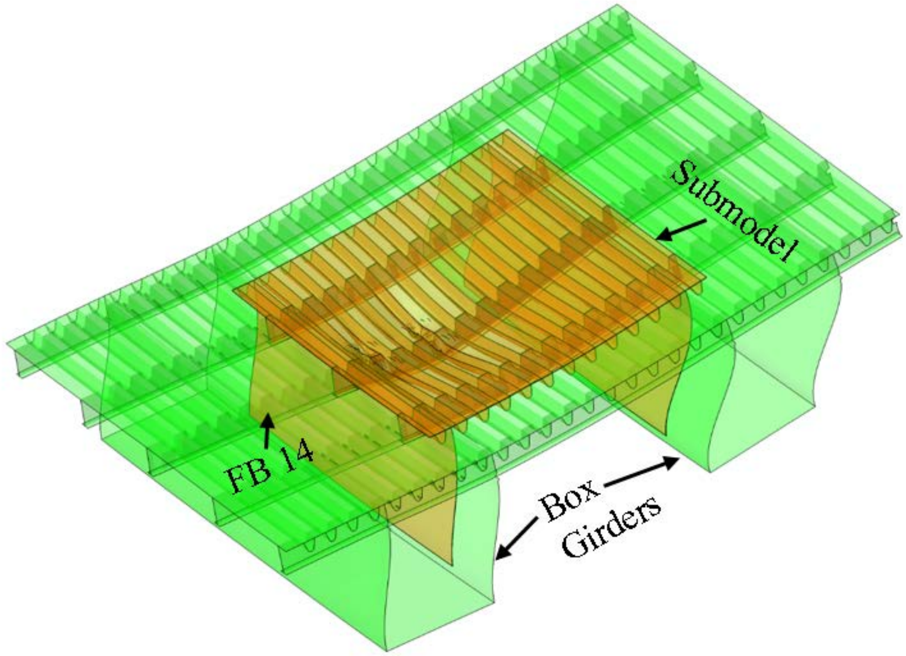

Figure 50. Top view of GM showing extent of SM

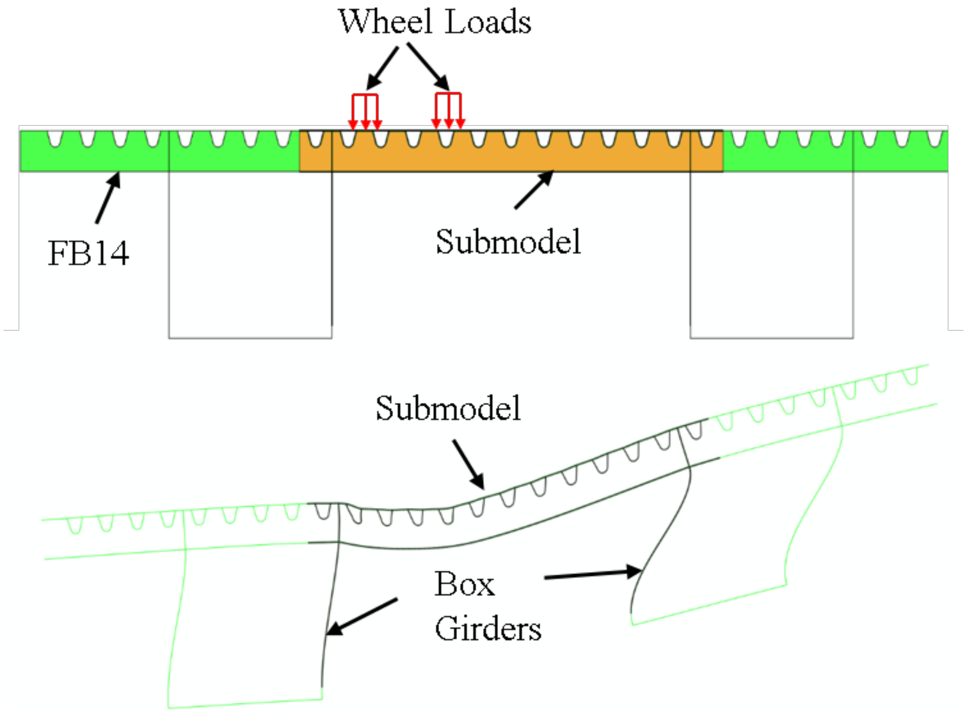

Figure 51. Part cross sections of undeformed and deformed GMs showing the extent of SM

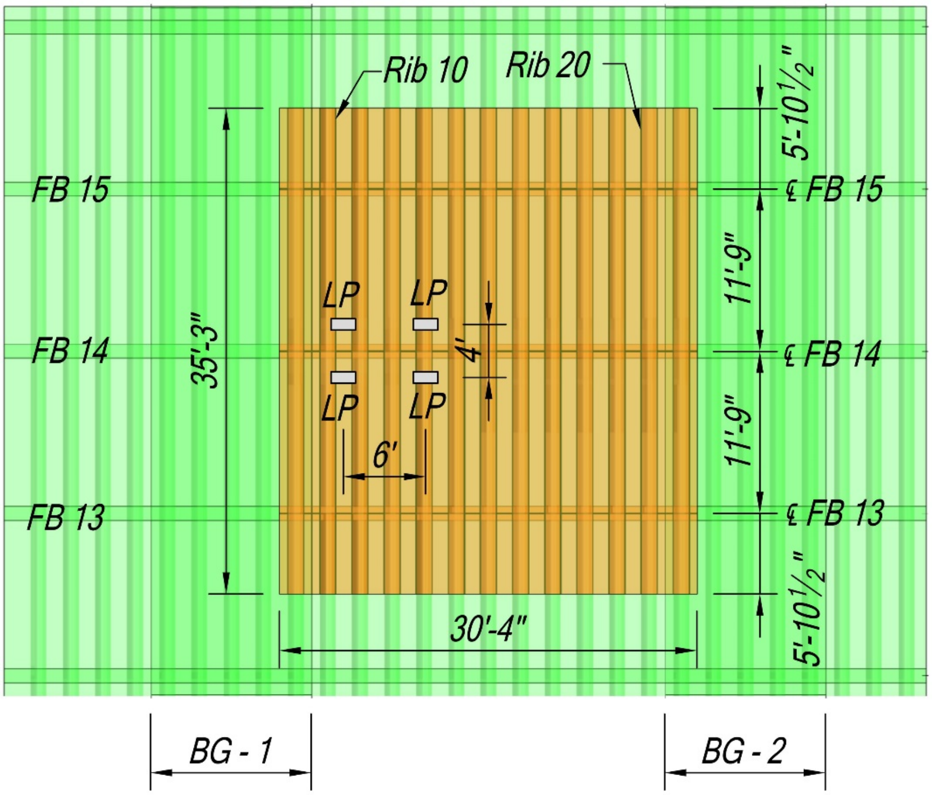

Figure 52. Underside view of GM showing the extent and dimensions of the SM (load positions also marked)

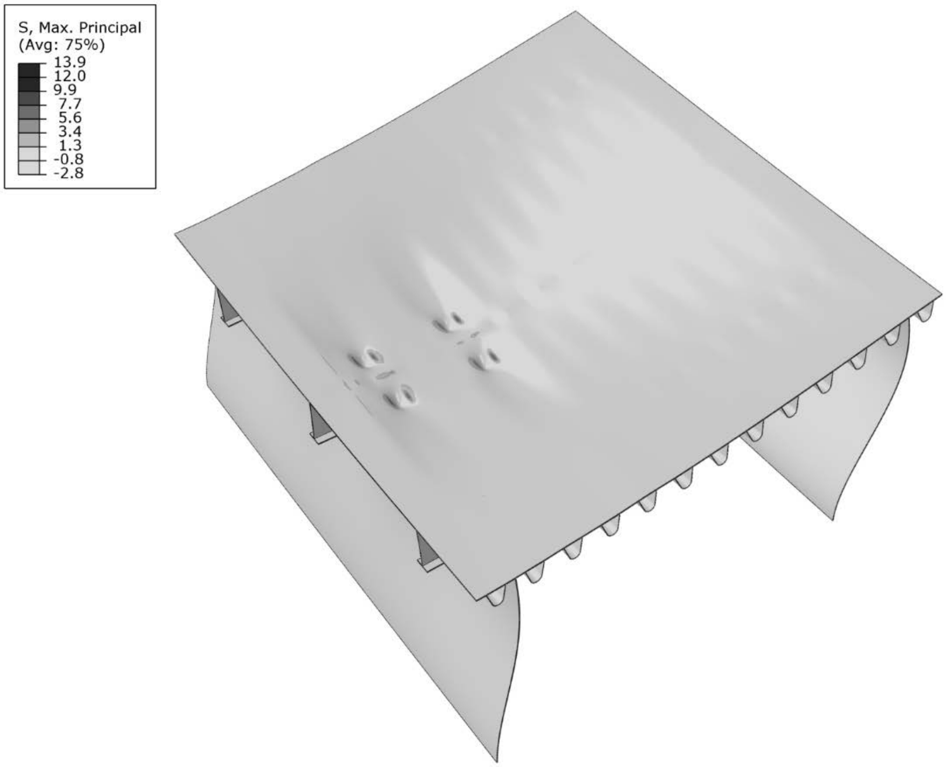

Figure 53. 3D top view of the SM showing the principal stress contour in the deformed configuration

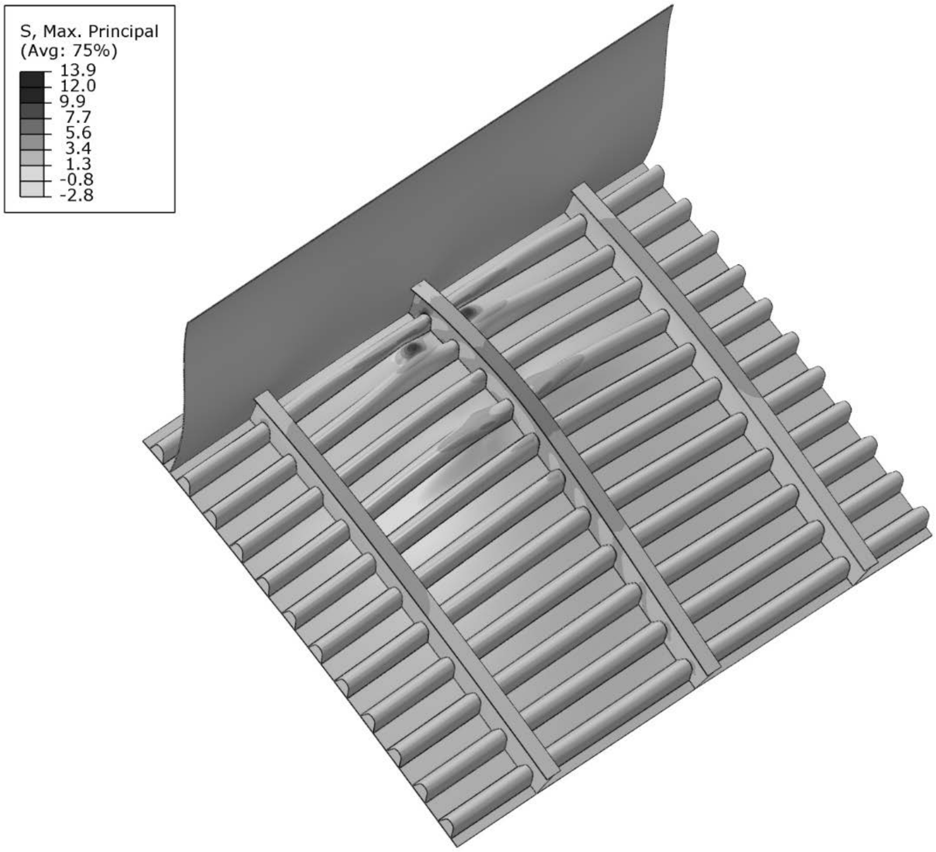

Figure 54. 3D underside view of the SM showing the principal stress contour in the deformed configuration

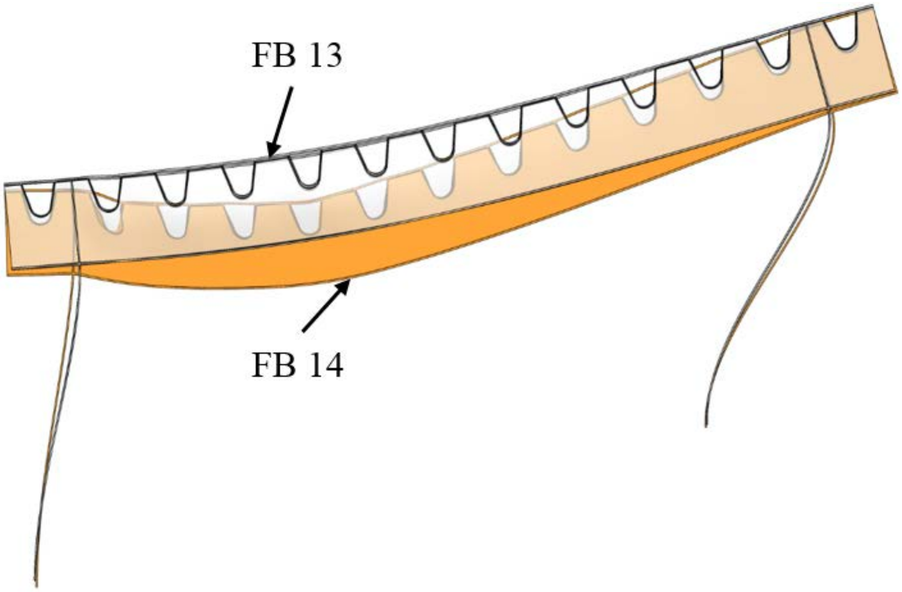

Figure 55. Comparison of deformed configuration of FB 14 and FB 13

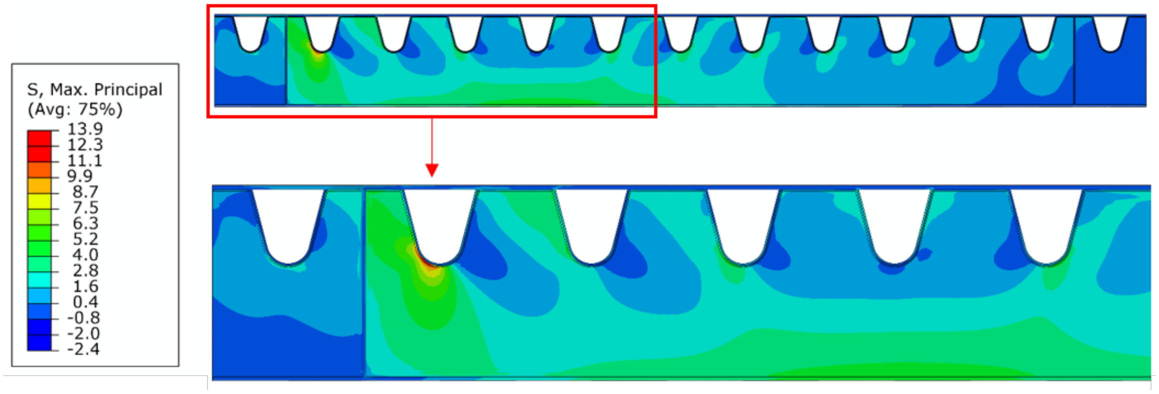

Figure 56. Maximum principal stress in FB 14

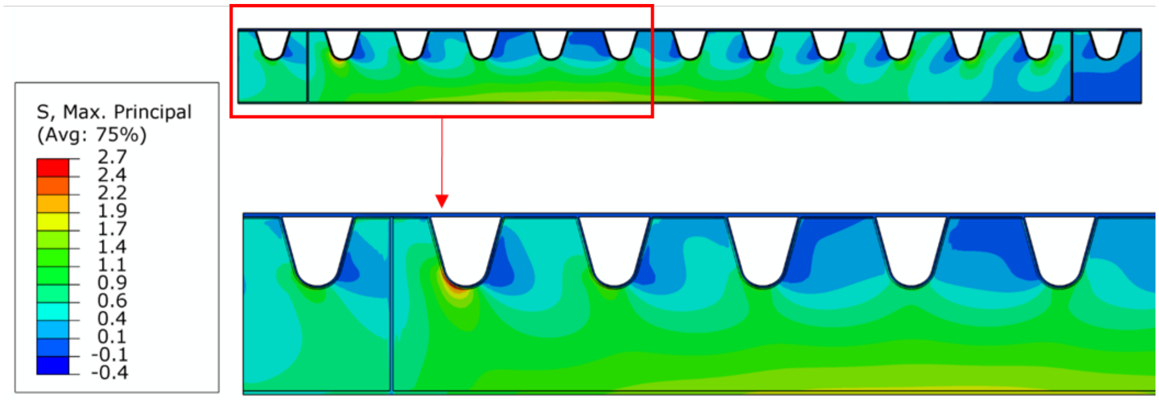

Figure 57. Maximum principal stress in FB 13

3. FABRICATION AND TESTING OF SMALL-SIZE MOCK-UPS

The activities undertaken in Task 4 of the research project related to the fabrication and testing of mockups are reported in this chapter. Economic fabrication of orthotropic deck details is the key to an effective LCC and for successful implementation of orthotropic decks. Accordingly, the influence of various parameters related to the fabrication of the proposed deck was studied, and the most cost effective and fatigue resistant details for the rib-to-floor beam and rib-to-deck plate connections were identified by fabricating, fatigue testing and destructively evaluating three small-size full-scale mockups with different connection details. The mockups were single rib and floor beam specimens and were identified as MU1, MU2 and MU3. The mockups were fabricated by High Steel at their Lancaster facility. After fabrication of the rib-to-deck plate weld, the weld penetration was nondestructively evaluated in each specimen using Phased Array Ultrasonic Testing Technique (PAUT) technique with General Electric (GE) Phasor XS. The mockup specimens were fatigue tested at the Fritz Engineering Laboratory of Lehigh University under simulated AASHTO tandem axle loading using three above-deck actuators. The specimens were instrumented at critical locations as per the instrumentation plan developed based on FEA of the specimen model. The specimens were tested at elevated load levels to promote fatigue cracking and finish the experiment in lesser span of time. As such, the fatigue tests results were only qualitative indication of the fatigue performance of different details.

3.1 Description of the Mockup Details

Cost-effective fabrication of the rib-to-deck plate weld connection is the most significant component of orthotropic deck fabrication because of the sheer length of this connection (twice the length of all the ribs in a deck). Joint preparation, weld penetration and fit-up gap are the most important parameters influencing the cost-effective design and fabrication of this detail. Accordingly, the rib-to-deck plate connection details in the three specimens were designed and fabricated as partial joint penetration (PJP) groove weld with varying degree of joint preparation, fit-up gap and weld penetration to investigate the effect of these parameters. The design of the proposed orthotropic deck for the Wittpenn Bridge specifies an 80% PJP weld at the rib-to-deck connection. To be cost-effective, some fabricators prefer to fabricate this weld without joint preparation and using high heat input with submerged arc welding (SAW) process. However, connections fabricated without joint preparation and with high heat input are susceptible to hot cracking and achieving uniform penetration over the production length becomes a concern. Accordingly, this process of fabrication was evaluated in MU1 where the rib wall was left square as cut without any joint preparation. As an alternative, if a bevel is used with SAW process, the landing width and travel speed should be adequately controlled to prevent weld melt-through and blow-through conditions when higher penetration is attempted. Different degrees of bevel with different landing widths, fit-up gaps and target penetrations were evaluated in MU2 and MU3.

The three rib-to-deck plate connections details are shown in Figure 58. The rib-to-deck plate connection in MU1 was specified as a 80% PJP weld without any joint preparation on the rib wall resulting in a natural bevel of 15 degree (note that the taper of the rib was

75 degree) and the fit-up gap between the nearest rib corner and the deck plate was limited to 0.025 in. (0.6 mm). The specified degree of penetration and fit-up-gap in MU2 was same as MU1, except the connection was fabricated with a bevel of 35 degree on the rib wall and a root face (or landing) of $^{3}/_{32}$ in. (2.4 mm). The rib-to-deck plate connection in MU3 had a lesser specified weld penetration than the other 2 specimens. The connection was specified as a 70% PJP weld and it was fabricated with a bevel of 30 degree on the rib wall and a landing of $^{5}/_{32}$ in. (4 mm). The fit-up gap was limited to 0.020 in. (0.5 mm).

The design of the proposed orthotropic deck for the Wittpenn Bridge specifies a fillet welded detail for the rib-to-floor beam connection. Despite the complex distribution of in-plane and out-of-plane effects, it is a common perception that a proper design of orthotropic deck will produce predominantly in-plane stresses at the rib-to-floor beam connection. Therefore, perceived to be cost-effective without any efforts for joint preparation, the rib-to-floor beam connection was designed as fillet-welded. Inherently, fillet welds have minimum penetration into the connected elements and produce large lack of fusion (LOF) at the weld root. The strength of the fillet welds is defined by the throat of the weld. To avoid an insufficient weld throat and avoid fatigue cracking through the weld throat, a very tight gap tolerance or fit-up of $^{1}/_{32}$ in. (0.8 mm) was specified. Due to the variations in the rib manufacturing and attachment of the ribs to the deck plate prior to welding the floor beam to the ribs, however, additional fabrication efforts in terms of match cutting and/or grinding the floor beams were anticipated for achieving the desired fit-up. This fit-up between the rib and floor beam is critical for suppressing fatigue growth from the weld root of this fillet welded rib-to-floor beam connection. To investigate the additional efforts and performance, two variations of the fit-up for the fillet welded connection were investigated in MU1 and MU2. As an alternative, another rib-to-floor beam connection detail (MU3) was investigated that employed a Partial Joint Penetration (PJP) weld with joint preparation on the floor beam, but with a larger fit up gap. A smaller LOF in PJP weld eliminated the possibility of reduced throat thickness due to the larger fit-up gap. Despite additional efforts for joint preparation, it was anticipated that MU3 detail could be cost-effective with lesser efforts for the floor beam fit-up.

The three rib-to-floor beam connection details are shown in Figure 58. The rib-to-floor beam connection in MU1 was specified as $^{5}/_{16}$ in. (8 mm) fillet weld and had a design fit-up gap of $^{1}/_{32}$ in. (0.8 mm). The stringency on the fit-up gap was relaxed in MU2, where the target fit-up gap was increased to $^{1}/_{16}$ in. (1.6 mm) with a maximum of 2.4 mm ($^{3}/_{32}$ in.). The PJP welded detail in MU3, had a 45° bevel on both sides of the floor beam web. The target fit-up gap was specified as $^{3}/_{32}$ in. (2.4 mm), with a maximum limit of $^{1}/_{8}$ in. (3 mm).

3.2 Design of Mockup Specimens

To better utilize the mockup specimens and to obtain advanced information on the performance of the deck details, the mockup specimens were proposed to be fatigue tested under simulated one side wheel pair of AASHTO tandem axle loading with simple boundary conditions. The proposed mockup specimens had to be modified to accommodate the load pads for the critical load position which was determined from FEA. In the transverse direction the deck plate was increased by 8 in., but the in the longitudinal direction the length of the mockup specimen was maintained the same. The descriptions of the proposed and the modified mockup specimen are given below in subsequent articles.

3.2.1 Proposed Mock-up Specimen

The proposed mockup specimen consisted of a deck plate 6 ft. long and 3 ft. wide, with a floor beam at the center of the span (representing FB 14) and a rib (representing Rib 10) passing through the cut-out in the floor beam. The plan, elevation and section of the proposed mock-up specimen are shown in Figures 59, 60, and 61 respectively.

3.2.2 Modified Specimen

FEA of the global model showed that transverse load position 29 produced the most critical stress for longitudinal load case 1 at the Rib 10-to-FB 14 connection adjacent to box girder BG-1. For this load case, the centerline of the near side wheel pair was 1 ft. 2 in. (356 mm) from the centerline of Rib 10. The width of the proposed mockup specimen was not enough to accommodate the near side wheel pair of the tandem axle which will replicate the one side wheel pair of the tandem axle for transverse load position 29. Initially, the loads were positioned as close as possible to load position 29. However, FEA of the global model and submodel showed that the shear force in the floor beam web was predominantly responsible for the high stresses at the rib-to-floor beam connection. 3D FEA of the mockup specimen was conducted to design the size of the specimen for testing. FEA of specimen model showed that moving the load closer to the rib wall due to absence of additional width was resulting in less shear force which in turn was causing less stress in the connection as compared to the submodel analysis results. After analyzing more than 40 alternatives for the mockup specimen, it was decided to extend the mockup specimen on the loading side by 8 in. in the transverse direction (width) to accommodate the wheel pair and to get the exact eccentricity for the load, which in conjunction with appropriate test setup produced similar critical stress state in the specimen model as of the submodel. In the longitudinal direction, the length of the mockup specimen was maintained the same. The 3D view of the modified mockup specimen is shown in Figure 62. The plan and the section view of the modified mockup specimen are shown in Figures 63 and 64 respectively. The modification of the specimen involved increasing the deck plate and the floor beam web on the loading side. This was accomplished by welding a 6 ft long 8x8x3/4 in. angle section to the deck plate by a complete joint penetration (CJP) groove weld with 35 degree bevel and back gouge, but without backing bar. This detail simulated the longitudinal field splice between the orthotropic deck panels, and fortuitously provided an opportunity to investigate the welded splice in deck plate. The angle section produced the stiffening effect which was required to simulate the continuity effect. A ½ inch (13 mm) thick plate was bolted spliced to the floor beam web to provide the continuity for the floor beam web. The details of the modified mock up specimen is shown in Figure 65. On the other side, the continuity of the floor beam was achieved by a beam fixture (Figure 66) of almost the same cross section as the floor beam. The beam fixture was designed to be spliced to the deck specimen using bolts. The details of the beam fixture is given in section 3.6.2. The specimens were oriented along the east west direction of the laboratory. This direction convention will be used in subsequent texts.

3.3 FEA of Mockup Specimens

3.3.1 Details of the Specimen Model

FEA of the .mockup specimens were performed using 3D solid elements to analytically predict the behavior of the specimens, to decide on the locations of strain gauges and to check with the experimental measurements. The welds were modelled as $^5/_{16}$ fillet welds with idealized zero notch radius at the weld toes and complete penetration at the weld root. However, the CJP groove weld between the angle and the deck plate and the splice connection between the ½ in. plate and the floor beam web on the loading side were modelled as tie constraints with hard contact definition between the mating surfaces. The splice connection between the fixture beam and the deck specimen on the other side was also modelled as tie constraint with hard contact definition between the mating surfaces.

3.3.2 Material Properties

Widely accepted linear elastic material properties of steel were used for analysis. The modulus of elasticity and Poisson’s ratio of steel were assumed as 29000 ksi and 0.3 respectively.

3.3.3 Element Type and Meshing

The specimen model was meshed with 3D continuum solid hexahedral elements, incorporating twenty node, quadratic, reduced integration and isoparametric formulation. In ABAQUS, this element is identified as C3D20R. For correct assessment of stresses at the welded connections, finer meshing was required. As recommended by ABAQUS, elements with aspect ratio greater than 10 or with face angle as less than 10° or with the large face angle greater than 160° were avoided for better accuracy of data. The specimen model was meshed with an average minimum mesh size of 0.25 in. and an average aspect ratio of 1.3. The submodel consisted of 508,734 elements and 2,428,650 nodes, generating 7,277,667 solution variables or nodal degrees of freedom.

3.3.4 Loading

The specimen model was analyzed for the most critical load position (L1T29) as determined from the FEA of the global model. The width of the specimen was such that it could accommodate only one side wheel pairs of the tandem axle. The wheel pairs are identified as east actuator and west actuator in Figure 67, as it identifies the location of the actuators during fatigue testing. But the other side wheel pairs were also contributing to the magnitude of shear force in the floor beam web as it was observed in the submodel analysis. So the effect of the other side wheel pair was also taken into account by placing a third actuator in the middle of the east and the west actuators. The third actuator is identified as the middle actuator in Figure 67. The purpose of the third actuator was to simulate the effect of the other side of the wheel pairs as shear on the floor beam however the deck plate would not see any effect of this load. So the actuator was placed matching its center line to the center line of the floor beam web so that the load was directly transmitted to the floor beam and the deck plate sees no effect of it. It was observed from the submodel analysis results that the stresses normal to the weld toe in the floor beam web at the rib-to-floor beam connection was much less than the CAFT of the detail, which is categorized as Category C detail in AASHTO with a CAFT of 10 ksi. Since, the purpose of testing the mockup specimens was to qualitatively assess the different connection details, it was decided to test the specimens at relatively higher load level as compared to the load level of AASHTO Fatigue I Limit Load (AASHTO 2012) for orthotropic decks, in order to promote fatigue crack growth. So the applied load from the east and west actuators were 25 kip instead of 20.7 kip load following AASHTTO. As the middle actuator was representing both the wheel pairs on the other side, the load level in the middle actuator was double that of the other actuators i.e. 50 kip. The load levels in the three actuator are shown in Figure 67.

The load from each of the east and west actuators was uniformly distributed over a rectangular load patch of 10 in. long and 20 in. wide as specified by AASHTO LRFD Bridge Design Specifications (AASHTO 2012). Although a transverse gap of 1 in. exists in the middle of each wheel pairs, it was ignored in the idealized rectangular wheel contact for simplicity in modelling. The load from the middle actuator was distributed over a rectangular load patch of 10 in. long and 10 in. wide. As seen from Figure 68, the load patches for the east and west actuators were symmetrically placed 2 ft. on either side of FB 14 resulting in a spacing of 4 ft. between the two axles. The spacing between the load patches was consistent with the latest provisions of the AASHTO LRFD Bridge Design Specifications (AASHTO 2012). The load patch for the middle actuator were placed with its centerline coinciding with the centerline of the floor beam web (Figure 68). In the transverse direction (Figure 69), the position of the load patches was consistent with the transverse load position T29 of the tandem axle.

3.3.5 Boundary Condition

The specimen was loaded in a cantilever configuration with all the boundary conditions applied to the beam fixture (Figure 70). The beam fixture was given roller boundary condition at the near end with the floor beam to simulate the support of the right web of box girder BG-1, where in-plane rotation and horizontal displacement of the beam fixture and the floor beam was allowed. At the far end, the beam fixture was given fixed boundary conditions with negligible moment restraint. The boundary conditions to the beam fixture was applied at sections coinciding with the locations of lab floor anchors. The distance between the two sections was 5 ft. (1.5 m) which was essentially the lab floor anchor spacing.

3.3.6 Analysis Results

The contour of maximum principal stress in the deck is shown in Figure 71 in the underside view of the deformed configuration of the deck. The stresses are presented for 25 kip loads in the east and west actuators and 50 kip load in the middle actuator, resulting in a total load of 100 kip. Similar to the global model and submodel analyses, the deformed configuration of the deck shows that the deformations were concentrated under the load patches and decreased rapidly away from the load patches. The deck plate didn't see any significant stress under the middle actuator, as the load from the middle actuator got directly transmitted to the floor beam. It can also be seen that the maximum principal stresses were highly localized under the east and the west load patches as is seen as black patches, and away from the load the stresses were insignificant. Figure 72 shows the distribution of normal stress on the top and the bottom surfaces of the deck plate along a section through the centerline of the east load pad. As is evident from the figure, stresses were highly localized under the load pads and gradually decreased away from the load pads. The deck plate deformed in different curvature under the load pads away from the rib-to-deck connection and at the rib-to-deck connection. As expected, due to the stiffness provided by the angle section, the deck deformed in sagging curvature away from the rib-to-deck plate connection and in hogging curvature over the connection. So, the stresses at the top and bottom of the deck plate were compressive and tensile respectively away from the connection, and tensile and compressive respectively over the connection. The stresses on the top and the bottom surfaces of the deck plate were almost of equal magnitude indicating pure bending of the deck plate.

The principal stress contour in the floor beam web along with the fixture beam in a deformed configuration of the deck is shown in Figure 73. The principal stress contour in the floor beam web alone is shown in Figure 74. The distribution of principal stress in the floor beam web was similar to that observed in the global and the submodel analyses. Similar to the global model and submodel, the wheel loads were transferred to the simulated box girder support through the floor beam by shear. The transfer of wheel loads as shear to the box girder support resulted in a diagonal tension field from the bottom (tension) flange of the floor beam to the top corner formed by the floor beam web and the simulated box girder web section. The shear induced tensile stress field in the floor beam web was interrupted by the cutout, and the stress field deviated around the cutout. As a result, high stress concentration developed in the web at the rib-to-floor beam connection weld toe, locally at a region where the tension fields were approximately tangential to the cutout. Stresses were tensile at the connection towards the fixture beam or the north side, and compressive towards the loading or the south side. It should be noted that after the simulated box girder section on the north side of the specimen, stresses became tensile on the top flange of the fixture beam and compressive at the bottom flange of the fixture beam. This distribution of principal stress is expected as the deck was loaded in a cantilever configuration and deck deformed in hogging curvature in the between the two sections where boundary conditions were applied. The maximum principal stress in the floor beam web at the rib-to-floor beam connection was about 25.5 ksi (176 MPa) as compared to 12.5 ksi (86 MPa) in submodel analysis. The principal stress in the specimen model was much higher than the submodel or global model, because it was envisaged to the test the specimens under higher load levels to promote fatigue cracking and accordingly the specimen model was also analyzed for a much higher load levels (see section 3.3.4) as compared to the submodel or global model.

The three mockup specimens MU1, MU2 and MU3 were fatigue tested at slightly different load levels than the load level of the specimen model. This slight deviation in load levels was due to the limitations of the laboratory loading system. The detail of the test loads for the three mockup specimens are given in in section 3.6.4. However, the specimen model was later analyzed for the test load levels of the three specimens. The principal stress contour in the floor beam web analyzed under the three different test load levels are shown in Figures 75, 76, and 77 for MU1, MU2 and MU3 respectively. The maximum principal stress in the floor beam web at the rib-to-floor beam connection was about 26 ksi (180 MPa), 27.3 ksi (188 MPa) and 26 ksi (180 MPa) for MU1, MU2 and MU3 respectively.

Fatigue cracking at the weld toe is primarily attributed to the crack growth from the micro discontinuities subject to the stress range normal to the weld toe. Figures 78, 79, and 80 show the variation of normal stress on floor beam surface normal to the weld toe around the rib for MU1, MU2 and MU3 respectively. The maximum tensile stress in the floor beam web normal to the rib-to-floor beam weld toe was much higher than the CAFT of the connection as specified by AASHTO. As such, fatigue cracking was expected at the rib-to-floor beam weld toe in all the three specimens. The maximum tensile normal stresses were about 14.9 ksi (103 MPa), 14.4 ksi (99 MPa) and 15.7 ksi (108 MPa) for MU1, MU2 and MU3 respectively, and they occurred at a section at about 50° from the soffit of the rib at the centerline. The maximum compressive normal stresses were about 15.8 ksi (109 MPa), 16.7 ksi (115 MPa) and 15.4 ksi (106 MPa) for MU1, MU2 and MU3 respectively, and they occurred at a section at about 53° from the soffit of the rib at the centerline. Similar to the submodel, a localized reverse bending of the rib wall at the rib-to-floor beam welded connection was observed as shown in Figure 81.

Fatigue cracking the rib-to-floor beam connection can also occur from the volumetric discontinuities at the weld root, and hence circumferential stress at the weld root becomes critical for assessment of fatigue performance. Figures 82, 83, and 84 show the variation of circumferential stress at the weld root of the rib-to-floor beam connection around the rib bottom for MU1, MU2 and MU3 respectively. The maximum tensile circumferential stresses at the weld root were about 24.6 ksi (170 MPa), 25 ksi (173 MPa) and 24.8 ksi (171 MPa) for MU1, MU2 and MU3 respectively, and they occurred at about 50° from the rib soffit at the centerline. The maximum compressive circumferential stresses at the weld root were about 31.1 ksi (215 MPa), 31.8 ksi (219 MPa) and 31.1 ksi (215 MPa) for MU1, MU2 and MU3 respectively, and they occurred at about 56° from the rib soffit at the centerline. It should be noted the circumferential stresses at the weld root of the rib-to-floor beam connection were much higher than the stresses in the floor beam web normal to the weld toe.

3.4 Fabrication of Specimens

The three specimens (MU1, MU2 and MU3) were fabricated by High Steel at their Lancaster facility. As stated earlier, the modification of the mockup specimens was accomplished by welding an angle section to the deck plate (Figure 85) and splicing a web plate to the floor beam (Figure 86). The rib-to-deck plate welding was performed prior to the rib-to-floor beam welding. The rib was bent to the desired profile in a brake press and was pressed down on the deck plate in an inverted position and tack welded at regular intervals. The rib-to-deck plate welds were produced by a single pass of SAW process using a semi-automatic travelling overhead gantry, where the welds on both sides of the rib were deposited simultaneously in a horizontal position (Figure 87). The floor beams were cut according to designed rib profile. Significant efforts were then spent for fitting the floor beam around the as-fabricated rib to achieve the desired fit-up (Figures 88 and 89). The rib-to-floor beam welds were produced manually by Gas Metal Arc Welding (GMAW) process as shown in Figure 90. The specimens were delivered to Lehigh University on September 10, 2012.

3.5 Non-destructive Inspection using PAUT

After welding the rib to the deck plate, the weld penetrations of the PJP welded rib-to-deck plate connections in MU1, MU2 and MU3 was measured non-destructively using PAUT. The measurements were performed using GE equipment model Phasor XS, which did not have encoding capability to record continuous inspection data (Figure 91). As such, screen capture of the equipment readings or snap shots of the inspection were recorded only at discrete sections along the rib-to-deck welded connections. The locations of the sections, where PAUT measurements were captured, are shown in 92 and 93. The first section was at 3 in. from the end where the testing was initiated, and the subsequent sections were at 6 in. intervals, resulting in 12 sections for the connection on each side of the rib in a specimen. With reference to east-west orientation of the ribs in the laboratory during fatigue testing of the mockup specimens, these sections were located on each specimen: from east to west as A to F and G to L on the south-east and the south-west rib segments respectively; and from west to east as M to R and S to X on the north-west and the north-east rib segments respectively. The sections were identified by paint marks on the mock-up specimens and are shown in Figure 91. After completion of the fatigue tests, the weld penetration was measured destructively at the same sections for verifying the PAUT measurements and for setting up a calibrated inspection protocol for the PJP welded connections using PAUT. The comparison between the PAUT and the destructive measurements for MU1, MU2, and MU3 is discussed in section 5.2.1. Further comparison of PAUT with destructive measurements for subsequent specimens is given in section 7.2.1.

3.6 Laboratory Testing

3.6.1 Test Setup

The north and west elevation of the test set-up is shown in Figures 94 and 95 respectively. The mockup specimens spanned along the east-west direction of the laboratory. The existing frame located at the west side of the Fritz Engineering Laboratory in Lehigh University was selected as the frame to support the specimen and the related fixtures. An arrangement comprising of two cross beams and two longitudinal beams identified as the loading beam, was used to hang the three above-deck actuators. The description of the loading is given in section 3.6.4. The four existing frame columns at the west end of Fritz Engineering Laboratory in Lehigh University were chosen to support the two cross beams. The existing columns were W14x233 sections. The columns were welded to the base plates and were securely fastened to the lab base by ϕ3 inch bolts and base plate arrangement. The cross beams were fabricated from W30x326 sections. The flanges of the cross beams were trimmed by 1 inch on each of the matting faces (inner faces) for passing vertical rods that were used to hang the loading beam. The loading beam span longitudinally across the cross beam. The cross section of the loading beam was a box section fabricated from steel plates. The top flange of the section was 15½ in. x 1 in., think, the bottom flange was a 12⅞ in. x 1 in. thick and the two webs of the box section were 13 in. x ⅝ in. thick. The total depth of the box section was 15 in. The clear distance between the two web walls was 7⅝ in. The cross section of the loading beam is shown in Figure 95. To increase the flexural rigidity of the loading beam and to reduce the deflection of the beam, the moment of inertia of the beam was increased by putting another loading beam of the same cross section on the top of it. An additional W12X87 column (identified as Safety Column) was used at the south end of the specimens as a safety measure against falling off of the specimen from its fixture. The top of the Safety Column was 0.5 inch below the bottom of the specimen to avoid any contact of the column and the specimen during the test. The clearance was decided based on the detailed calculation of the deflection of the entire set-up under the full capacity of the three actuators. Another steel block was placed closed to the Safety Column to support the Mechanical Counter there to measure the deflection at the tip of the free end of the specimen. The test setup at Fritz lab is shown in Figure 96

The beam fixture which provided the continuity of the floor beam on the other side of the loading was supported on a W12x87 (Column A) column section by a free rocker bearing arrangement at the near side to the floor beam to simulate the support of the box girder web. On the far side, the beam fixture was supported on a W12x190 section (Column B) which was anchored to the laboratory floor with minimum moment restraint. Detailed descriptions of these connections are given in section 3.6.2.

The mockup specimens were loaded in a cantilever configuration by three hydraulic actuators above the deck. The details of the actuators are provided in section 3.6.4. The two outer actuators simulated one side wheel pair of the AASHTO rear tandem axle, while the middle actuator simulated the load effect of the other side wheel pair. The rationale for this loading arrangement is discussed in section 3.6.4.

3.6.2 Test Fixtures

Beam fixture

A single beam fixture was used for all the three specimens. Only the specimens got replaced during the course of the fatigue tests. The beam fixture had different fixtures which are described below in the subsequent paragraphs.

Splice Connection

The mock-up specimen was attached to the beam fixture by means of ½ inch thick splice plates. The web splices were designed to take the vertical shear force due to the loads and the flange splices were designed to take the axial force developed due to the in-plane bending moment in the floor beam. The detail of the splices is shown in Figure 97. All the splice connections were designed as slip critical joints. The floor beam web was spliced to the web of the beam fixture by two vertical columns of ϕ¾ in. bolts with 14 bolts in each column. The flange splices were done using four rows of ϕ¾ in. bolts with 4 bolts in each row. All the bolts were of A325 grade.

Connection with Column A

The beam fixture was connected to Column A by means of a free rocker bearing arrangement procured from the existing inventory and the column was fabricated from a W12x87 section. The logic behind using this type of support was to allow the rotation of the beam at the support without transferring any moment to the column in order to simulate roller type support provided by the box girder web as observed from global model analysis results. The rocker swung like a pendulum within the grooves provided in its top and bottom plates which allowed the rotation of the beam. The detail of the support is shown in Figure 98. The top plate of the bearing was connected to the bottom flange of the beam by using four ϕ¾ in. A325 grade bolts, two bolts on either side of the web of the floor beam. A 2 in. thick plate was fillet welded to the top of the column and the plate was connected to the bottom plate of the bearing by using two ϕ1 in. A325 grade bolts. The column was securely fastened to the lab base by using bolt ϕ3 in. bolts and base plate arrangement.

Connection with Column B

The connection between the beam fixture and column B was designed and detailed as partially fixed. The column was fabricated from an existing W12x190 section. The column was cut to the required size and the top plate attached to the column was removed and a new plate was welded to the top of the column. The column was securely fastened to the lab base by ϕ3 inch bolts and base plate arrangement. The column was welded to both the top and base plates by using partial joint penetration groove weld. The top plate of the column was connected to the bottom flange of the beam by using four ϕ1 in. A490 grade bolts, two on either side of the web of the beam. The detail of the support is shown in Figure 99. Additional measure of safety was adopted by using two 2 in. diameter threaded anchored rods, which were drilled and tapped in the base plate. The anchor rods were securely fastened against the top flange of the beam fixture by using nuts which were tightened against an anchor plate sitting on the top flange in bearing. The anchor rods were not taken into the design consideration of the set-up.

Stiffener Plates

Stiffener plates were used to stiffen the web of the beam fixture at the reaction points i.e. at the column locations. The detail of the stiffener plates is shown in Figure 100. The stiffeners were designed as bearing stiffeners following the specifications of the AASHTO LRFD Bridge Design Specifications. ½ in. thick stiffener plates were fillet welded on either side of the web of the beam fixture. The size of the plates was 5 inch x

½ inch and a chamfer of 1 in. x 1 in. was provided at the corner of its connection to the web to clear up the rounding of the web. The stiffener plates were also used for connecting the vertical bracings to the beam fixture. The connection detail of the bracings to the existing stub column forced to place the center line ¾ in. offset from the center line of the support columns.

<u>Bracings</u>

Single angle sections were used to brace the beam fixture in vertical plane so as to prevent the possible chances of the beam being displaced from its true position during the test. Detail of the bracing connection is shown in Figure 101. The angle sections were fabricated from the L4x4x5/16 angles. The stiffener plates were used for connecting the bracings to the beam fixture. ϕ¾ in. A325 grade bolts were used to connect the bracings to the stiffeners. The bracings were connected to the existing W12x87 stub columns and the bracings were oriented to match the existing bolted-plate connection available at the stub column positions. The stub columns were securely fastened to the lab base by using ϕ3 in. bolts and base plate arrangement. The consideration of the vertical bracing was not taken in designing the test setup; the bracings were there for the purpose of safety.

Safety Column

As mentioned earlier, a Safety Column was placed at the cantilever end of the specimen i.e. at the south side to prevent the falling off of the specimen from the set-up in case of any collapse occurs. The arrangement of the column is shown in Figures Figure 95 and Figure 96. A W12x87 section was used for the Safety Column and was procured from the existing inventory. The height of the Safety Column was 35½ inch. A gap of ½ inch was given between the top of the column and the soffit of the specimen to provide sufficient clearance for the maximum downward deflection of the entire set-up. The column was just placed on the lab floor without any connection and was standing on the floor due to its self-weight only.

Loading Block and Load Pads

Loading block was provided below the above-deck actuators for applying the load to the specimens. The detail of the loading block is shown in Figure 102. A pair of 5/8 in (16 mm) thick rubber pads (load pads) was glued under the loading block to simulate a pair of rubber tires (wheels). Each loading pad was 10 in (254 mm) long and $9^1/_2$ in (241 mm) wide, and were oriented such that the longer dimension was in the transverse direction of the specimen. A transverse gap of 1 in (25 mm) was provided at the center of the loading pads, representing the separation between a pair of tires (wheels). Thus, the outer dimensions of the load pads were 10 in (254 mm) long and 20 in (508 mm) wide, in accordance with the tire patch dimension specified in the AASHTO LRFD Bridge Design Specifications. Guide angles, that were secured on the deck using C-clamps was used to contain the load pads in position during fatigue testing.

3.6.3 Instrumentation

The specimen was extensively instrumented at critical locations to determine its global response and to measure the local stresses at the fatigue sensitive connection details. The gauge arrangements were decided based on the FEA results (Refer section 3.3). The three mockup specimens had the same instrumentation plan. Stresses were measured using surface mounted, encapsulated metallic, bonded or welded electrical resistance strain gauges. The majority of the strain gauges were installed on the floor beam web at the rib-to-floor beam connection. Strain gauges were also installed on the rib wall, majority of them were at the rib-to-floor beam connection. Strain gauges were also installed on the top and bottom surfaces of the deck plate, bottom flange of the floor beam and on the top and the bottom flanges of the beam fixture. In addition, three load cells were employed during the static tests. During the fatigue test, only the load cell at the middle actuator was retained. The vertical displacement of the deck was also measured by a liner variable differential transformer (LVDT) provide at the tip of the cantilever portion of the mock-up specimens.

Details of Sensors

Strain gauges of uni-axial and rosette configurations having different resistances and applicable temperatures were used. Gauges had either 1 mm or ¼ in gauge lengths. Rosettes and strip gauges were used only on the floor beam web at the rib-to-floor beam connection. During the static tests 54 uni-axial gauges of ¼ in. gauge length, 34 uni-axial gauges of 1 mm gauge length, 4 strip gauges with 5 elements of 1 mm gauge length, 4 rosette, 3 load cells and 1 LVDT were installed, involving a total of 124 data channels. During the fatigue test, only the load cell at the middle actuator was retained, involving a total of 122 channels during the fatigue tests. The different types of strain gauges used were:

1. Vishay Micro Measurements LWK-06-W250B-350 uni-axial weldable gauges having 350Ω resistance and ¼ in. (6 mm) gauge length;

2. Texas Measurements FXV-1-11-002LE bondable strip gauges having five gauges of 1 mm gauge length and 120Ω resistance oriented along the length of the strip at 2 mm pitch;

3. Texas Measurements FLA-1-11-002LE uni-axial bondable gauges having 120Ω resistance and 1 mm gauge length; and

4. Texas Measurements FRA-1-11-002LE stacked rosette (also called rectangular rosette) bondable gauges having 120Ω resistance and 1 mm gauge length.

Prior to installation of strain gauges, the surface of the specimen was ground to bare steel at the strain gauge locations. The strain gauges were installed in accordance with the guidelines provided by the strain gauge manufacturers.

3 load cells were used and they were Honeywell 3156 (Tension/Compression Canister Load Cell), having a nominal load limit capacity of 100 kip.

Instrumentation on Deck Plate

16 uni-axial gauges of ¼ in. gauge length and 4 uni-axial gauges of 1 mm gauge length were installed on the top and bottom surfaces of the deck plate. The gauges on the west and the east sides (Figure 103) had the same channel names except, the channel names on the west and the east sides of the rib were prefixed by W and E respectively..

The strain gauges on the deck plate were installed primarily near the rib-to-deck plate weld, symmetrically on the west and east sides of the rib as shown in Figure 104. The detailed location of these gauges is given in Figures 104 and 105. The gauges were oriented in the transverse direction of the deck plate and along the centerlines of the load pads at the east and west sides of the rib. The gauges were installed to measure the transverse bending stress in deck plate and to capture the local out of plane bending of the rib-to-deck plate weld. With reference to east-west orientation of the ribs in the laboratory during fatigue testing of the mockup specimens, it was observed from FEA that the tensile stress increases on the top of deck plate and compressive increases on the bottom of the deck plate as we move from the north end of the specimen to the internal face of the rib wall. The same trend was observed as we moved from the south end of the specimen towards the external face of the rib wall. Due to the presence of steep stress gradient close to the weld toe notch, it was required to capture the peak localized strains. A uniaxial gauge of 1 mm length was installed on the bottom of the deck plate at 0.5t or $^{3}/_{8}$ in. from the weld toe on the deck plate, where “t” is the thickness of the deck plate, both to the east and west intersections of the rib wall (adjacent to the load pads) with the deck plate. The channel names were (W/E)BDP_E1_Avg. To get the overall variation of the stress close to the weld toe, uniaxial gauges of ¼ in. gauge length were installed at 1.5t or 1 $^{1}/_{8}$ in. from the weld toe. The channel names were (W/E)BDP_E2_Avg. The reason behind having gauges at 0.5 t and 1.5 t was to extrapolate the stress values from these two measurements to the weld toe as per the AASHTO recommendations. To measure the high compressive stress near rib corner opposite to the bevel (adjacent to the load pads) as observed from FEA, a uniaxial gauge of 1 mm gauge length was installed at 0.5t or $^{3}/_{8}$in. from the edge of the inner face of the rib wall, both to the east and west intersections of the rib wall with the deck plate. The channel names were (W/E)BDP_I1_Avg. To get the overall variation of the stresses near the connection, uniaxial gauges of ¼ in. gauge length were installed at 1.5t or 1 $^{1}/_{8}$ in. from the inner face. The channel names were (W/E)BDP_I2_Avg.Uniaxial gauges of ¼ in. gauge length were provided on the top of deck plate adjacent to the rib-to-deck plate weld toe, back-to-back with the gauges on the bottom, nearer to the rib walls. As these gauges were under the load pads, they were covered with mastic to prevent getting damaged. The channel names were (W/E)TDP_1_Avg and (W/E)TDP_2_Avg.

Uniaxial gauges of ¼ in. gauge length were installed on the bottom of deck plate on either side of the longitudinal CJP deck splice, abutting the weld toes as shown in Figures 104 and 106. These gauges were oriented in the transverse direction of the deck plate and along the centerlines of the east and the west load pads. The purpose of these gauges was to measure the high tensile stress observed in the FEA near the CJP weld occurring due to transverse bending of the deck. The channel names were (W/E)DSP_1_Avg and (W/E)DSP_2_Avg.

A uniaxial gauge of ¼ in. gauges was provided on the bottom of the deck plate on either side of the intersection of the deck plate with the floor beam, at 0.5t or ¼ in. from the weld toe as shown in Figure 107, where “t” is the thickness of the floor beam web. The gauges were oriented in the longitudinal direction of the deck plate and the section coincided with the centerline of the middle load pad. The purpose of these gauges was to capture the high compressive stress observed in the FEA at the bottom of the deck plate near the deck-to-floor beam connection occurring due out-of-plane bending of the deck-to-floor beam weld. The channel names were (W/E)DPFB_1_Avg.

Instrumentation on Rib

20 uni-axial gauges of ¼ in. gauge length and 22 uni-axial gauges of 1 mm gauge length were installed on the rib wall. With respect to the east-west orientation of the rib in the laboratory during fatigue testing, the strain gauges on the rib wall were installed primarily near the rib-to-floor beam weld, symmetrically on the north and the south sides as well as east and west sides of the rib as shown in Figures 108 and 109. Strain gauges were also installed on both the internal and external faces of the rib wall (adjacent to the load pads) in back-to-back configuration, both to the east and west intersections of the rib wall with the deck plate. The gauge channels were identified by N or S (North or South) at the start followed by W or E (west or east)

All the gauges on the rib wall at the rib-to-floor beam connection were installed symmetrically on the north and the south sides of the rib as well as to the east and the west sides of the rib as shown in Figure 110. The FEA results showed that the maximum stress (tensile) stress in the rib wall normal to the rib-to-floor beam weld toe occurred at a section to the north side of the rib at about 60° from the centerline of the rib soffit. So the weld toe at 60° was identified as the potential zone for fatigue cracking due to high normal tensile stress developing due to stress concentration at the weld toe notch and it was decided to install gauges extensively at that location. Due to the presence of steep stress gradient close to the weld toe, it was needed to capture the peak localized strains to have the correct stress distribution normal to the weld toe along 60° radial line. So a uniaxial gauge of 1 mm gauge length was installed on the rib wall both in the north and the south sides as wells as east and the west sides of the rib, at 0.5t or $^{5}/_{32}$ in. from the weld toe measured normal to the weld toe on the rib, where “t” is the thickness of the rib. The gauges were oriented along a 60° line normal to the rib-to-floor beam weld toe on the rib. The channel names were (S/N)WR_60_1_Avg and (S/N)ER_60_1_Avg on the west and the east sides of the rib respectively. But the area of maximum strain was restricted to a small zone. So it was decided to install another uniaxial gauge of 1 mm gauge length next to this gauge at 1.5t or $^{15}/_{32}$ in. from the weld toe. The channel names were (S/N)WR_60_2_Avg and (S/N)ER_60_2_Avg on the west and the east sides of the rib respectively The reason behind having gauges at 0.5 t and 1.5 t was to extrapolate the stress values from these two measurements to the weld toe as per AASHTO recommendations. To get the total variation of the normal stress along the 60° radial line, uni-axial gauges of ¼ in. gauge lengths were installed at 1 in. and 2

½ in. from the weld toe. The channel names were (S/N)WR_60_3_Avg & (S/N)WR_60_4_Avg and (S/N)ER_60_3_Avg & (S/N)ER_60_4_Avg on the west and the east sides of the rib respectively. It was observed from FEA that the normal stress along the 60° radial line was having almost a constant value after a distance of about 4 in. from the weld toe. So, uni-axial gauges of ¼ in. gauge length were installed along the 60° radial line at 4 in. from the weld toe to capture these constant values of the normal stress or the nominal stress. The channel names were (S/N)WR_60_5_Avg and (S/N)ER_60_5_Avg on the west and the east sides of the rib respectively. Gauges were also installed along the 30° radial line normal to the weld toe. A uni-axial gauge of 1 mm gauge length was placed at 0.5t or $^{5}/_{32}$ in. from the weld toe measured normal to the weld toe in the rib to capture the localized leak strain near the weld toe. The channel names were (S/N)WR_30_1_Avg and (S/N)ER_30_1_Avg on the west and the east sides of the rib respectively. A uni-axial gauge of ¼ in. gauge length was placed after this gauge at 1 in. from the weld toe. The channel names were (S/N)WR_30_2_Avg and (S/N)ER_30_2_Avg on the west and the east sides of the rib respectively. The reason for having these two gauges was to capture the steep gradient near the weld toe, and the stress gradient after 1 in. was almost flat or there was little change in the stress values as observed from FEA. As it was expected to have tensile stress on one side and compressive stress on the other side of the rib soffit along the centerline (0°) and it could also be seen from FEA, stress data on the rib wall near the weld toe at centerline of the rib soffit was required to get the entire stress variation along the rounding of the rib wall on each side. So a uni-axial gauge of 1 mm gauge length was installed along the 0° radial line at 0.5t or $^{5}/_{32}$ in. from the weld toe measured normal to the weld toe in the rib to capture the localized leak strain near the weld toe. The channel names were WR_0_1_Avg and ER_0_1_Avg on the west and the east sides of the rib respectively. A uni-axial gauge of ¼ in. gauge length was placed after this gauge at 1 in. from the weld toe. The channel names were WR_30_2_Avg and ER_30_2_Avg on the west and the east sides of the rib respectively. The reason for having these two gauges was to capture the steep gradient near the weld toe, and the stress gradient after 1 in. was almost flat. Another uni-axial gauge of ¼ in. gauge length was installed along the 0° line at 4 in. from the weld toe to capture the global longitudinal bending response of the deck specimen. The channel names were WR_30_3_Avg and ER_30_3_Avg on the west and the east sides of the rib respectively.

Uni-axial gauges were installed in back-to-back configuration on the rib wall adjacent to the rib-to-deck plate welds as shown in Figure 105 . These gauges were oriented along the inclined depth of the wall. These sections coincided with the centerline of the east and the west actuators. The first set of the gauges were installed at 0.5t or $^{5}/_{32}$ in. from the weld toe measured along the inclined depth of the rib wall. The channel names were (W/E)_RIB_E1 and (W/E)_RIB_I1 on the external and internal faces of the rib wall respectively. Another set of uni-axial gauges were installed next to the first set at 1.5t or $^{15}/_{32}$ in. from the weld toe. The channel names were (W/E)_RIB_E2 and (W/E) _RIB_I2 on the external and internal faces of the rib wall respectively. The reason behind having gauges at 0.5 t and 1.5 t was to extrapolate the stress values from these two measurements to the rib-to-deck plate weld toe on the rib wall.

Instrumentation of Floor Beam

13 uni-axial gauges of ¼ in. gauge length, 8 uni-axial gauges of 1 mm gauge length, 4 strip gauges with 5 elements of 1 mm gauge length and 4 rosettes were installed on the floor beam. The strain gauges on the floor beam were installed primarily near the rib-to-floor beam weld, symmetrically on the north and south sides of the rib as shown in Figures 111 and 112. The gauge channels were identified by N or S (North or South) at the start followed by W or E (west or east)

All the gauges on the floor beam web at the rib-to-floor beam connection were installed symmetrically on the north and south sides of the rib, and on each side the gauges were placed back-to-back on the east and west faces of the floor beam web to measure the in-plane and the out of plane stress components. The FEA results showed that the maximum tensile stress normal to the rib-to-floor beam weld toe on the floor beam web occurred at a section to the north side of the rib at about 50 degrees measured clockwise from the centerline of the rib soffit The maximum normal stress in the rib wall at the rib to floor beam weld occurred at a section to the north side of the rib at about 60° from the centerline of the rib soffit. But the stress at the weld toe on the rib wall was much higher than at the weld toe on the floor beam web. So the weld toe at 60° was identified as the potential zone for fatigue cracking due to high normal tensile stress developing due to stress concentration at the weld toe and it was decided to install gauges extensively at that location. Rosettes and uni-axial gauges were installed along the 60° radial line normal to weld toe as shown in Figure 111 and Figure 112. Bondable rectangular rosettes of 1 mm gauge length were installed on the floor beam web both to the north and the south sides of the rib abutting from the weld toe at 60° to capture the complex stress distribution and to determine the magnitude and direction of the principal stresses at this location. The channel names were N(W/E)FB_(R1/R2/R3)_Avg and S(W/E)FB_(R1/R2/R3)_Avg on the north and south sides of the rib respectively. The middle arm of the rosette R2 (as shown in Figure 113) was aligned along the radial line normal to the weld toe at the 60° location. Due to the presence of steep stress gradient close to the weld toe, it was needed to capture the peak localized strains to have the correct stress distribution normal to the weld toe along 60° radial line. But the area of maximum strain was restricted to a small zone. So it was decide to install a uni-axial strip gauge with 5 gauges of 1 mm gauge length next to the rosette such that the first strip gauge measurement was at 0.5t or ¼ in. from the weld toe (measured along the radial line) where "t" is the thickness of the floor beam web. The channel names were N(W/E)FB_(S1/S2/S3/S4/S5)_Avg and S(W/E)FB_(S1/S2/S3/S4/S5)_Avg on the north and south sides of the rib respectively. Numbering of the strip gauge is shown in Figure 113. Another uni-axial gauge of 1 mm gauge length was placed after the strip gauge at a distance of 1.5t or ¾ in. from the weld toe. The channel names were N(W/E)FB_60_1_Avg and S(W/E)FB_60_1_Avg on the north and south sides of the rib respectively. The reason behind having gauges at 0.5 t and 1.5 t was to extrapolate the stress values from these two measurements to the weld toe as per AASHTO recommendations. Another uni-axial gauge of ¼ in. gauge length was placed at a distance of 3t or 1 ½ in. from the weld toe such that the entire stress variation along the 60° radial line could be obtained from the gauge measurements. The channel names were N(W/E)FB_60_2_Avg and S(W/E)FB_60_2_Avg on the north and south sides of the rib respectively. Gauges were also installed along the 30° radial line normal to the weld toe. A uni-axial gauge of 1 mm gauge length was placed at 0.5t or ¼ in. from the weld toe measured along the radial line to capture the localized leak strain near the weld toe. A uni-axial gauge of ¼ in. gauge length was placed after this gauge at 1.5 t or ¾ in. from the weld toe, so that stress at the weld toe could be derived by extrapolating the stress values at 0.5t and 1.5t. The channel names were N(W/E)FB_30_1_Avg & N(W/E)FB_30_2_Avg and S(W/E)FB_30_1_Avg & S(W/E)FB_30_2_Avg on the north and south sides of the rib respectively. As it was expected to have tensile stress on one side and compressive stress on the other side of the rib soffit along the centerline (0°) and it could also be seen from FEA, stress data on the floor beam web near the weld toe at centerline of the rib soffit was required to get the entire stress variation in the floor beam web along the rounding of the rib wall on each side. So a uni-axial gauge of ¼ in. gauge length was installed on the floor beam web along the centerline of the rib soffit at 0.5t or ¼ in. from the weld toe. The channel names were (W/E)FB_0_1_Avg.

Two ¼ in. gauges were installed in back-to-back configuration on the floor beam web at the intersection with the deck plate under the middle load pad at 0.5t or ¼ in. from the weld toe as shown in Figures 107 and 114. The gauges were a distance of 4 in. from the centerline of the longitudinal splice as shown in Figure 114. The gauges were oriented in the vertical direction (depth direction of the floor beam web) and aligned along the centerline of the load pads. The purpose of these gauges was to capture the transverse out-of-plane bending or distortional stress in the floor beam web. The channel names were (W/E)DPFB_2_Avg. An additional ¼ in. gauge was installed on bottom flange of the floor beam near the splice connection with beam fixture as shown in Figure 115. The gauge was oriented in the transverse direction of the deck and was provided to capture the global bending response of the deck in the transverse direction. The channel name was BDP_WEB_Avg.

Other Instruments

In addition to the strain gauges on the deck plate, rib and the floor beam, strain gauges were also installed on the top and bottom flanges of the beam fixture as shown in Figure 115. These gauges were placed to capture the global transverse bending of the specimen and to measure the in-plane bending stresses in the beam near the support locations. The first set of strain gauges TF_2_Avg and BF_2_Avg were placed on the top surface of the top flange and the top surface of the bottom flange respectively, near the support Column B. The second set of strain gauges TF_1_Avg and BF_1_Avg were placed on the top surface of the top flange and the bottom surface of the bottom flange respectively, near the support Column A. The gauges had to be placed without interfering with the column supports, so they were offset from the column centerlines. With respect to the east-west orientation of the rib during the fatigue testing, the first set of gauges were installed at 1 ft. 6 in. from the north end of the beam fixture, while the second set of gauges were at 2 ft. 9 in. from the first set of gauges.

The applied loads during the static and the fatigue tests were measured by load cells placed between the actuators and the load pads. The arrangement of the load cells is shown in Figure 94. Load cells LC_101_Avg, LC_103_Avg and LC_105_Avg were placed under west, middle and east actuators respectively. During the static tests loads cells were placed under each of the three actuators to verify the load values shown in the dial gauges of the Amsler machine with the actual applied loads on the specimen recorded in the logger. During the fatigue tests, only the load cell at the middle actuator was retained.

Vertical displacement of the deck was also measured by a liner variable differential transformer (LVDT) provide at the tip south end of the mockup specimens, as shown in Figure 115.

3.6.4 Test Load

Three Amsler Actuators were used for loading the specimen, two of them were 55 kip actuators and the other one was a 110 kip actuator. The two 55 kip actuators will be referred as the east and the west actuator and the 110 kip actuator will be referred as middle actuator in subsequent texts. The arrangement of the actuators is shown in Figures Figure 94 and Figure 95, and it replicated the loading used in the FEA of the specimen model. All the actuators were appropriately coupled by means of a coupling shaft so that all the actuators were synchronized and they apply the load simultaneously. The east and the west actuators were used for loading the specimen which simulated one side wheel pair of the AASHTO tandem axle. The east and the west above-deck were placed symmetrically 2 ft. on either side of the floor beam to simulate the symmetric load position, resulting in a 4 ft. spacing between the two actuators following the AASHTO specifications. As discussed earlier, the load from each actuator was distributed through rectangular load pads (simulating the wheel contact with the deck plate) 10 in long and 20 in wide, spaced 6 ft. apart in transverse direction (according to AASHTO LRFD Bridge Design Specifications). In the transverse direction, the actuators were placed representing the transverse load position T29. Submodel analysis showed that the other wheel pair was also contributing to the magnitude of the stress at the rib to floor beam connection. In absence of that load, the stress was less as compared to the Global Model. Accordingly, a third Amsler Actuator was placed in the middle of the two 55 kip actuators to simulate the other side wheel pair. The actuator was placed matching its center line to the center line of the floor beam web so that the load is directly transmitted to the floor beam and the deck plate sees no effect of it.

Since, the middle actuator simulated the load effect of the other side wheel pair, the load level generated by this actuator was double that of the side actuators. The primary purpose of the tests was to evaluate the fabrication conditions by macro-etching the cross sections of the welded connection and to suggest the weld details of the rib to floor beam and rib to deck connections which would be the best for the full-size specimen. As a consequence, the specimens were tested at higher load levels to complete the tests in lesser span of time. However, the load level in the third actuator was kept as close as possible to two times of the load levels in the side actuators during both static and fatigue tests of all the specimens. The values of the loads for the specimens for static and fatigue tests are given in detail in Articles 3.6.5 and 3.6.6 respectively.

3.6.5 Static Tests

General Test Procedure

Prior to initiating fatigue tests, all specimens were tested at a slow loading rate or static loading by using Amsler actuators and pulsators to determine the overall response of the deck, the dynamic load limits and stress limits at the control gauges for the fatigue tests and to shakedown the residual stresses.

Static tests were conducted in an up-down fashion where the loads at the actuators were slowly increased from zero to the maximum load for a particular test and then completely unloading the actuators. Loads were held constant at regular intervals for a brief period for the purpose of recording data. The data was collected by Campbell Scientific digital data logger CR9000. To shakedown the residual stress and to verify the repeatability of tests, the static tests were repeated three times.

During the static tests, data was collected for both the loading and the unloading phases in order to check the presence of hysteresis loop and also to check the linearity of the data. Applied loads were measured in load cells provided in between the Amsler actuators and the loading blocks. Loads were also indicated by the dial gauge in the Amsler pulsators which were correlated with the load cell measurements. Due to this accurate correlation between the dial gauge and the load cells, the load cells under the east and west actuators were replaced by the load cell replacement assembly during the fatigue test. The load cell under the middle actuator was present during the fatigue test as a check for the applied load. In addition to this, a LVDT was placed at the tip of the cantilever specimen for measuring the maximum displacement of the specimen. The load values, record numbers and the displacement indicated by the logger and the load values indicated by the dial gauges in the Amsler machine were also hand recorded on data sheets.

Data was recorded at discreet load levels as discussed in the following.

Static Testing of MU1

Static testing was conducted on October 19, 2012. The load in the middle actuator was increased from 0 kip to a maximum load level of 58.2 kip and then decreased from 58.2 kip to 0 kip. The loads in the east and west actuators were increased from 0 kip to maximum load levels of 27.9 kip and 28.4 kip respectively and then decreased to 0 kip. Data was collected at 0 kip, 10 kip, 20 kip, 30 kip, 40 kip, 50 kip and 58.2 kip load levels in the middle actuator during the loading phase and at 40 kip, 20 kip and 0 kip load levels in middle actuator during the unloading phase.

Static Testing of MU2

Static testing was conducted on November 7, 2012. The load in the middle actuator was increased from 0 kip to a maximum load level of 59.5 kip and then decreased from 59.5 kip to 0 kip. The loads in the east and west actuators were increased from 0 kip to maximum load levels of 28.5 kip and 28.9 kip respectively and then decreased to 0 kip.

Data was collected at 0 kip, 10 kip, 20 kip, 30 kip, 40 kip, 50 kip and 59.5 kip load levels in the middle actuator during the loading phase and at 40 kip, 20 kip and 0 kip load levels in middle actuator during the unloading phase.

Static Testing of MU3

Static testing was conducted on November 15, 2012. The load in the middle actuator was increased from 0 kip to a maximum load level of 58.4 kip and then decreased from 58.4 kip to 0 kip. The loads in the east and west actuators were increased from 0 kip to maximum load levels of 27.9 kip and 28.5 kip respectively and then decreased to 0 kip. Data was collected at 0 kip, 10 kip, 20 kip, 30 kip, 40 kip, 50 kip and 58.4 kip load levels in the middle actuator during the loading phase and at 40 kip, 20 kip and 0 kip load levels in middle actuator during the unloading phase.

3.6.6 Fatigue Tests

General Test Procedure

Fatigue tests were conducted under constant amplitude loading of 4.3 Hz using Amsler actuators and pulsators. The tests were load controlled and monitored by the maximum and minimum loads indicated by the dial gauges in the Amsler testing machine. In addition to this, stresses at four critical gauges were monitored and recorded at every inspection. The data was collected by Campbell Scientific digital data logger CR9000. The specimens were inspected for possible fatigue cracking at an interval of 4 hour with the exception during night time when the last inspection for a day was at 12:00 midnight while the first inspection for the next day was at 8:00 A.M. The inspections were aided with 10X magnifying glass and/or dye-penetration test. During every inspection, load cycles indicated by dial gauges in Amsler machine and also in the CR9000 logger, and the stress values at the four critical gauges were recorded both in hand-written sheet and in Microsoft Excel spreadsheet. Upon detection of a fatigue crack, the time and location of the crack with the corresponding number of cycles were noted.

An automated email system was created to inform the persons involved in the project in case when the load in the middle actuator dropped below 4 kip.

Fatigue Testing of MU1

Fatigue testing was initiated on October 19, 2012 at 3:55 PM. The middle actuator was loaded to a load range of 58.2 kip while the east and the west actuators were loaded to 27.9 kip and 28.4 kip load ranges respectively. The test was conducted round the clock with the inspection schedule as much rigorous as possible. The test was halted for a couple of hours the next day to change the program for the CR9000 logger and the test was restarted at 2:25 PM. Stresses at the strain gauges NEFB_R2, NER_60_1, ER_0_3 and WBDP_E1 were monitored and recorded during every inspections and also other gauges were monitored.

Fatigue Testing of MU2

Fatigue testing was initiated on November 7, 2012 at 3:45 PM. The middle actuator was loaded to a load range of 59.5 kip while the east and the west actuators were loaded to 28.5 kip and 28.9 kip load ranges respectively. The test was conducted round the clock with the inspection schedule as much rigorous as possible. The test was halted for a couple of hours the next day to change the program for the CR9000 logger and the test was restarted at 1:40 PM. The test was again halted on November 9, 2012 at about 5:00 PM to modify the program for CR9000 and was restarted at 5:45 PM. Stresses at the strain gauges NEFB_R2, NER_60_1, ER_0_3 and WBDP_E1 were monitored and recorded during every inspections and also other gauges were monitored.

Fatigue Testing of MU3

Fatigue testing was initiated on November 15, 2012 at 8 PM. The middle actuator was loaded to a load range of 58.4 kip while the east and the west actuators were loaded to 27.9 kip and 28.5 kip load ranges respectively. The test was conducted round the clock with the inspection schedule as much rigorous as possible. Stresses at the strain gauges NEFB_R2, NER_60_1, ER_0_3 and WBDP_E1 were monitored and recorded during every inspection and also other gauges were monitored.

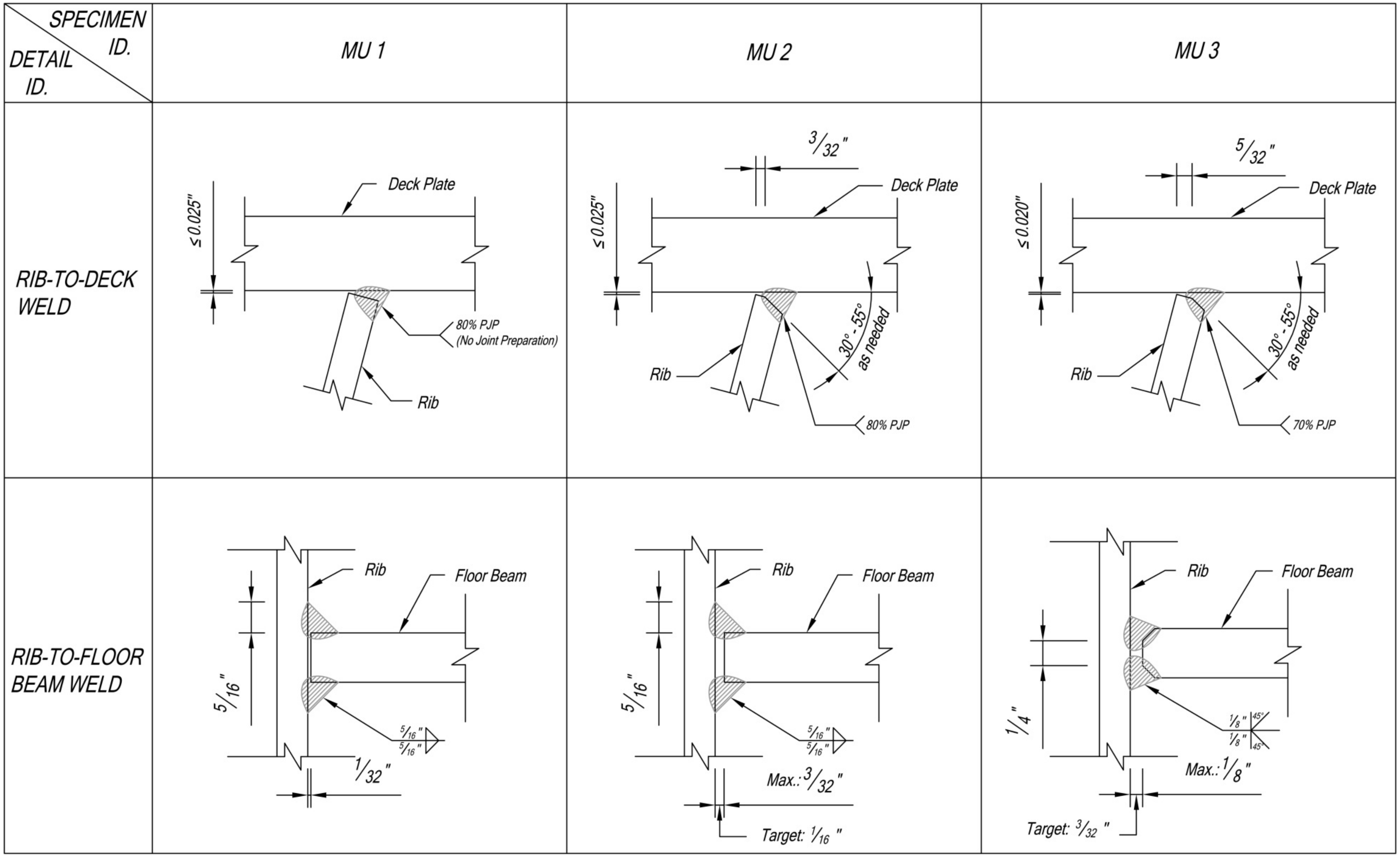

Figure 58. Rib-to-deck and rib-to-floor beam weld details for the three mock-up specimens

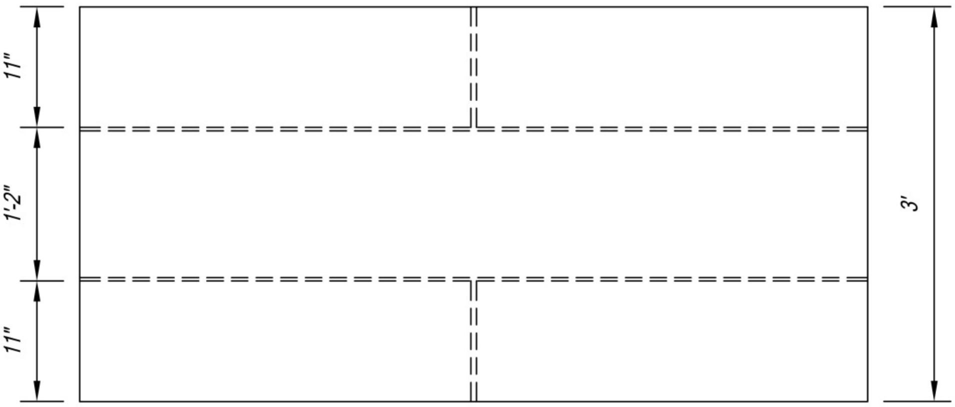

Figure 59. Plan view of proposed mock-up specimen

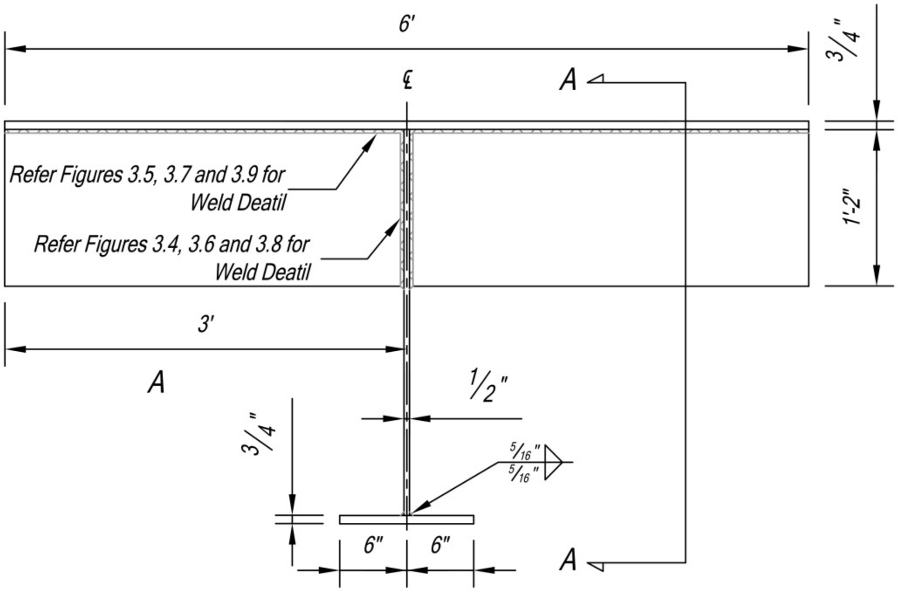

Figure 60. Elevation of proposed mock-up specimen

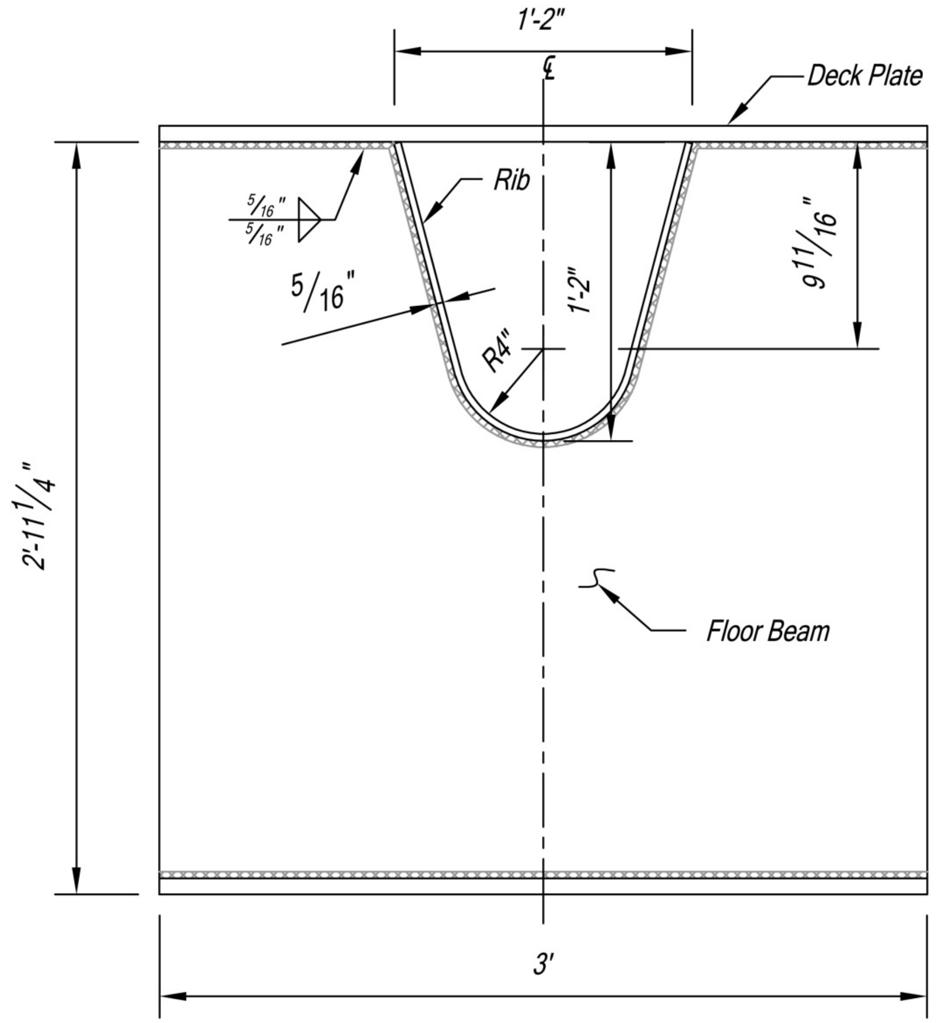

Figure 61. Section A-A (refer Figure 59 for section identification)

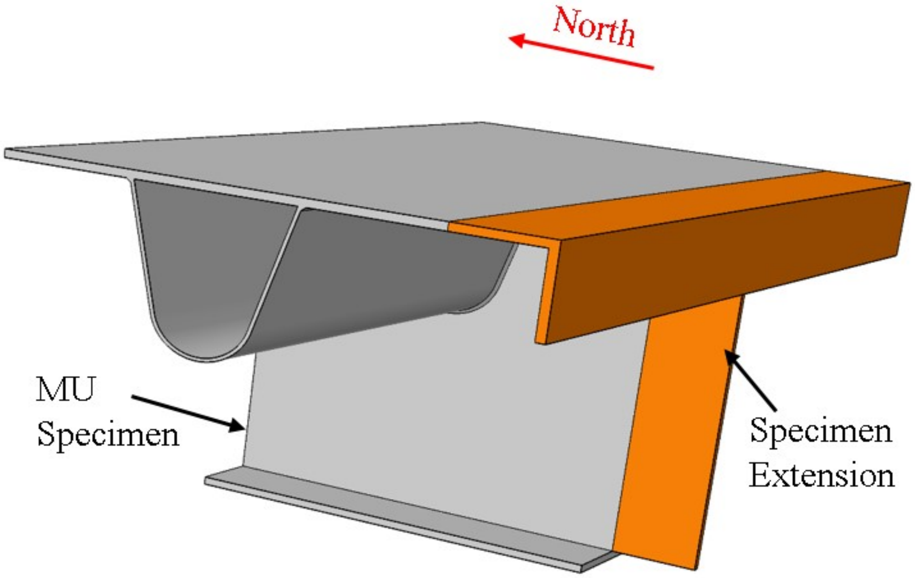

Figure 62. 3D view of the modified mockup specimen

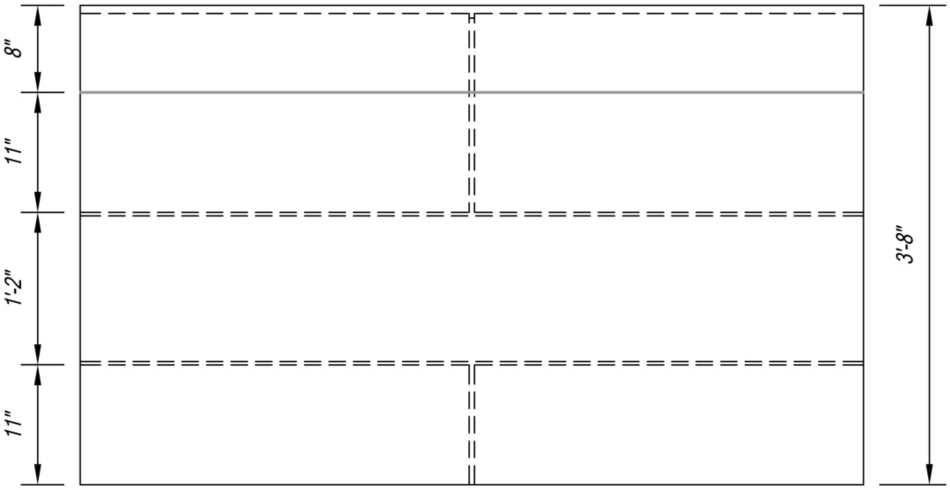

Figure 63. Plan view of modified mockup specimen

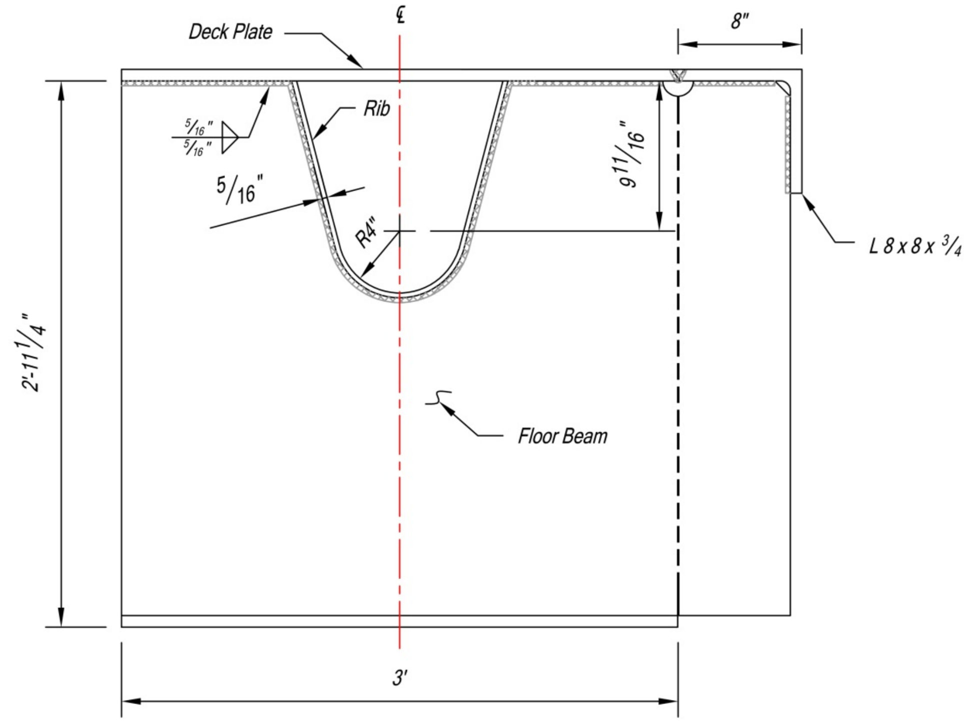

Figure 64. Section A-A of modified mock-up specimen (refer Figure 59 for section identification)

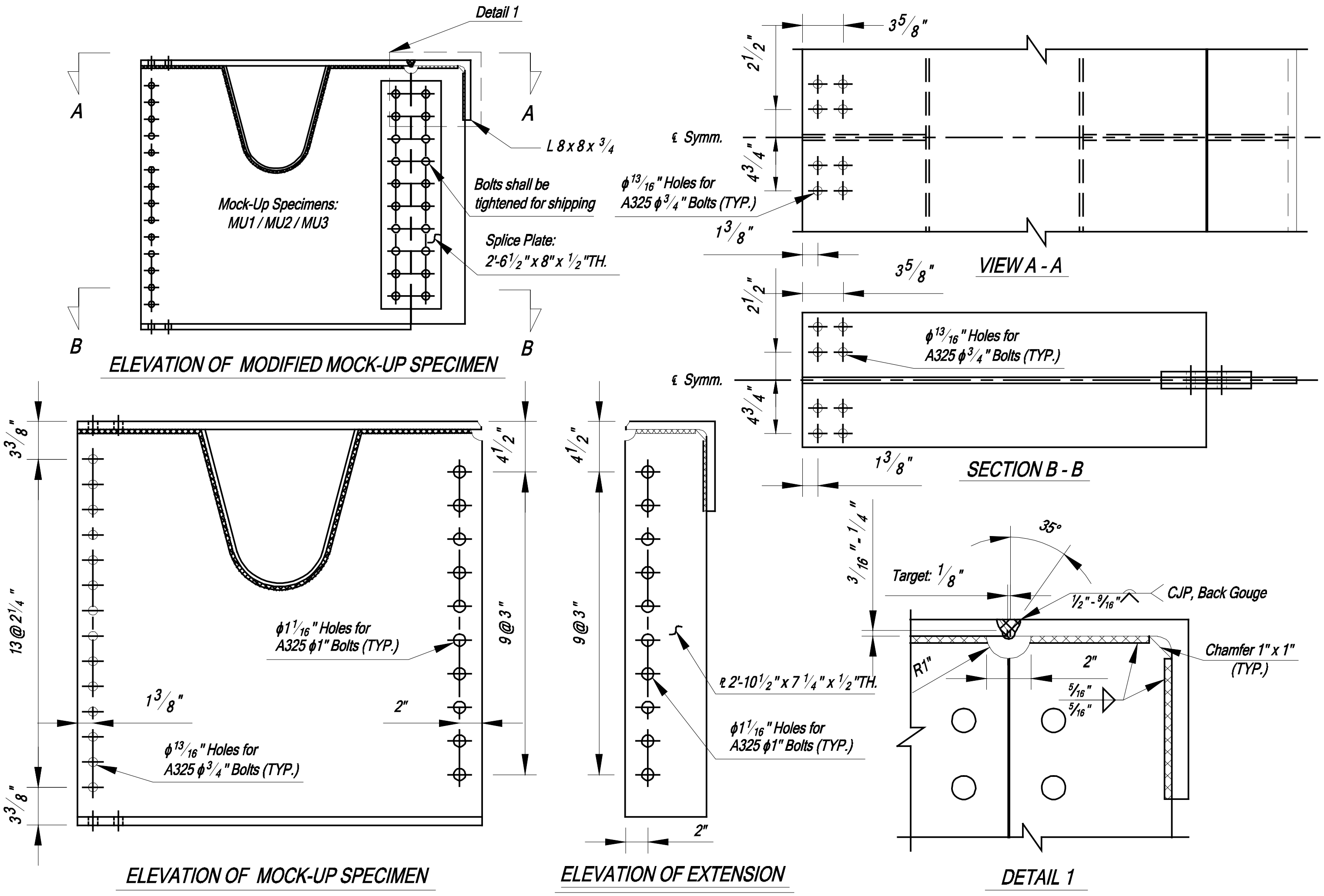

Figure 65. Details of modified mockup specimen

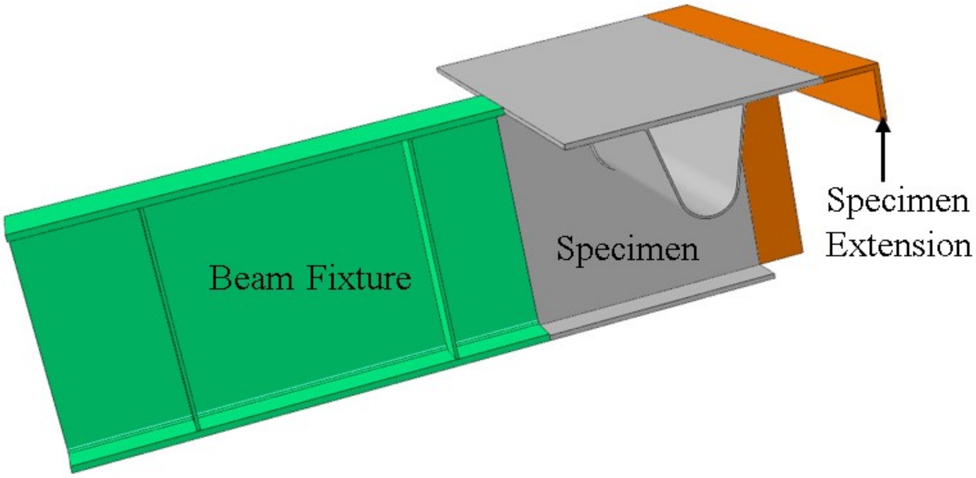

Figure 66. 3D view of the specimen with beam fixture

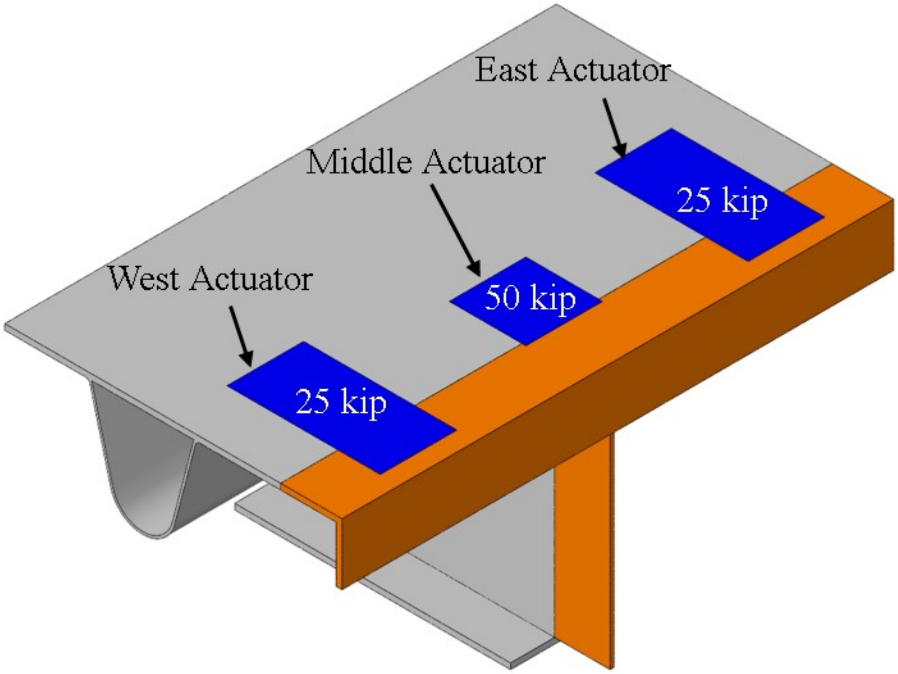

Figure 67. 3D view of the specimen showing the load positions

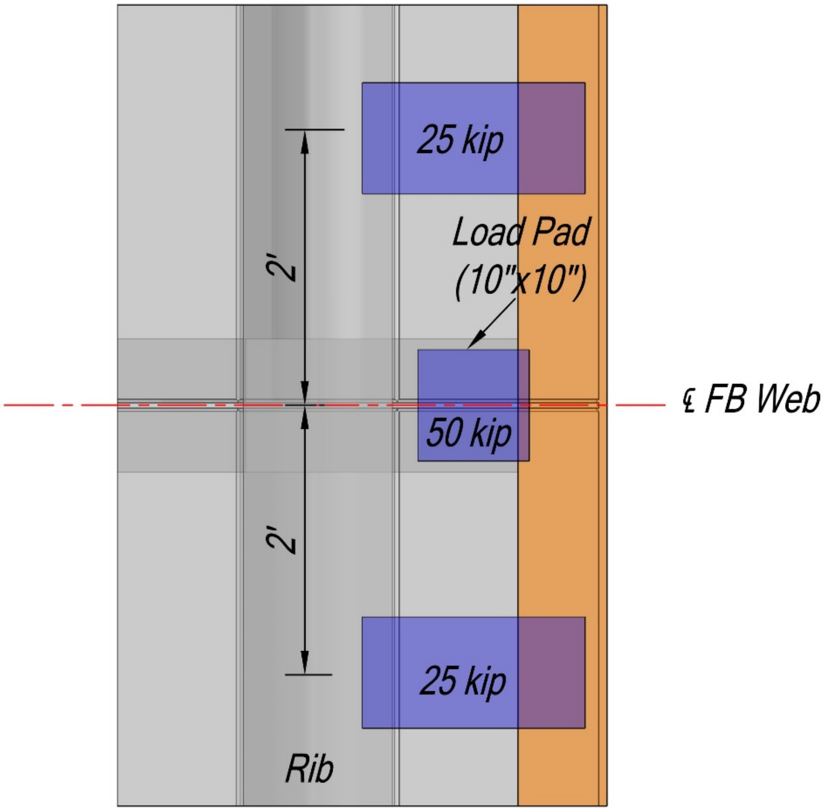

Figure 68. Plan view of the specimen showing the load positions

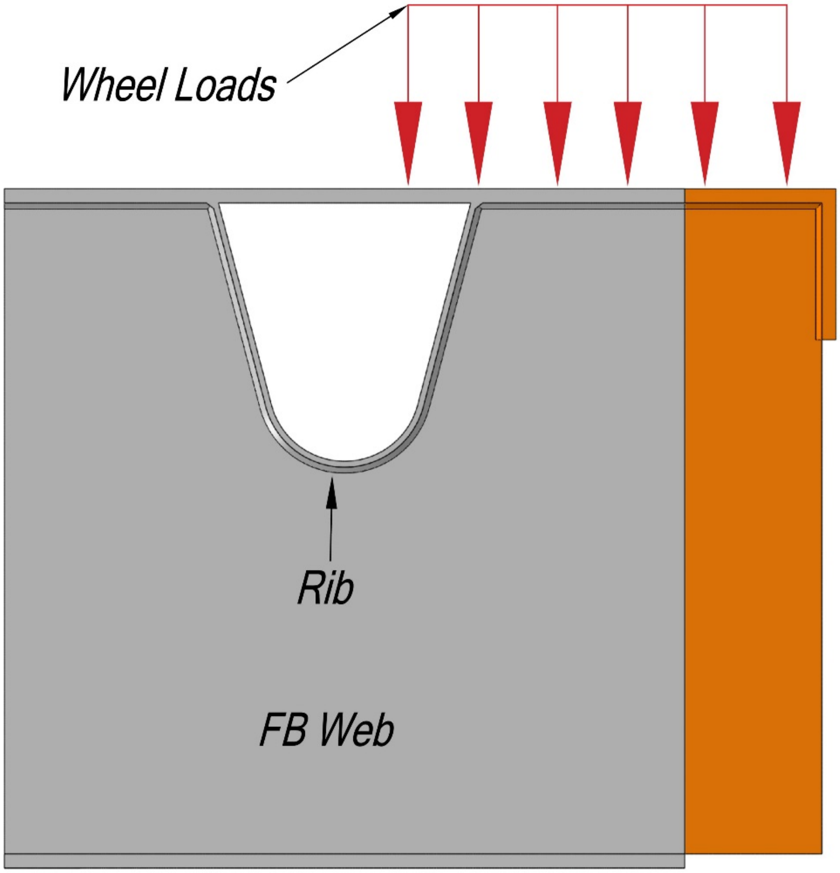

Figure 69. Cross section of the specimen showing the load positions

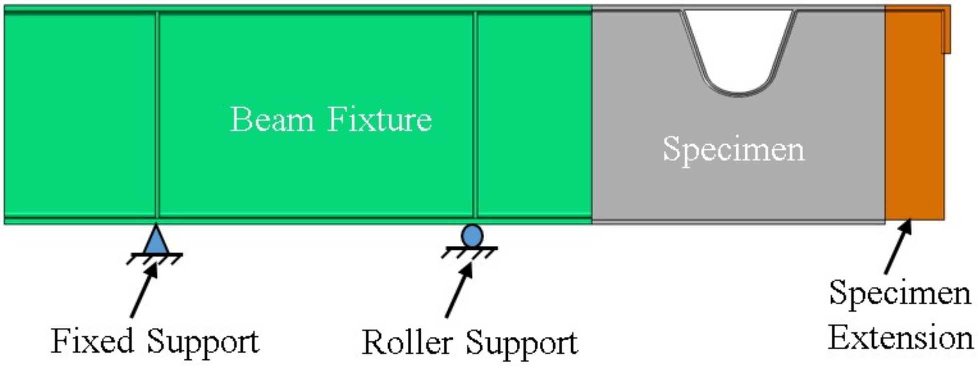

Figure 70. Boundary condition for the specimen

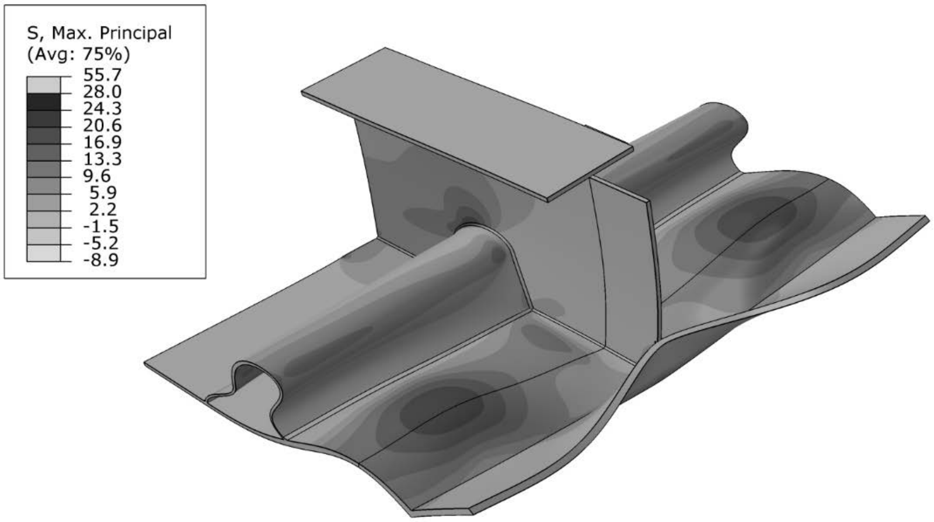

Figure 71. 3D underside view of the specimen model showing the principal stress contour

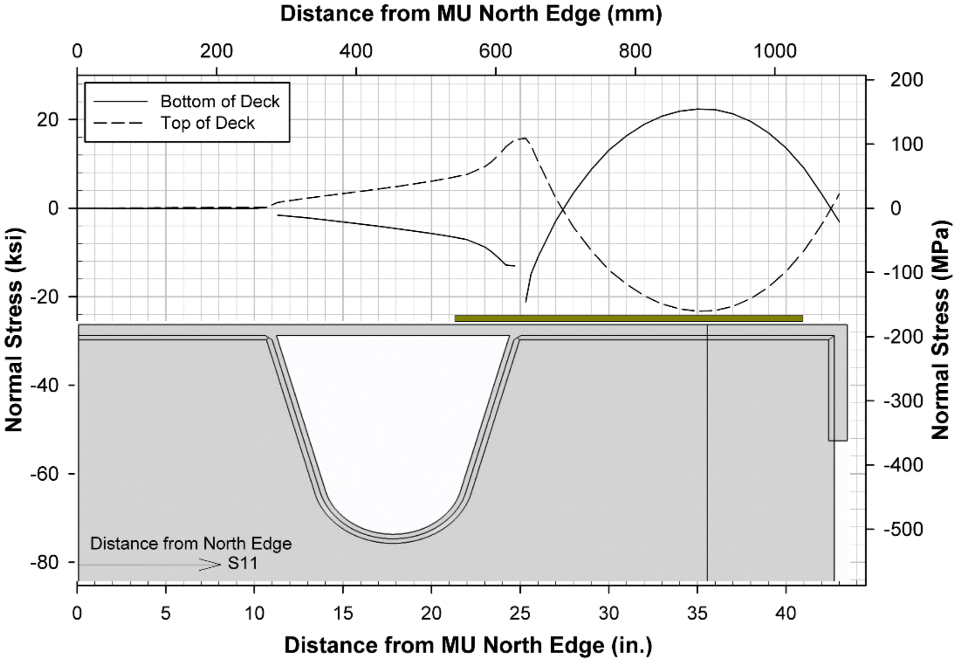

Figure 72. Normal stresses on the deck plate along a transverse section through the centerline of the east load pad

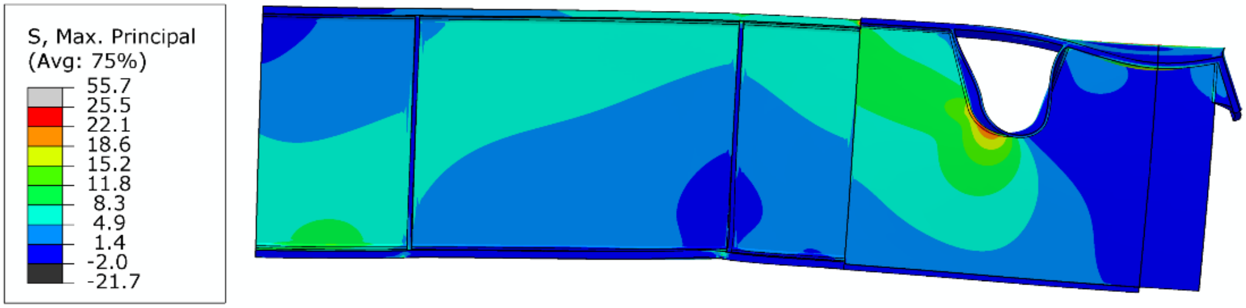

Figure 73. Principal stress contour in the specimen model

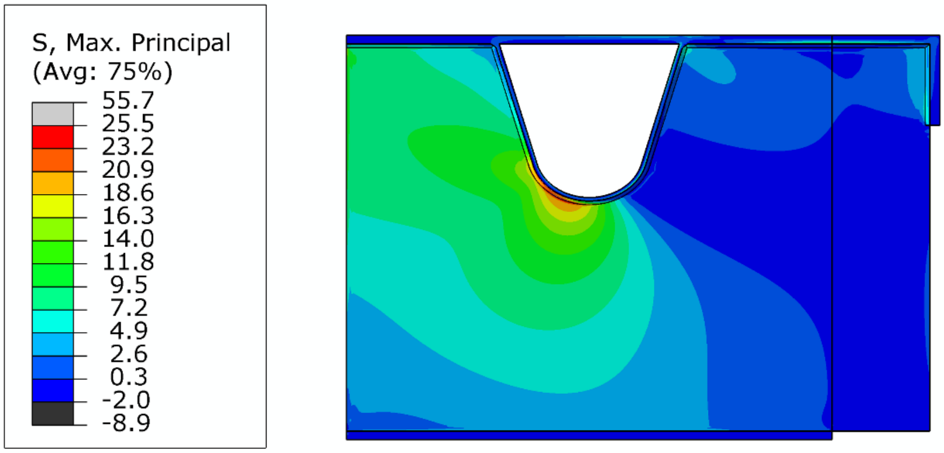

Figure 74. Principal stress contour in the floor beam web for the specimen model

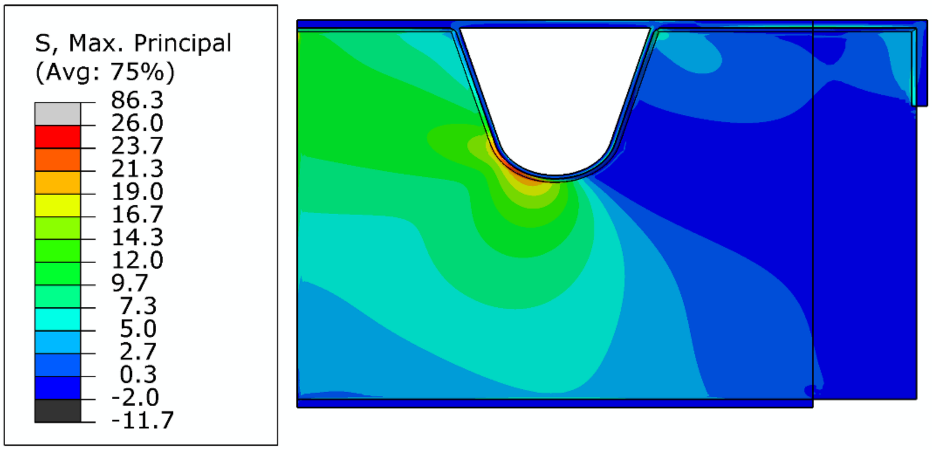

Figure 75. Principal stress contour in the floor beam web for the specimen model for MU1

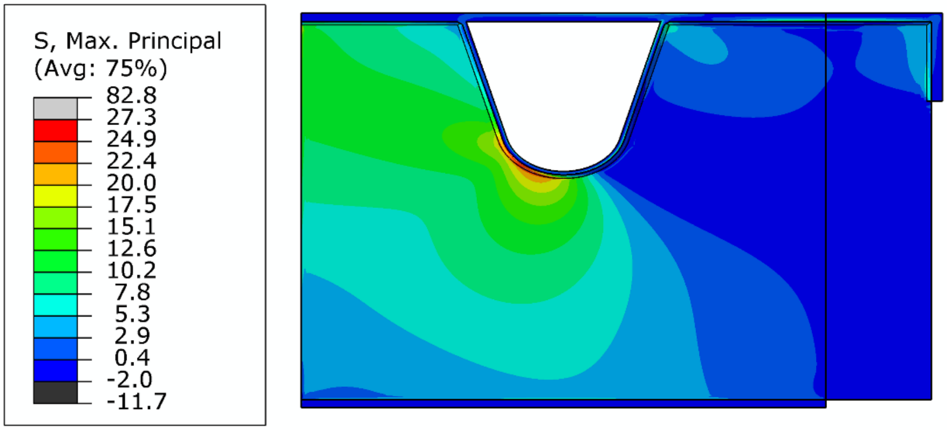

Figure 76. Principal stress contour in the floor beam web for the specimen model for MU2

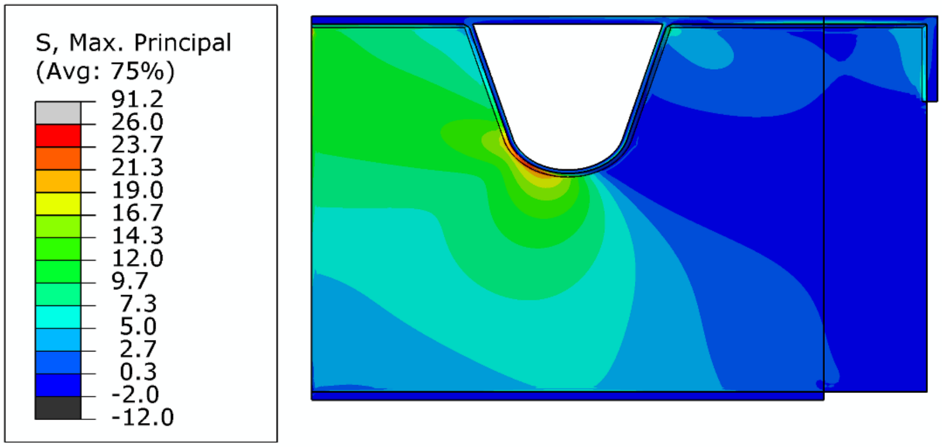

Figure 77. Principal stress contour in the floor beam web for the specimen model for MU3

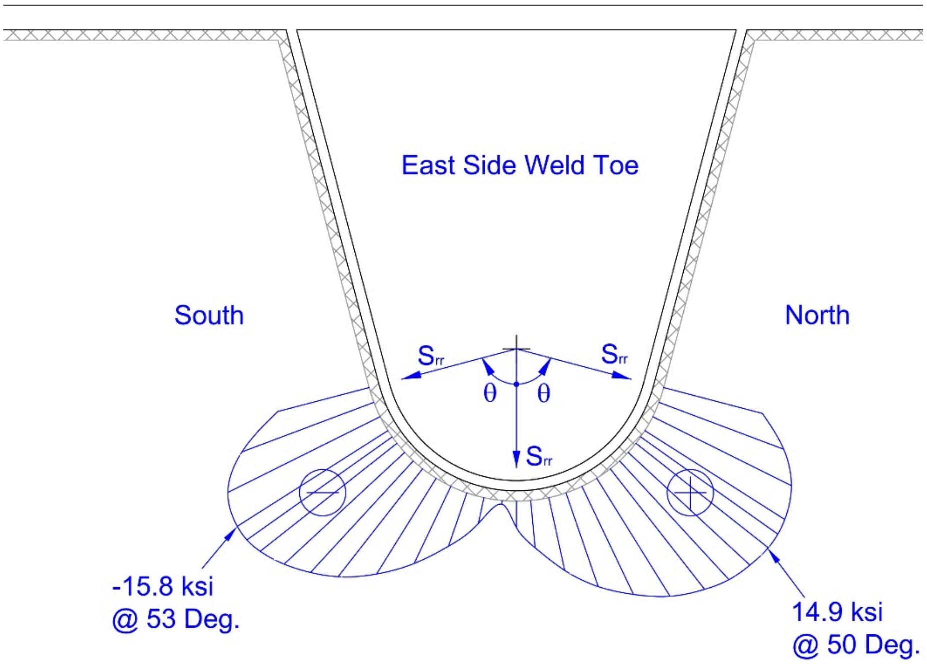

Figure 78. Variation of normal stress on floor beam surface normal to rib-to-floor beam weld toe around the rib bottom for MU1

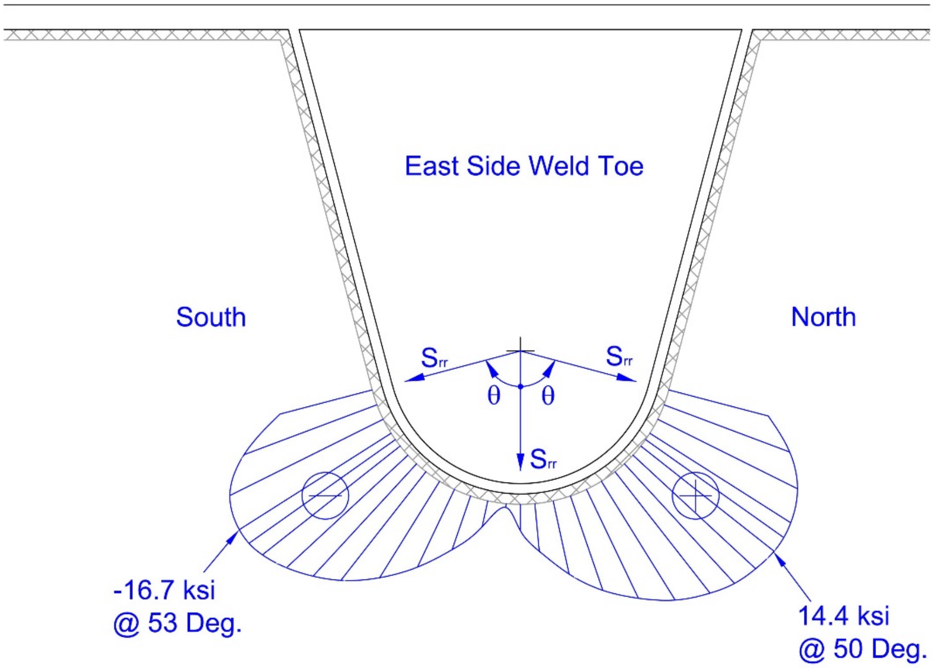

Figure 79. Variation of normal stress on floor beam surface normal to rib-to-floor beam weld toe around the rib bottom for MU2

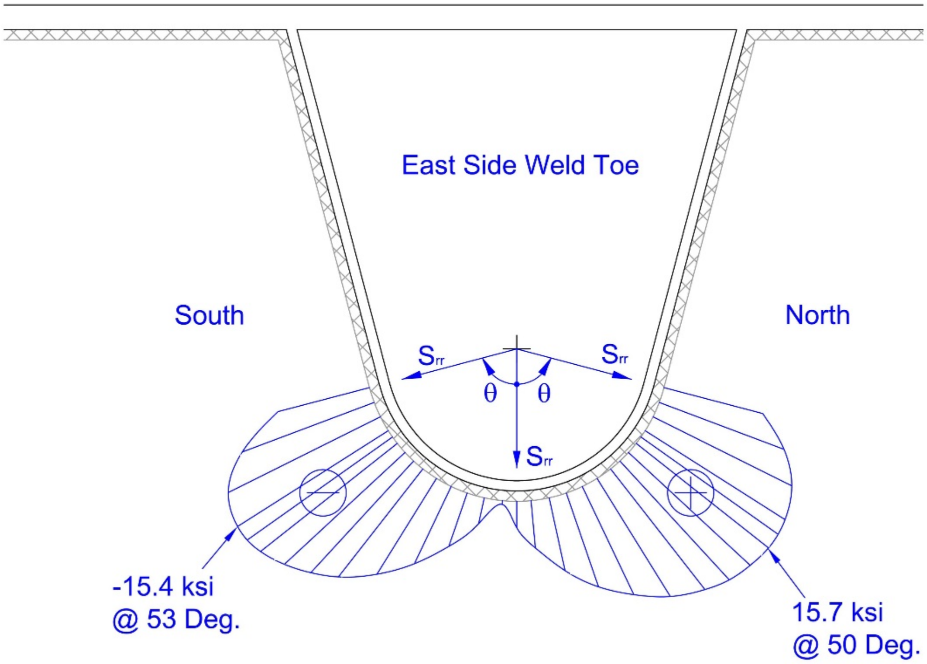

Figure 80. Variation of normal stress on floor beam surface normal to rib-to-floor beam weld toe around the rib bottom for MU2

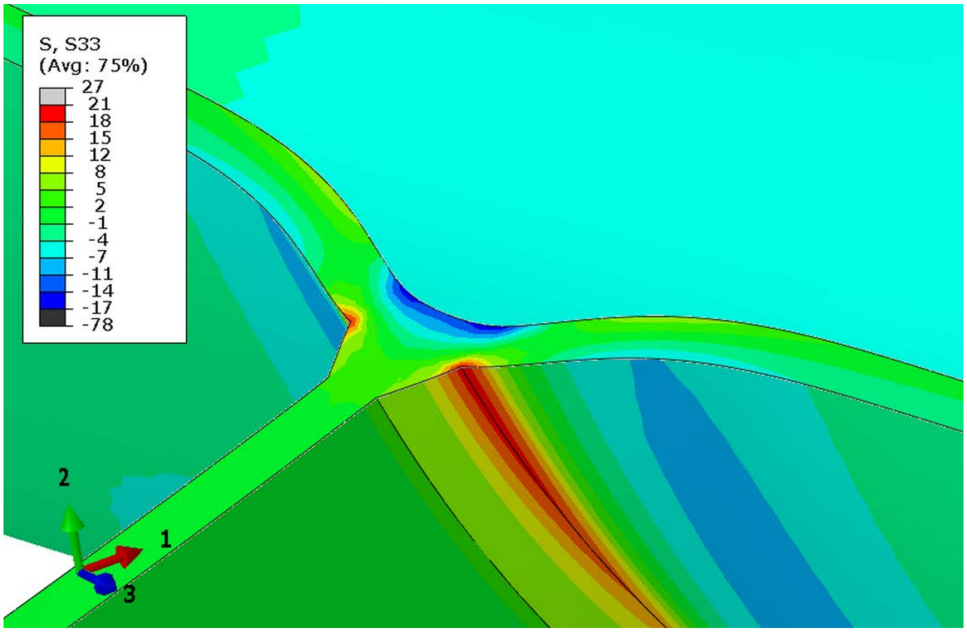

Figure 81. Radial section through the floor beam and rib of the specimen model, at about 60° from the center line of the rib in the clockwise direction, showing the contour of stresses in the rib direction

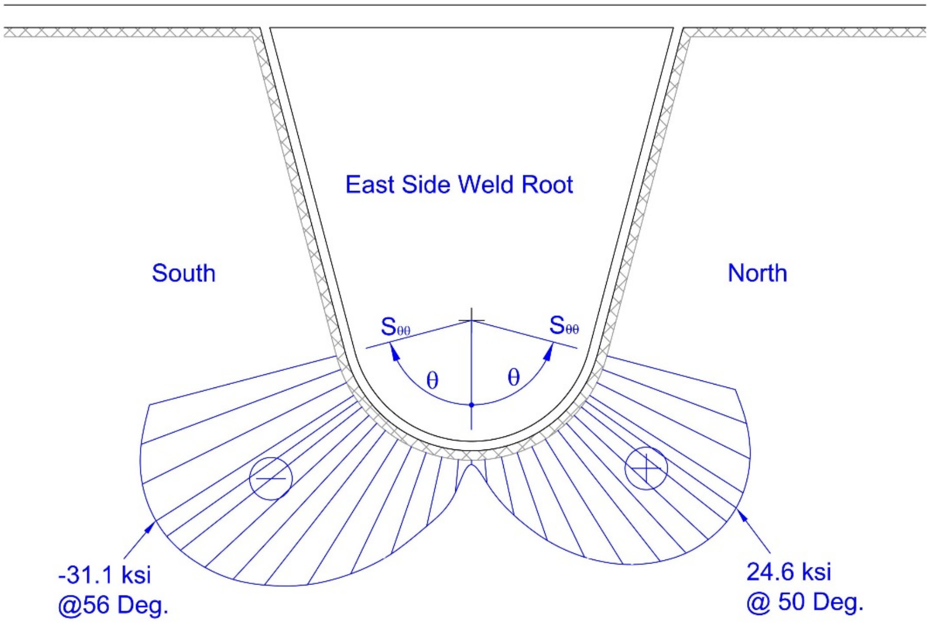

Figure 82. Variation of circumferential stress at the weld root of the rib-to-floor beam weld around the rib bottom for MU1

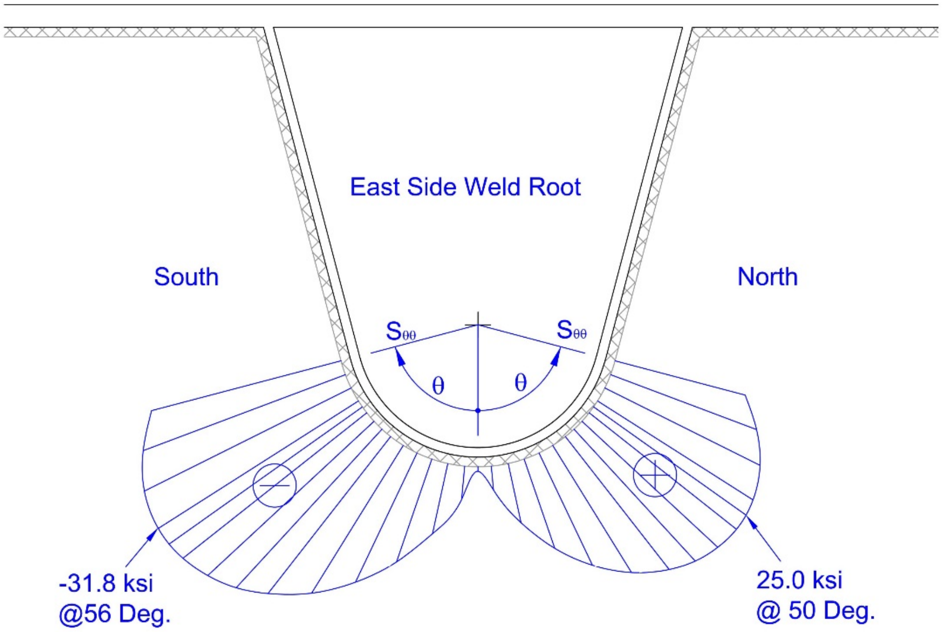

Figure 83. Variation of circumferential stress at the weld root of the rib-to-floor beam weld around the rib bottom for MU2

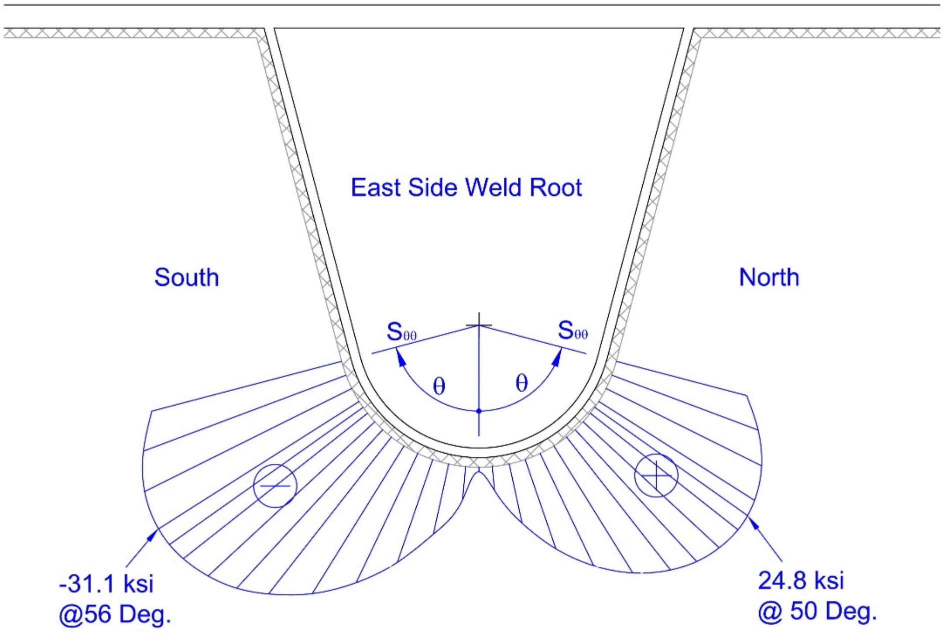

Figure 84. Variation of circumferential stress at the weld root of the rib-to-floor beam weld around the rib bottom for MU3

Figure 85. Modification of mockup specimen by addition of angle

Figure 86. Modification of mockup specimen by splicing plate to floor beam

Figure 87. Automatic welding of rib-to-deck plate connection

Figure 88. Grinding of floor beam to match with rib-profile

Figure 89. Extensive efforts for rib-to-floor beam fit-up

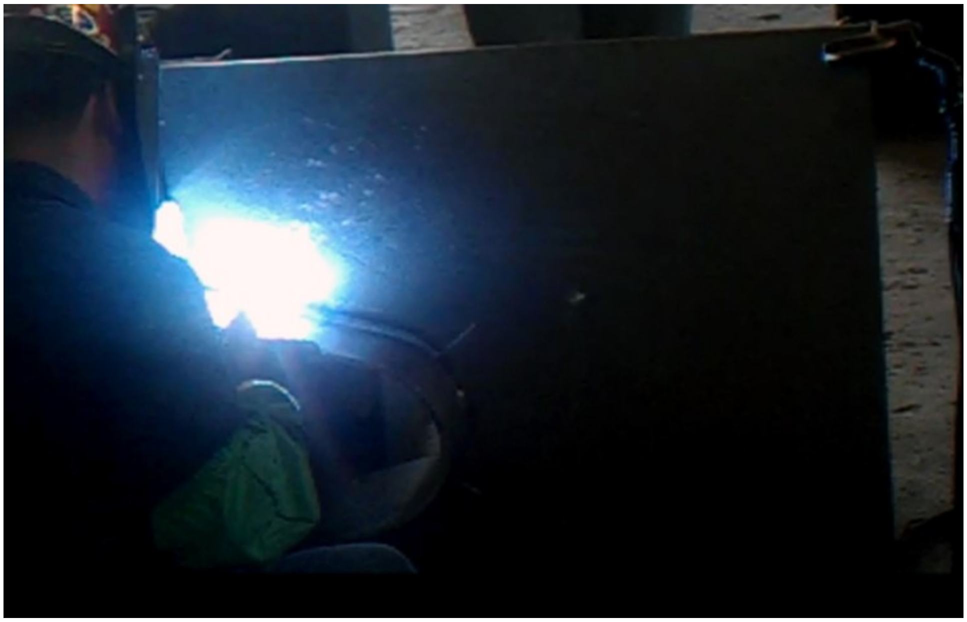

Figure 90. Manual welding of rib-to-floor beam connection

Figure 91. PAUT of the mockup specimen using GE Phasor XS; also seen are the discreet sections where the test data were recorded

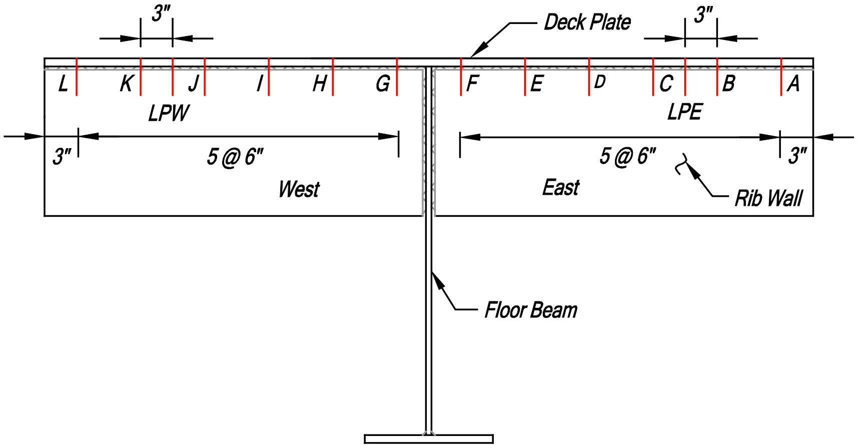

Figure 92. South side elevation showing the section locations

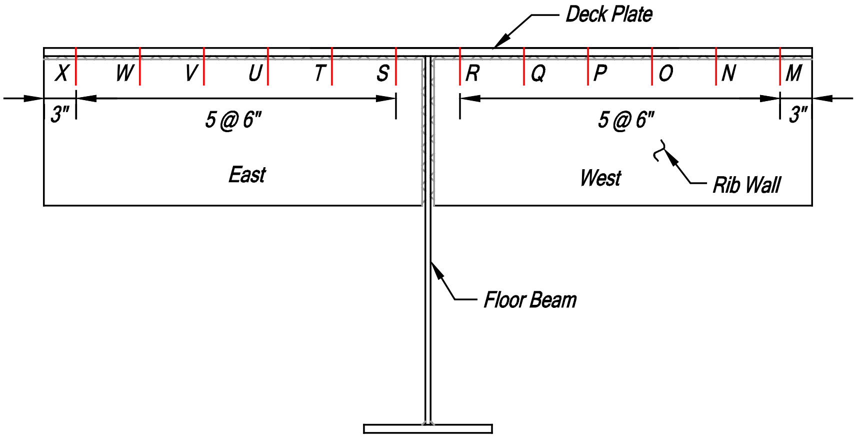

Figure 93. North side elevation showing the section locations

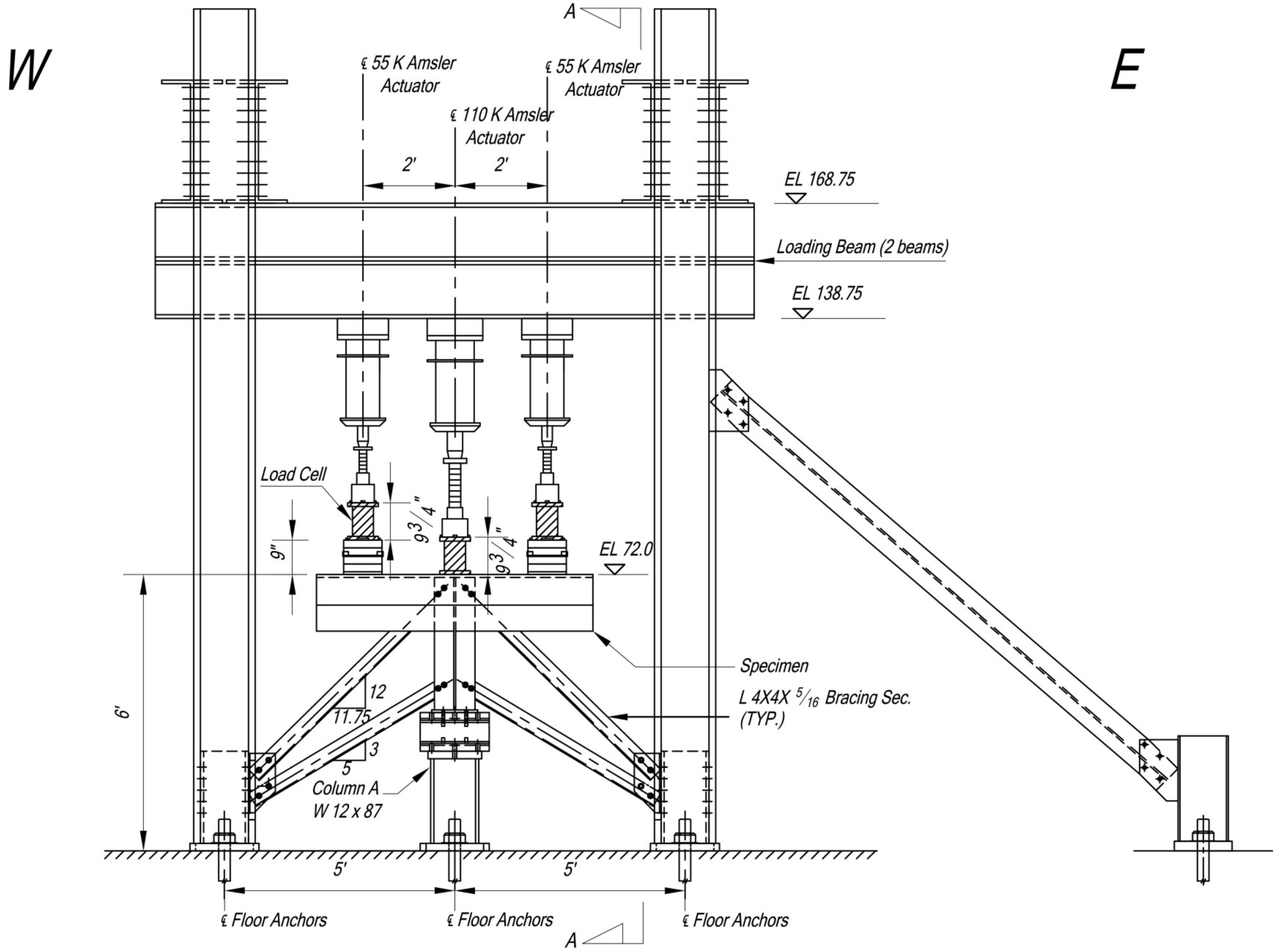

Figure 94. North elevation of the test setup for mockups

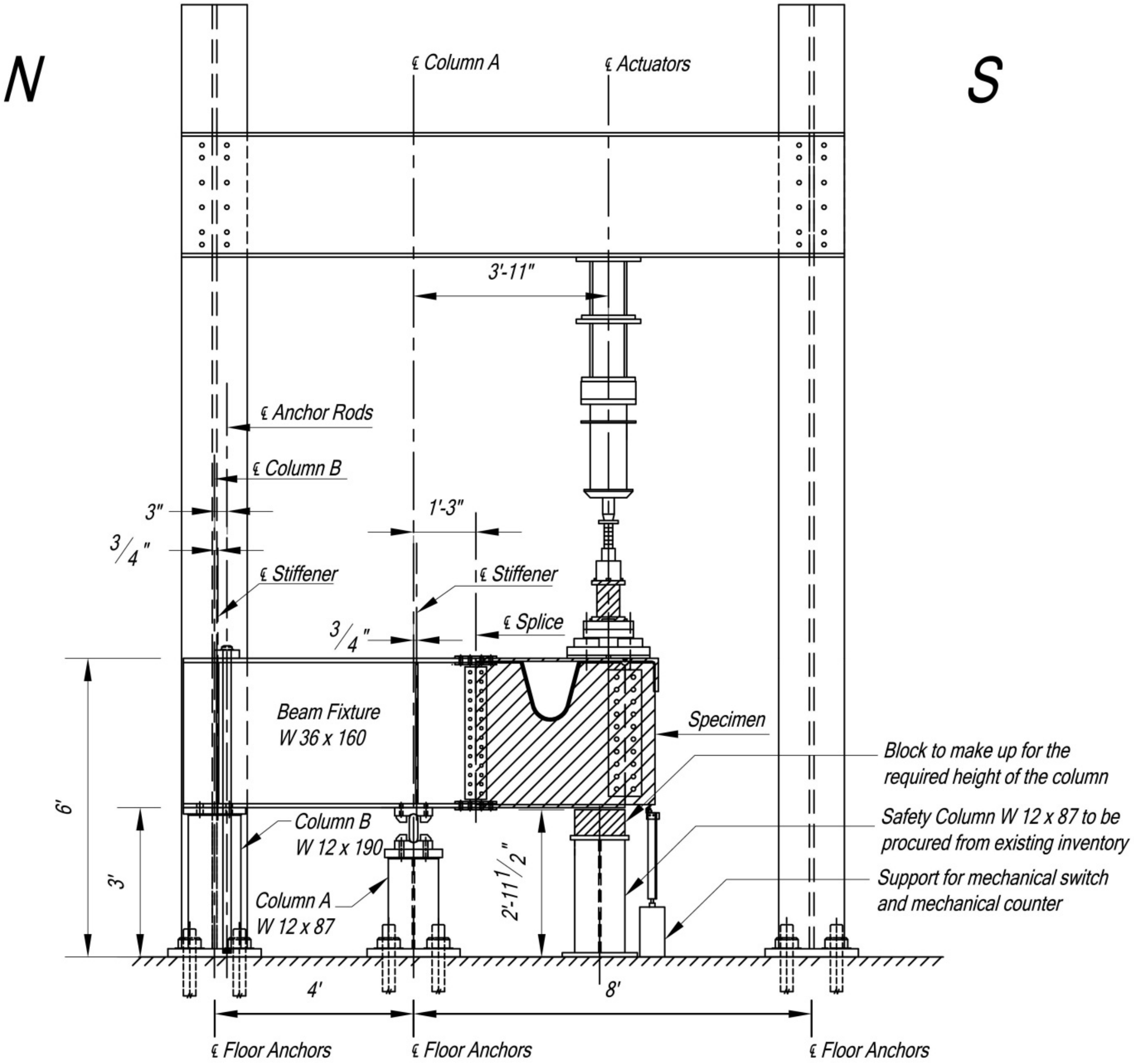

Figure 95. Side view (section A-A) of the test setup (looking from west)

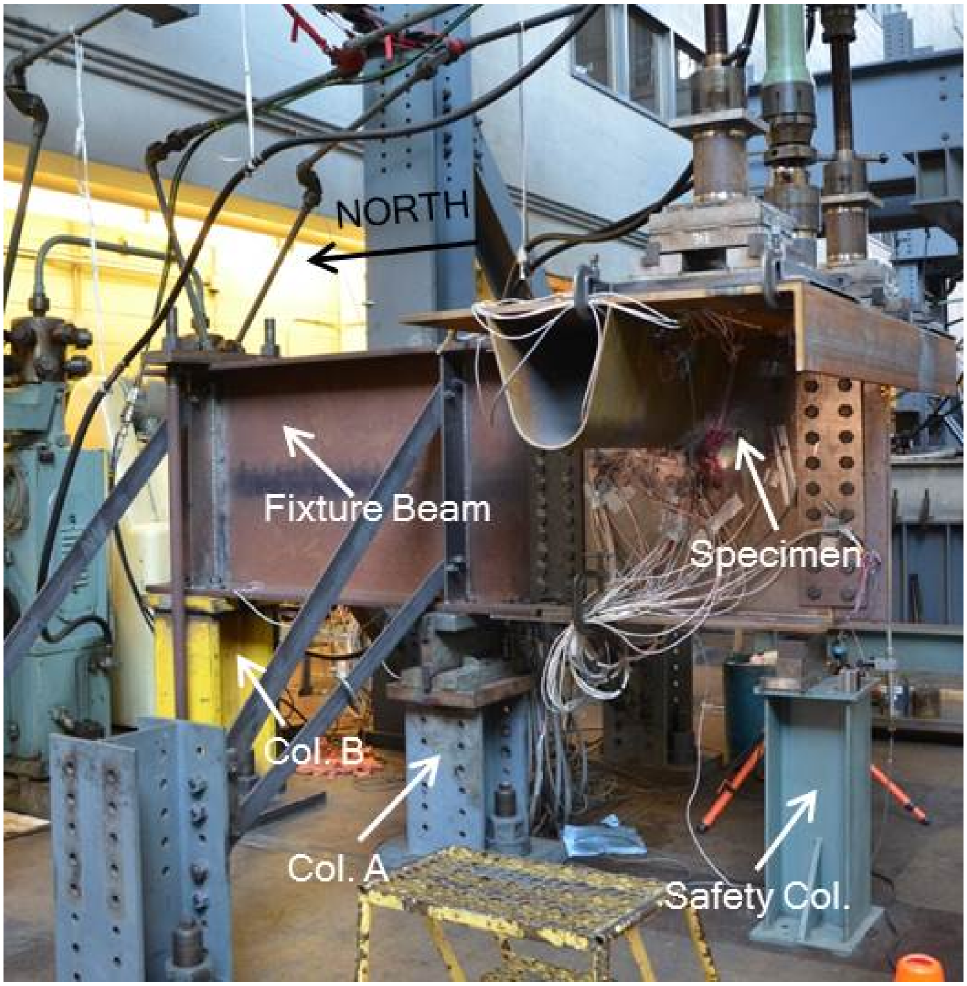

Figure 96. Test set up at Fritz Engineering Laboratory

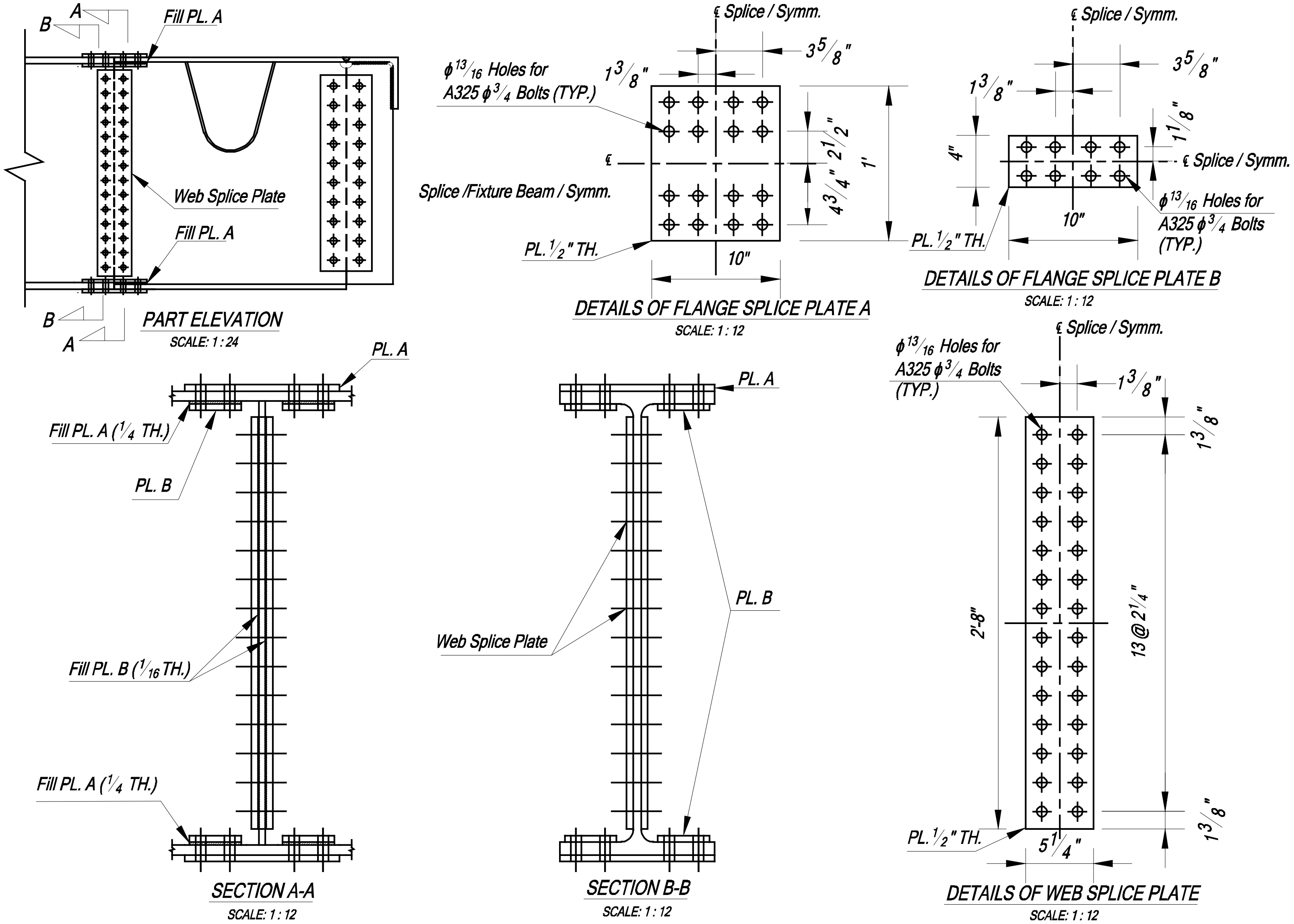

Figure 97. Details of Splice connection between beam fixture and the specimens

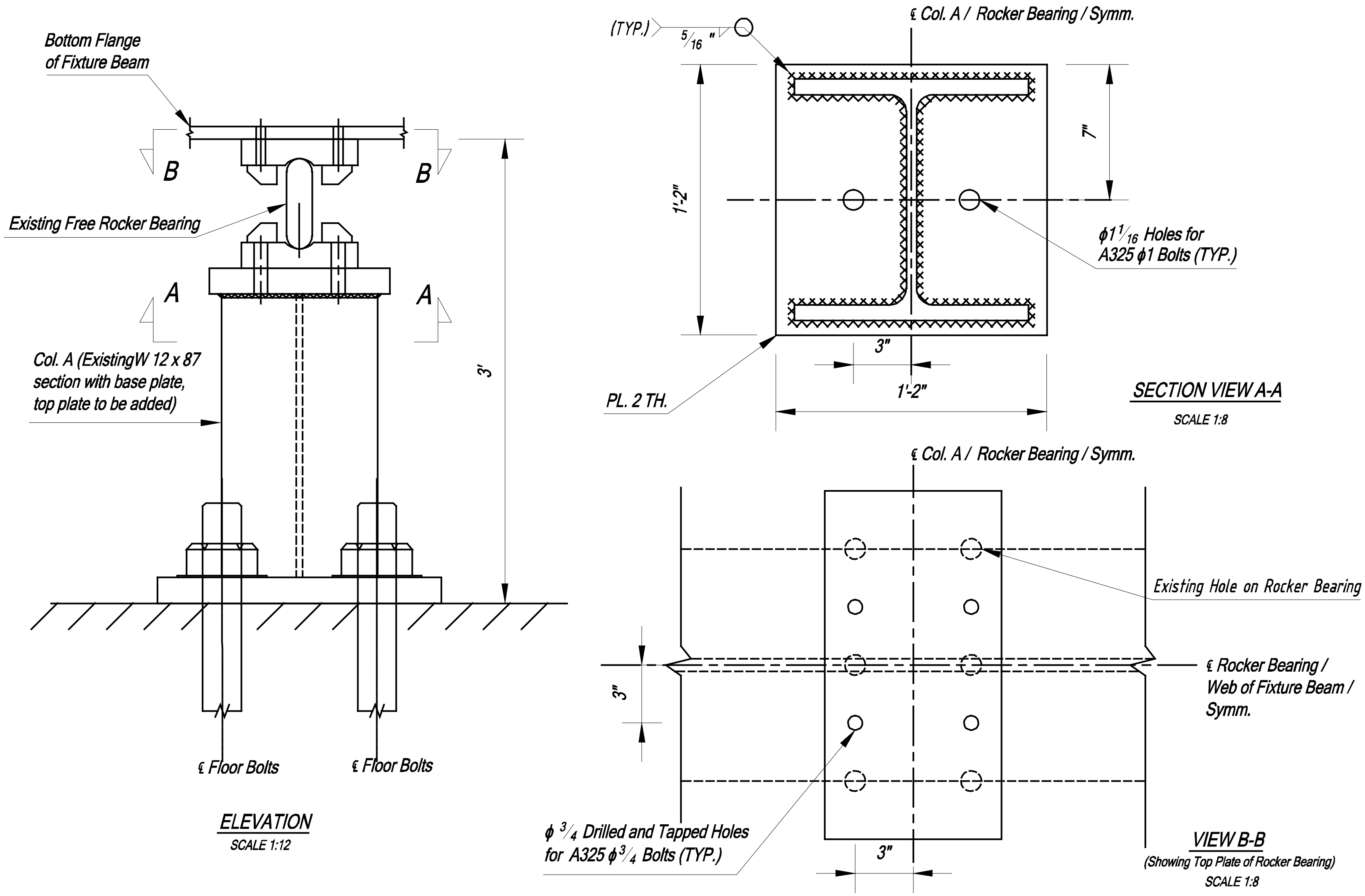

Figure 98. Connection detail of beam fixture to Column A

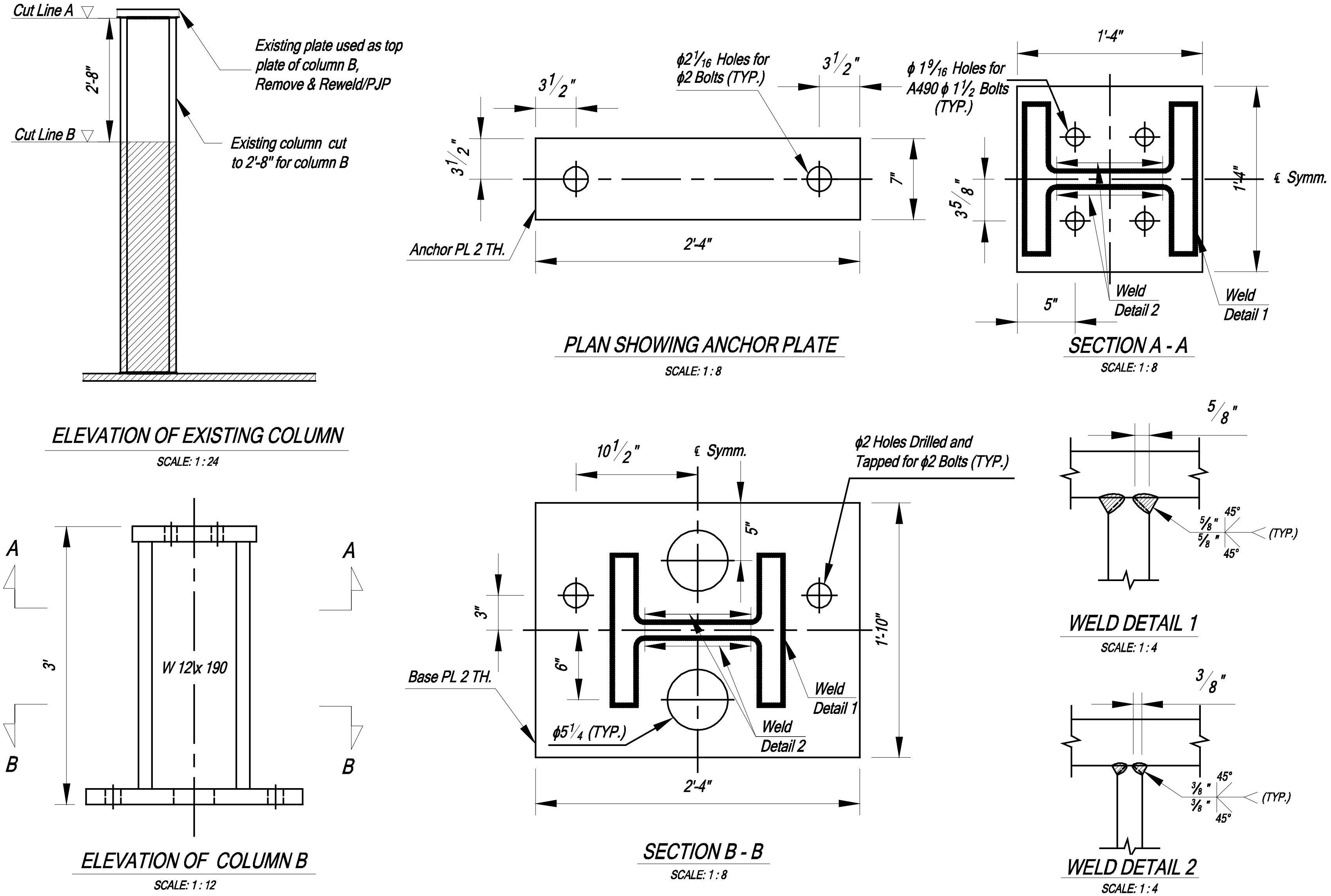

Figure 99. Connection detail of beam fixture to Column B

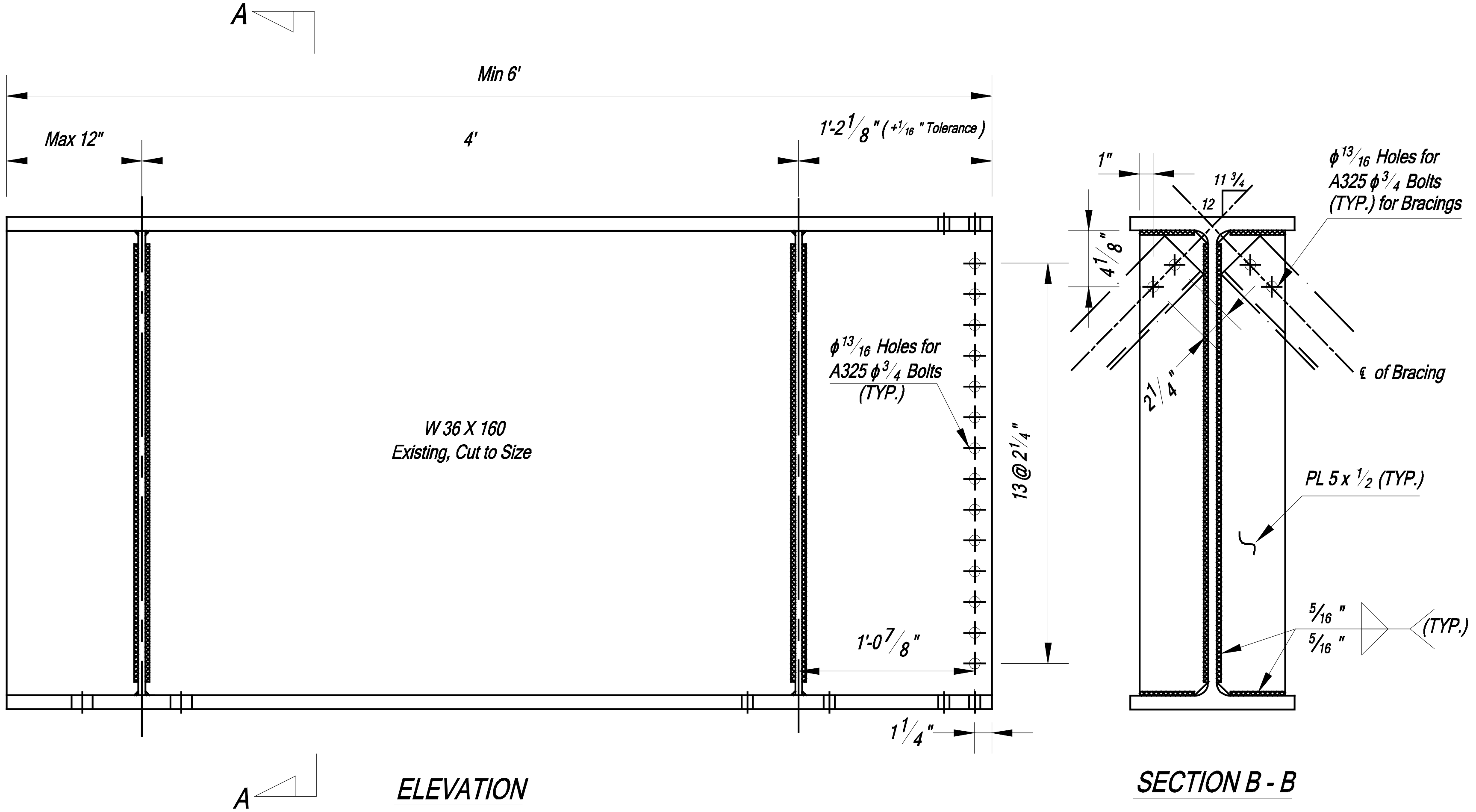

Figure 100. Detail of stiffener plates

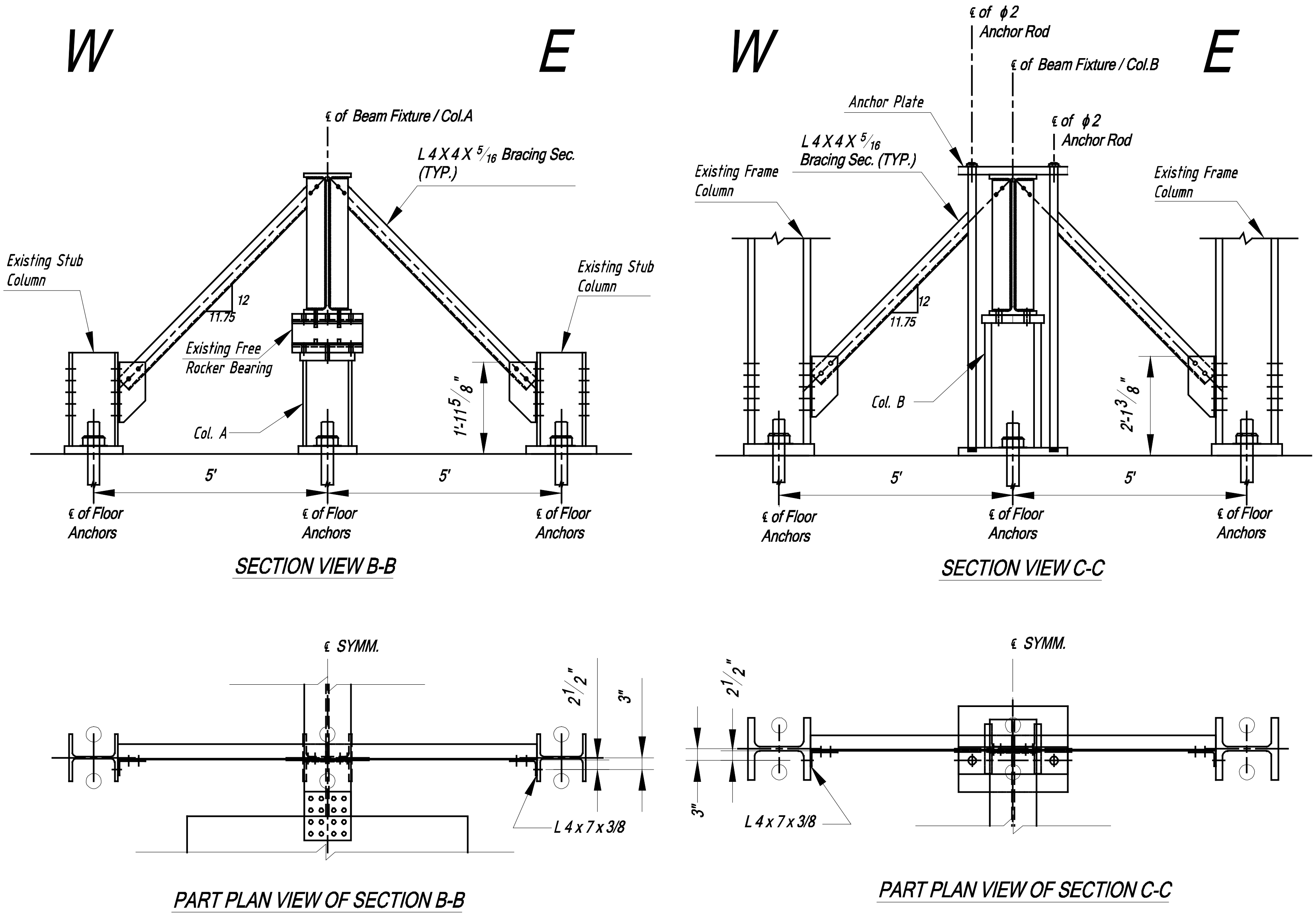

Figure 101. Detail of vertical bracing

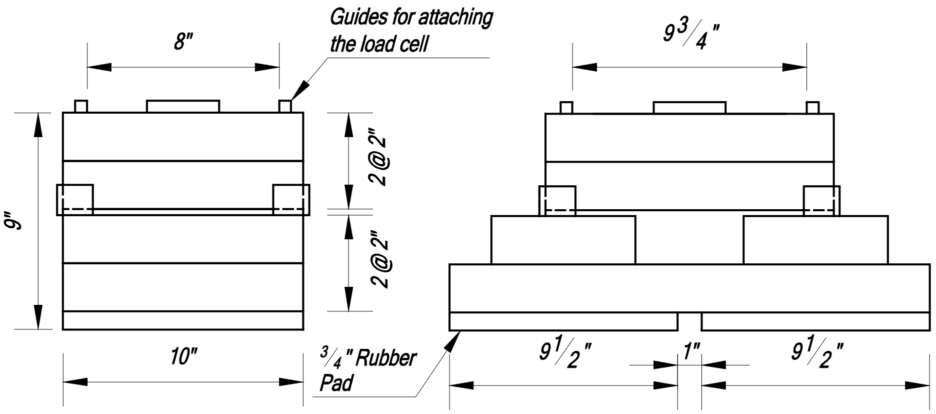

Figure 102. Details of loading block

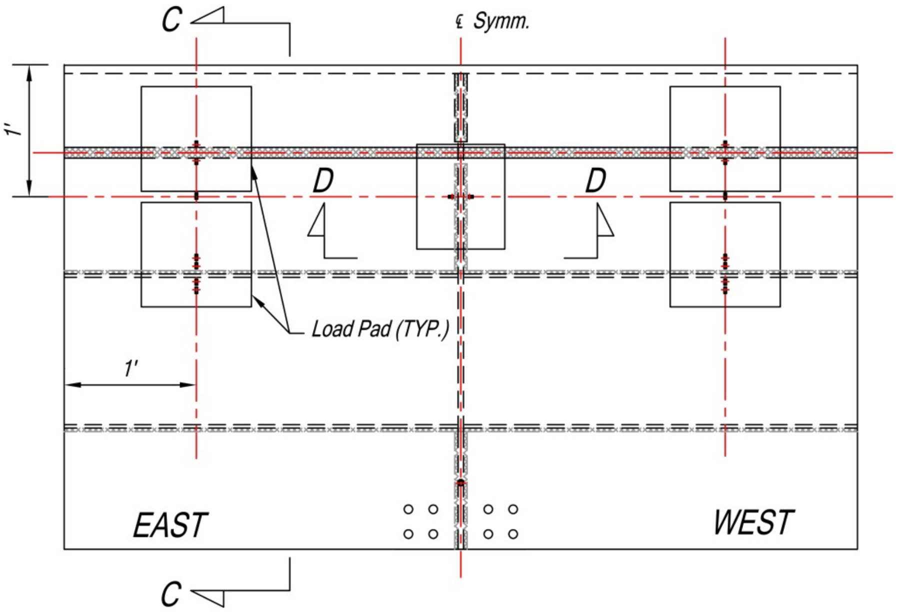

Figure 103. Instrumentation on deck plate

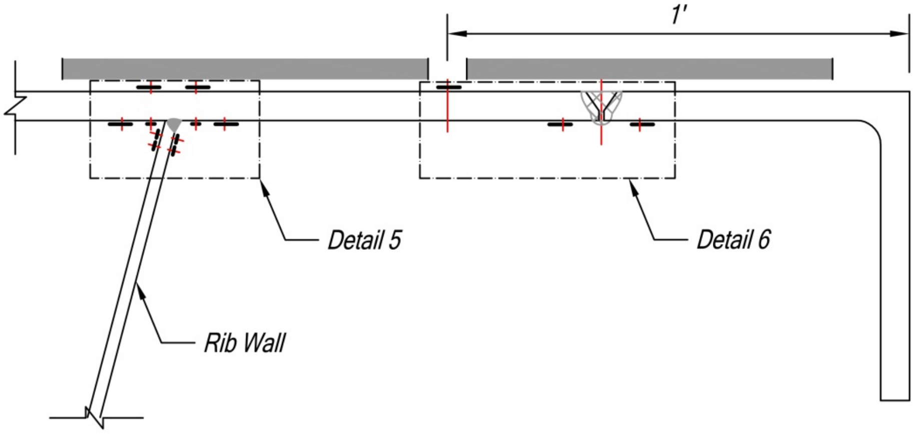

Figure 104. Part section C-C (refer Figure 103)

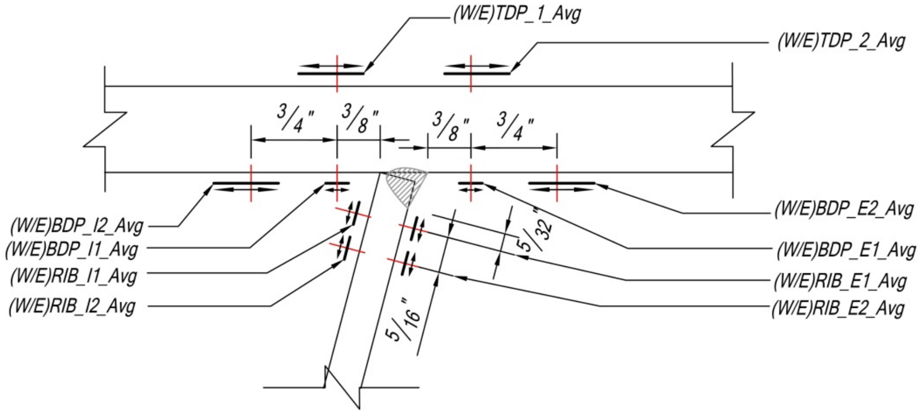

Figure 105. Detail 5 (refer Figure 104) showing gauges installed around rib-to-deck weld

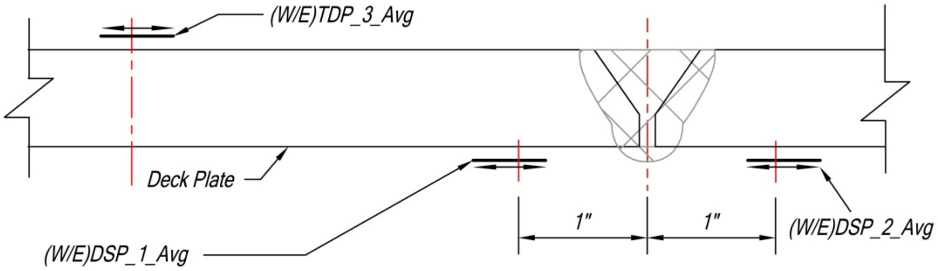

Figure 106. Detail 6 (refer Figure 104)

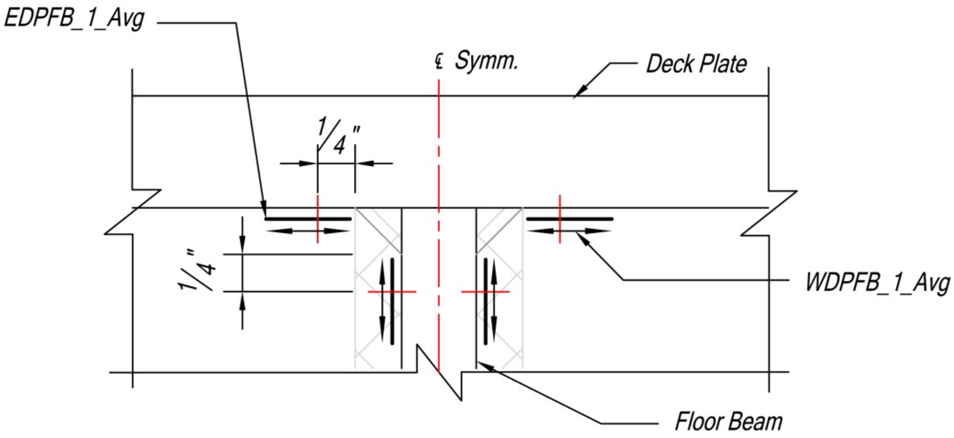

Figure 107. Part section D-D (refer Figure 103) showing gauges installed around deck-to-floor beam weld

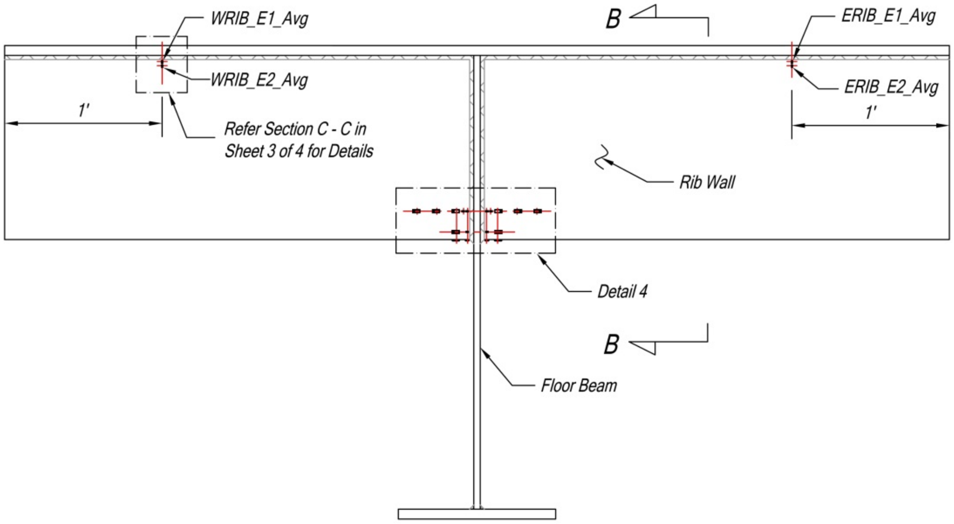

Figure 108. Side elevation of the specimen showing the gauges installed on the outer surface of the rib wall

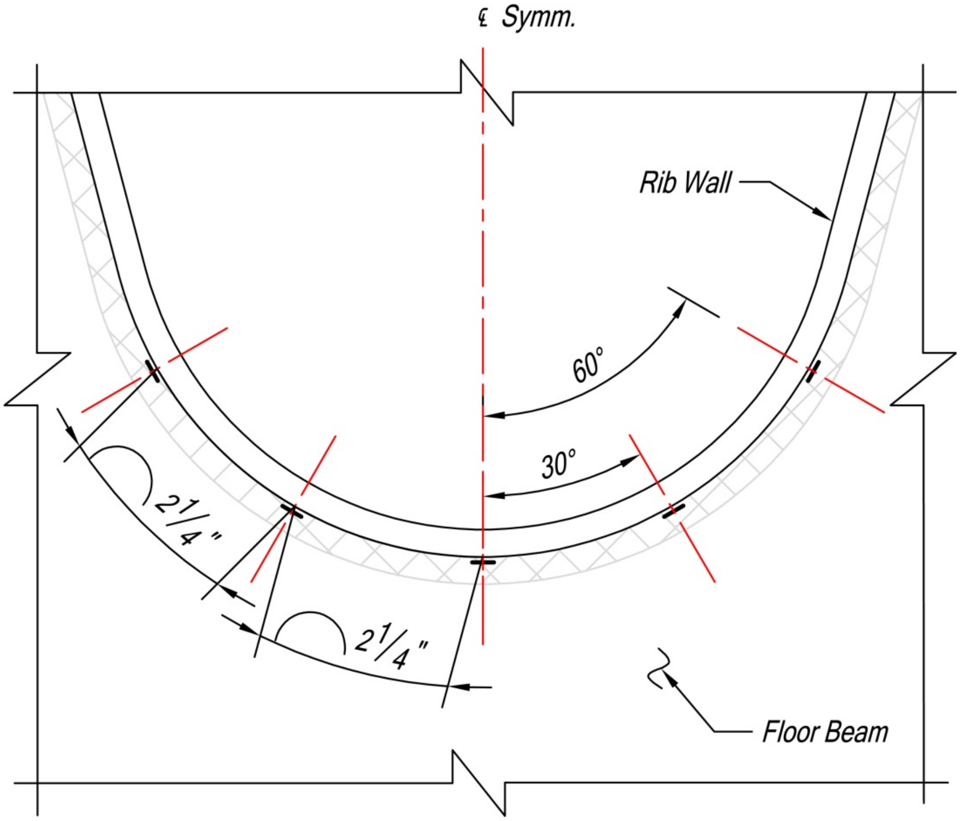

Figure 109. Section B-B (refer Figure 108)

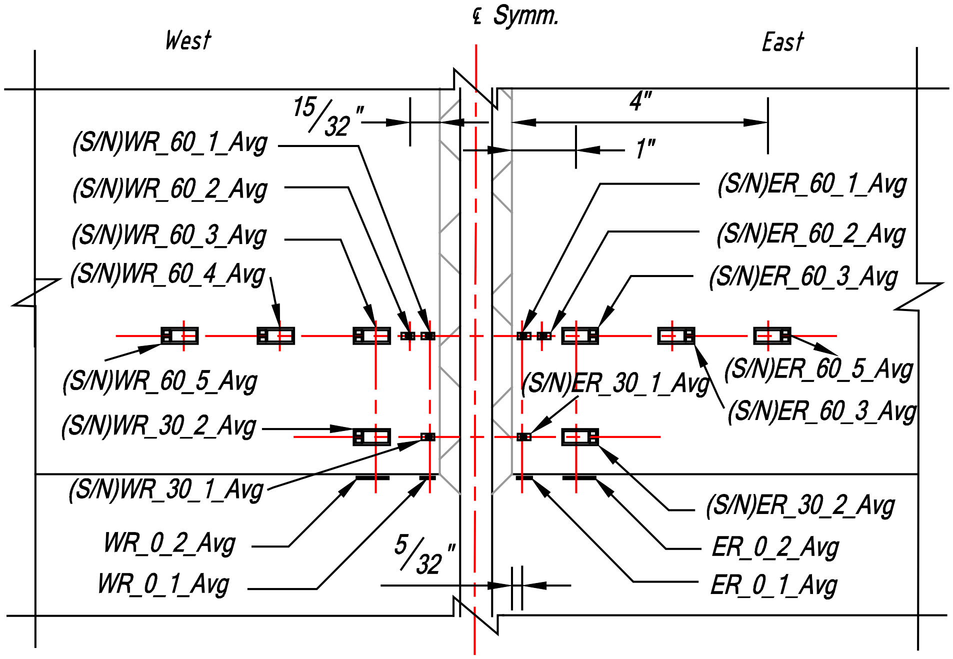

Figure 110. Detail 4 (refer Figure 108) showing the gauges installed on the rib wall at the rib-to-floor beam weld

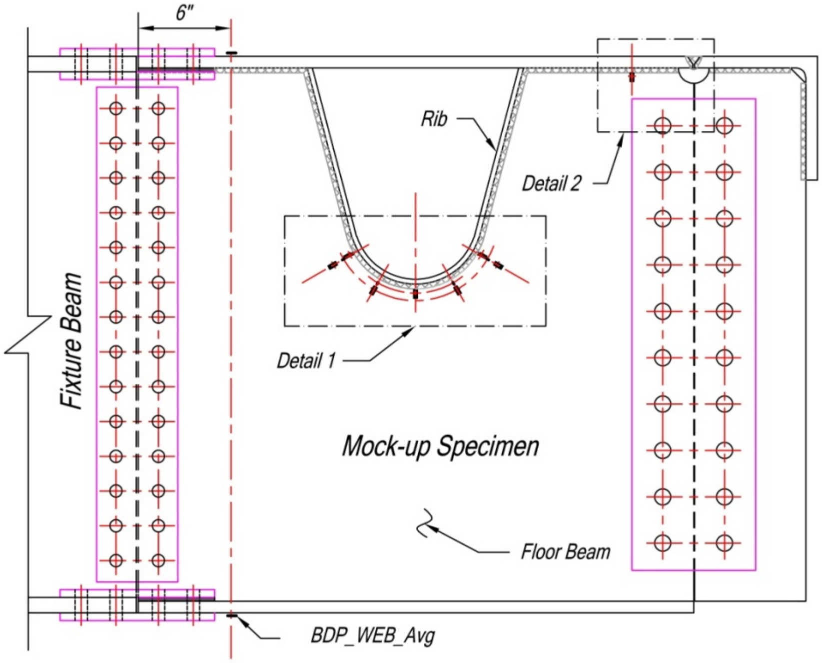

Figure 111. West elevation of the specimen showing the gauges installed on the floor beam

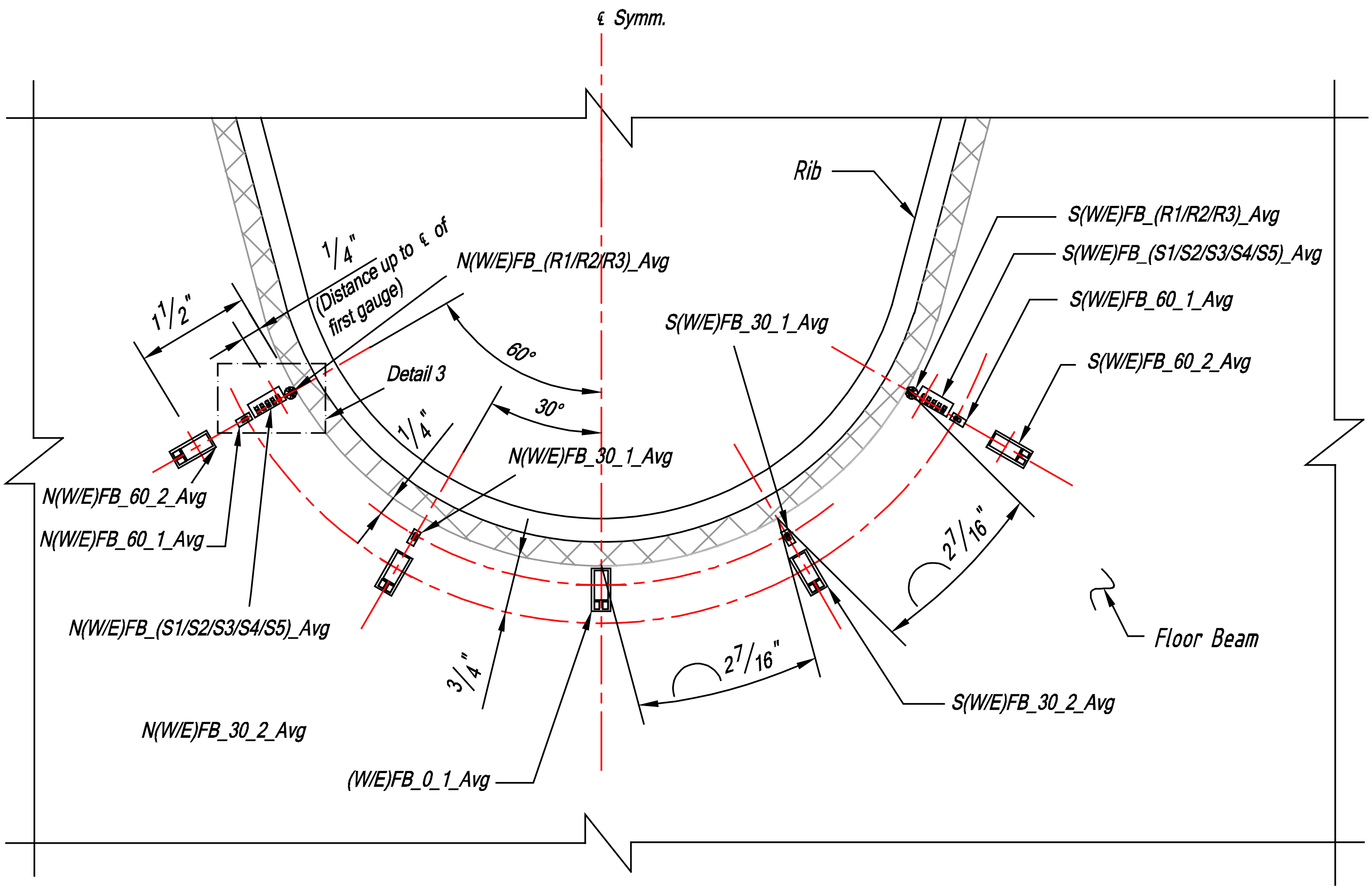

Figure 112. Detail 1 (refer Figure 111) showing the gauges installed on the floor beam at the rib-to-floor beam weld

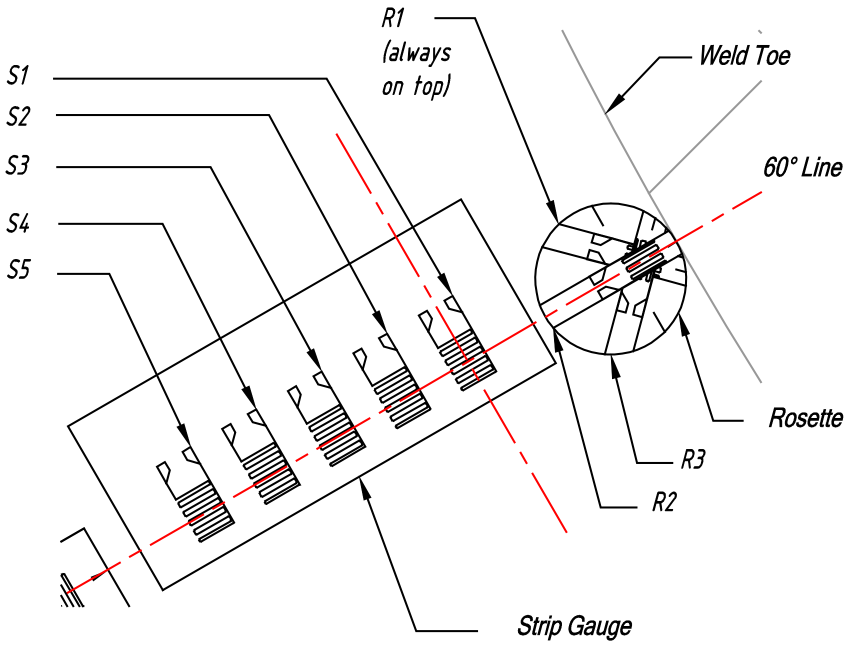

Figure 113. Detail 3 (refer Figure 112) showing the numbering of the rosette and the strain gauge

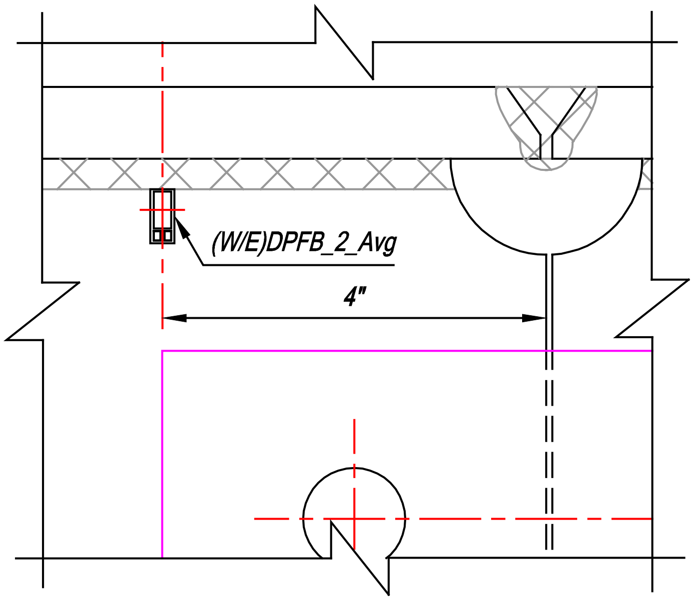

Figure 114. Detail 2 (refer Figure 111) showing the gauges installed on the floor beam at the deck-to-floor beam weld

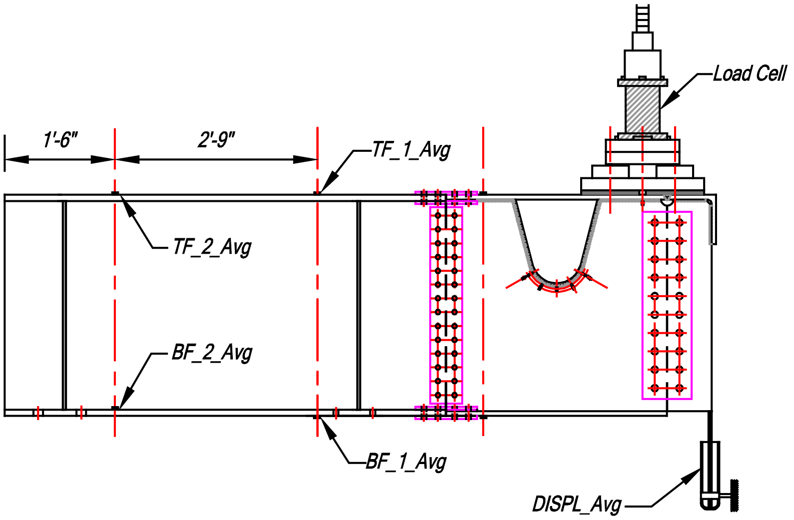

Figure 115. Elevation of the specimen with beam fixture showing the load cells, LVDT and the gauges installed on the beam fixture